NORTHWESTERN UNIVERSITY

Probing Excited State Dynamics in Metalloporphyrins and Hemoproteins with X-Ray Transient Absorption Spectroscopy

A DISSERTATION

SUBMITTED TO THE GRADUATE SCHOOL IN PARTIAL FULFILLMENT OF THE REQUIREMENTS

for the degree

DOCTOR OF PHILOSOPHY

Field of Chemistry

By

Megan Lynn Shelby

EVANSTON, ILLINOIS

December 2016

Abstract

Probing Excited State Dynamics in Metalloporphyrins and Hemoproteins with X-Ray Transient Absorption Spectroscopy

Megan Lynn Shelby

Metalloporphyrins fulfill incredibly diverse chemical roles in biology and photocatalysis, where they act as photosensitizers, redox sites, substrate binding sites, and facilitators of long range electron transfer. Metalloporphyrin chemistry is uniquely tuneable through conformation and functionalization of the porphyrin ring, choice of metal, and interaction with the environment as these impact the interaction between ligand orbitals and metal d orbitals. Many biological or photocatalytic processes in these systems can be optically triggered. To understand how excited state chemistry can be controlled, either by the rational design of photocatalysts or by metalloproteins to regulate their function, it is key to ask how porphyrin structure and electronic structure evolve during these dynamic processes. X-ray Transient Absorption (XTA) spectroscopy is a pump-probe technique that utilizes the metal site electronic structure and local coordination geometry sensitivity of core-level X-ray absorption to follow excited state dynamics.

This work uses XTA to investigate the excited state dynamics of three metalloporphyrin systems: Nickel tetramesitylporphyrin (NiTMP), Carbmonoxymyoglobin (MbCO), and Zinc porphyrins, including zinc-protoporphyrin IX (ZnPPIX) substituted hemoproteins Cytochrome C

and Myoglobin. NiTMP and MbCO are both open shell metalloporphyrins where excited states rapidly relax through vacant d-orbitals. Our ultrafast XTA studies are among those shaping a new field using the ultrafast pulses of X-ray Free Electron Lasers (XFELs) to perform X-ray spectroscopy, in this case to measure sub-ps dynamics in these systems. In both cases, changes in the porphyrin structure occur in response to the excited state rearrangement of d electrons within a picosecond. In the case of NiTMP, an intermediate species not resolved by other ultrafast techniques was observed. ZnPPIX is a closed shell metalloporphyrin, and thus has very long lived porphyrin-centered excited states that are Jahn Teller unstable. Here we use this instability as a probe of the degree of porphyrin interaction with the protein in which it is bound.

_____

Professors Lin X. Chen and Brian M. Hoffman

Research Advisors

Acknowledgements

First and foremost I would like to acknowledge my advisors Lin Chen and Brian Hoffman, who have been incredibly supportive not only of my research, but of my growth as a scientist and as a person. Their wealth of expertise is an inspiration to me and without it I would never be where I am today. Lin has always been both a very supportive and remarkably engaging, tenacious advisor, admirable qualities in both a boss and a person. She is understanding and incredibly caring, but still able to provide that much needed push to expand one's thinking. Brian has been an indispensable resource and can be counted on to provide the big picture where it is lacking. Thank you both for your guidance, patience, encouragement, and support.

I would also like to thank the other members of my committee: Professors Emily Weiss, Amy Rosenzweig, and Tom Meade (the chair of my Qualifying Examination committee). Their guidance and constructive criticism has been a boon to my graduate career. Thank you for challenging me to think critically about my research and my scientific goals, and for being a voice of reason. I always felt my committee was on my side, and for that I am eternally grateful

I have been fortunate enough to find myself surrounded with an amazing cohort of colleagues and friends during my time at Northwestern. I would particularly like to thank Michael Mara, who is largely responsible for anything that I may now know about X-rays. From my very first year, Mike has been incredibly generous with his time, his knowledge, and his superhuman tireless effort. Although he graduated nearly three years ago now, he is still the unique person who will sit down and really hash out a problem that is not his own. I be forever grateful that he was my mentor. Kristopher Haldrup was also instrumental to the success of the XFEL work presented in this thesis.

He possess a rare unassuming nature that made a technique I was very inexperienced in approachable… and we had fun doing it too! I owe him a least a few beers for this.

I have spent enough time late at night on the beamline with these and other members of the Chen Group X-ray team that it would be impossible to imagine my graduate career without them. The things one finds hilarious at 3 am on four hours of sleep are ephemeral, but the friendships are real. Dugan Hayes and Ryan Hadt, thanks for the midnight trike rides, the coffee cup concerts, the chuckles, and the excellent science. Although I think you have some offset, try to put down Peter's papers once in a while because *that's weird.*

Thanks also the rest of the Chen and Hoffman groups; folks who especially contributed to this work include Kelly Fransted, Matthew Kelley, Taylor Page, Andrew Stickrath, Dolev Rimmerman, and Jiyun Hong. Nicholas Jackson *especially* did a lot of hard thinking on my behalf, thanks for learning group theory for me, Nick. Sam Brown-Xu, Pyosong Kim, Matt Kirschner, Darren Hsu, Ethan Trana, Jon Van Der Woude, Nadia Petlakh, Bharat Reddy, and Judy Nocek: thanks for your collaboration and invaluable friendship! I have tremendous affection for Tom "Keeper of the Vibes" Fauvell and Eric "Metamorphic" Manley for allowing me to interject into an almost uncountable number of conversation about fantasy football. Go easy on the office chairs, guys.

I would be remiss if I forgot to mention the folks who spent time with me even though they didn't have to, my close friends since the very first week of doing quantum problems sets on the floor: Daniel Hannah, Amber Davis, Taylor Page, Charlie Macko, Natalie Gruenke, Nick Calta, Stephanie Zaleski, and Jason Avila, you are the human connections I will always remember Chicago for. Amanda Marciel and I have been on this strange science trip together since our

freshman year at Cal, and I only hope to one day live up to your tenacity and general butt-kick tendencies.

My family has provided an immeasurable amount of support and encouragement through this process. Sarah, you understand and you always will. I simply can't imagine having to take the weird journey of the last 30 years without you. And because I am the bunion, I know a thing or two about thriving on the rich bone marrow blood supply of *friendship.* John, you are our fearless leader full stop. I learned a lot of the courage it look to do this from you. Maura, Melissa, and Al our relationship has meant so much to me as I have been away these past years and you have supported me incredibly in your own ways. Mom, you never let me be anything less than what I could be. You just don't quit or ever give up on me, or ever let me give up on myself and I love you for it. Dad, you have been taking me to science museums since I was a tiny child and so much of the analytical way I view the world comes from you. All this probably started as an insanely well considered explanation, delivered by you in fantastic detail, of one of my middle school chemistry labs while in the car on the way to who knows where. Thank you for inspiring me and teaching me without ever pushing.

Finally, I would like to thank my fiancé Julian, who is forever reminding me that I am doing this for "our future". Soon we are driving off into the sunset, and I have to say, our future is looking pretty bright.

In fond memory of Sarah, a doer.

Table of Contents

List of Figures

List of Tables

List of Abbreviations

11-ID-D: APS XTA beamline, Sector 11, Insertion Device, station D

12-BM: APS XAS beamline, Sector 12, Bending Magnet

1-MeIm: 1-methylimidazole

APD: Avalanche Photo Diode

APS: Advanced Photon Source, 3rd generation sychrotron at Argonne National Lab

CO: Carbon Monoxide

DeoxyMb: Deoxymyoglobin

DFT: Density Functional Theory

EPR: Electron Paramagnetic Resonance

ET: Electron Transfer

EXAFS: Extended X-ray Absorption Fine Struncture

fs: Femtosecond

FT: Fourier Transform

JT: Jahn Teller

LCLS: Linac Coherent Light Source

Mb: Myoglobin

MbCO: carbmonoxymyoglobin

NiOEP: Nickel octaethylporphyrin

NiTMP: Nickel tetramesitylporphyrin

NiTPP: Nickel tetraphelylporphyrin

OPS XTA: Optical Polarization Selected X-ray Transient Absorption

ps: Picosecond

RF: Radio Frequency

SASE: Self-Amplified Spontaneous Emission

SCF: Self Consistent Field

TDDFT: Time-Dependent Density Functional Theory

XAFS: X-ray Absorption Fine Structure

XANES: X-ray Absorption Near-Edge Structure

XAS: X-ray Absorption Spectroscopy

XFEL: X-ray Free Electron Laser

XPP: X-ray Pump Probe

XTA: X-ray Transient Absorption

ZnCc: Zinc Cytochrome C

ZnMb: Zinc Myoglobin

ZnP: Zinc Porphyrin

ZnPPIX: Zinc protoporphyrin IX

ZnTPP: Zinc tetraphenylporphyrin

Chapter 1. Introduction

1.1. Metalloporphyrin chemistry depends on the complex interaction between structural and electronic factors.

Metalloporphyrins possess amazingly versatile functionality, both as cofactors in biological processes such as natural photosynthesis,[1,] physiological oxygen transport,[3] and small molecule sensing, as well as in photocatalytic processes where they act as redox centers,[4-6] and photosensitizers in molecular devices.[7] Such functional versatility is enabled by a high degree of chemical tunability afforded by the choice of metal center, the ligated macrocycle, and the sensitivity of porphyrin chemistry to the environment. Changes in macrocycle functionalization can dramatically impact the distribution of electron density through the metalloporphyrin ring as well as macrocycle conformation and rigidity, leading to varied redox and electron transfer properties as the interactions between the porphyrin and metal d-orbitals are altered. Axial ligands frequently coordinate porphyrin bound metals depending on the metal electronic structure, but ligand affinities also depend on the porphyrin structure. Metal type and ring functionalization also have important effects on optical properties and excited state relaxation dynamics by altering the energetic ordering of excited states.

This level of chemical versatility invites investigation along two lines into how porphyrin chemistry is controlled by nuclear and electronic structure: for the intentional design of photocatalytic systems or to understand how porphyrin-containing biological systems have evolved to optimize certain physiologically important chemistries.

Much of the interest in metalloporphyrins as photocatalysts comes from their strong absorption of visible light, which is due to a porphyrin-centered excitation from the π bonding orbital to the π* antibonding orbital. For metalloporphyrins with no d orbital vacancies, long lived triplet excited states are formed that can transfer electrons to other moieties. If the valance d orbitals are not filled, this excitation can relax through these vacancies, frequently triggering changes in metal oxidation state, porphyrin structure, and ligation. Open-shell porphyrins have not historically been seen as candidates for solar energy conversion due to their relatively fast excited state deactivation. However, recent studies have shown that some excited transition metal complexes can initiate photochemical processes on the picosecond or sub-picosecond timescales via singlet excited states, timescales that are competitive with vibrational relaxation and faster than intersystem-crossing to a triplet excited state.[8-14] Such short-lived excited states are less susceptible to energy dissipation processes that would reduce the potential driving force of a reaction.

While there are relatively few light-triggered reactions in biology, many biologically relevant processes in porphyrin containing proteins can be optically triggered, providing valuable insight into how the protein environment regulates these dynamic processes. Heme containing proteins in particular are a very large family of metalloproteins that fill many diverse physiological roles considering they share the same active site cofactor. These roles include electron transfer, catalytic oxidation or reduction of metabolites, neutralization of damaging reactive species, and binding diatomics such as dioxygen, carbon monoxide, and nitric oxide for transportation and sensing.[3,15-19]. This reflects the extent to which porphyrin chemistry can be tuned, even for the same metal and nominal porphyrin structure, by contacts with protein matrix.

There is a vast body of literature that uses pump-probe spectroscopic methods to characterize either metalloporphyrin excited state electronic structure or changes in the nuclear geometry, for instance through transient absorption and time resolved vibrational spectroscopy respectively. However, few methods exist that are directly sensitive to both, making it difficult to discern how electronic dynamics and structural reorganization that occur on the same timescale are interrelated. Furthermore, optical signatures of metal-centered electronic transitions for excited open shell metalloporphyrins are frequently nonexistent or obscured by the strong $\pi \rightarrow \pi^*$ absorption localized on the porphyrin, which while useful for determining porphyrin centered dynamics do not provide a full picture of the electronic evolution of the system. X-ray transient absorption spectroscopy (XTA) is a technique that is analogous to optical TA, but utilizes an optical pump and *X-ray* probe pulse to interrogate excited state dynamics, which has some advantages if simultaneous determination of electronic and nuclear structure is a priority.

1.2. XTA as a tool for studying metalloporphyrin dynamics

Because the X-ray absorption signal originates from the excitation of core-level electrons, XTA is element specific and can selectively probe both the dynamic electronic structure of a metalloporphyrin metal center and its local nuclear dynamics following photoexcitation without interference from ligand-localized transitions.[20-28] Transitions into vacant metal orbitals can be directly excited to assess d-orbital splitting and occupancy, and at probe energies above the core electron ionization energy scattering phenomena impart sensitivity to the local structure surrounding the absorbing atom to a precision of ±0.02Å. XTA can also be measured for samples in solution and has no phase or crystallinity requirements. However, compared to ultrafast optical

and vibrational techniques that use femtosecond (fs) excitation and probe pulses, XTA at 3rd generation sychrotron sources has the disadvantage of poorer time resolution.

To address the question of ultrafast structural dynamics, it is critical to access the time scale on which atomic motions and rearrangements occur. Expanding the capability of X-ray sources into the femtosecond regime, the range into which a single atomic vibrational period will generally fall, is critical to capture chemical processes of interest. The time resolution of transient X-ray spectroscopies at synchrotron sources is generally limited by the temporal width of the X-ray pulse, typically greater than 30 ps, making observation of the fastest nuclear rearrangements on excitation difficult. This limitation is due to the nature of the X-ray pulse-generating electron bunches, the duration of which in the storage ring cannot decrease beyond this limit and retain significant charge and desirable characteristics.

Recently, X-ray free electron laser (XFEL) sources capable of producing femtosecond X-ray pulses[29,30] have become available for time resolved studies.[20] Free electron lasers offer both very bright and very short pulses, though at a lower repetition rate than most conventional sources. While XFEL X-ray pulses have a duration of only 10's of fs and also boast up to 10^{10} photons per pulse when a 1 eV bandwidth monochromator is used, the self-amplified spontaneous emission (SASE) process by which electron bunches are used to generate these X-ray pulses is a highly stochastic process. This "intrinsic instability" results in variation of both the pulse amplitude and energy spectrum from shot to shot, requiring careful normalization. In spite of this, the energy bandwidth of the LCLS beam is sufficient to allow a ~50 eV monochromatic scan, covering the energy range of an absorption edge and making it possible to perform transient X-ray absorption (XAS) experiments.

1.3. Outline of thesis

This work focuses on the description of nuclear geometry and electronic structure dynamics from the femtosecond to microsecond timescale in several metalloporphyrin systems using X-ray Transient Absorption methods. XTA characterization of excited states of Nickel (II) temtramesytlporphryin (NiTMP), the heme active site of Carbmonoxymyoglobin (MbCO), and a series of Zinc (II) porphyrins (ZnP) and Zinc substituted hemoproteins are presented. These systems span a range of structural complexity and ligation environments, from a four coordinate nickel porphyrin lacking axial ligands to a ferrous heme bound in the heme binding pocket of myoglobin through an axial histidine. Due to these different coordination environments as well as varying metal d-orbital occupancy, these systems also represent different modes of metal-porphyrin interaction and the effects of this interaction on excited state dynamics. In the hemoproteins studied here, the effects of the protein environment to influence these dynamics through ligation and other contacts with the porphyrin macrocycle are discussed.

Chapter 2 describes the physical origins of the XAS signal as well as the properties of synchrotron and XFEL pulses. An overview of the experimental scheme for both synchrotron based and XFEL based studies is provided.

Chapter 3 focuses on the femtosecond to picosecond evolution of Ni (II) tetramesitylporphyrin excited states as measured by Ni K-edge XANES at the Linac Coherent Light Source (LCLS). This work captured an intermediate electronic state not previously resolved by synchrotron XAS studies and is among the first examples of XTA implementation at an XFEL. This intermediate

charge transfer state is identified by electronic structure theory and its dynamics are discussed in the context of porphyrin structural changes during relaxation.

Chapter 4 is an investigation of myoglobin heme relaxation following the photodissociation of an axial ligand, carbon monoxide, on the femtosecond to picosecond timescale at LCLS. The evolution of the XAS difference signal at specific energies in the Fe K-edge XANES is interpreted to indicate a rapid spin transition followed by a series of heme structural changes that confer a conformational change to the myoglobin tertiary structure within 1 ps.

Chapter 5 is a synchrontron-based XTA and steady state XAS study of the excited state structures of a series of Zinc (II) porphyrins and Zinc substituted hemoproteins. The first triplet and singlet excited states of these systems are subject to a Jahn-Teller distortion that breaks their in-plane symmetry. This chapter focuses on the role of the asymmetric protein environment to stabilize distortions of the porphyrin.

Chapter 2. X-ray Transient Absorption Spectroscopy at Synchrotrons and XFELS

2.1. Origin of the X-ray absorption signal

2.1.1. Absorption edges

X-ray absorption spectroscopy is based on the excitation of atomic core electrons and measures the pattern of X-ray absorption by a sample surrounding a core electron binding energy for a specific element in that sample. At this binding energy, which depends on element type and the atomic orbital of the absorbing election, there is a step-like increase in the absorption cross section μ(E) as the energy of the X-ray photon becomes sufficient to promote the core-level electron to an unoccupied level above the Fermi energy. This step in absorption is called and "absorption edge". At energies above the ionization energy (E_0), a photoelectron is ejected with increasing kinetic energy as incident X-ray photon energy increases, a result of the well-known photoelectric effect (Figure 2.2). Below the ionization energy, absorption may excite the core electron into an unoccupied valence orbital according to normal dipole selection rules, leading to positive features described as 'bound transitions" on the low energy periphery of the absorption edge (Figure 2.2). Above the ionization energy, the electron is excited to a continuum level.

Absorption edges are named according to primary quantum number and total angular momentum as laid out in Figure 2.1. Depending on the element and identity of the core orbital, absorption edges can fall into the "soft" X-ray region, less than a few keV, or the "hard" X-ray region, between a few keV and 100 keV, and the energies at which edges occur is specific to each element. K-edges, which arise from the excitation of a 1s electron, are the focus of this work and for first row transition metals fall between 4 and 10 keV.

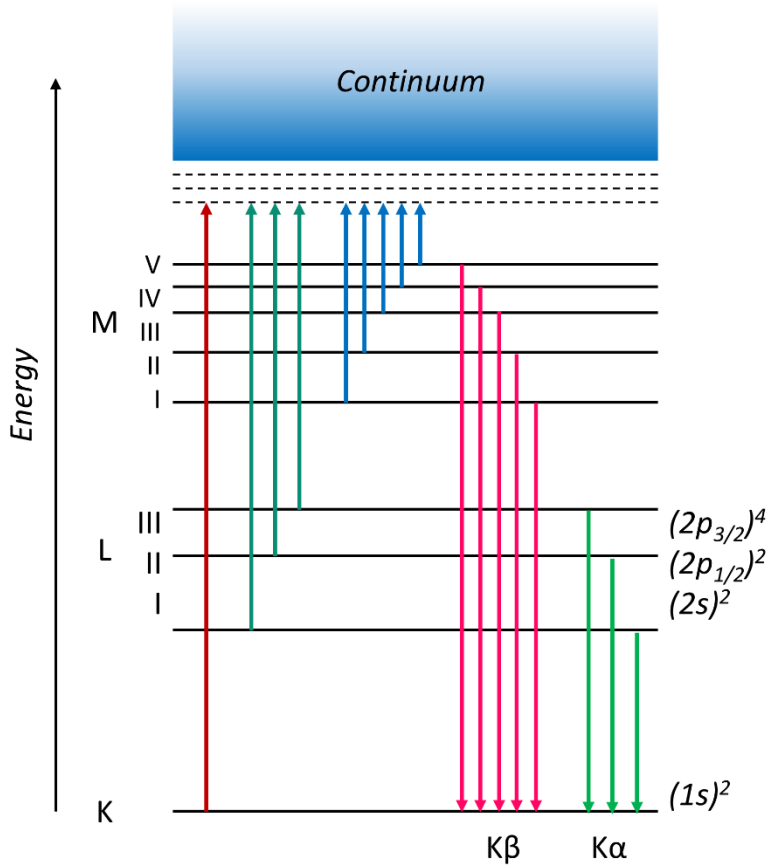

Figure 2.1: X-ray Absorption transitions and X-ray emission lines relevant to K-edge XAS data collection.

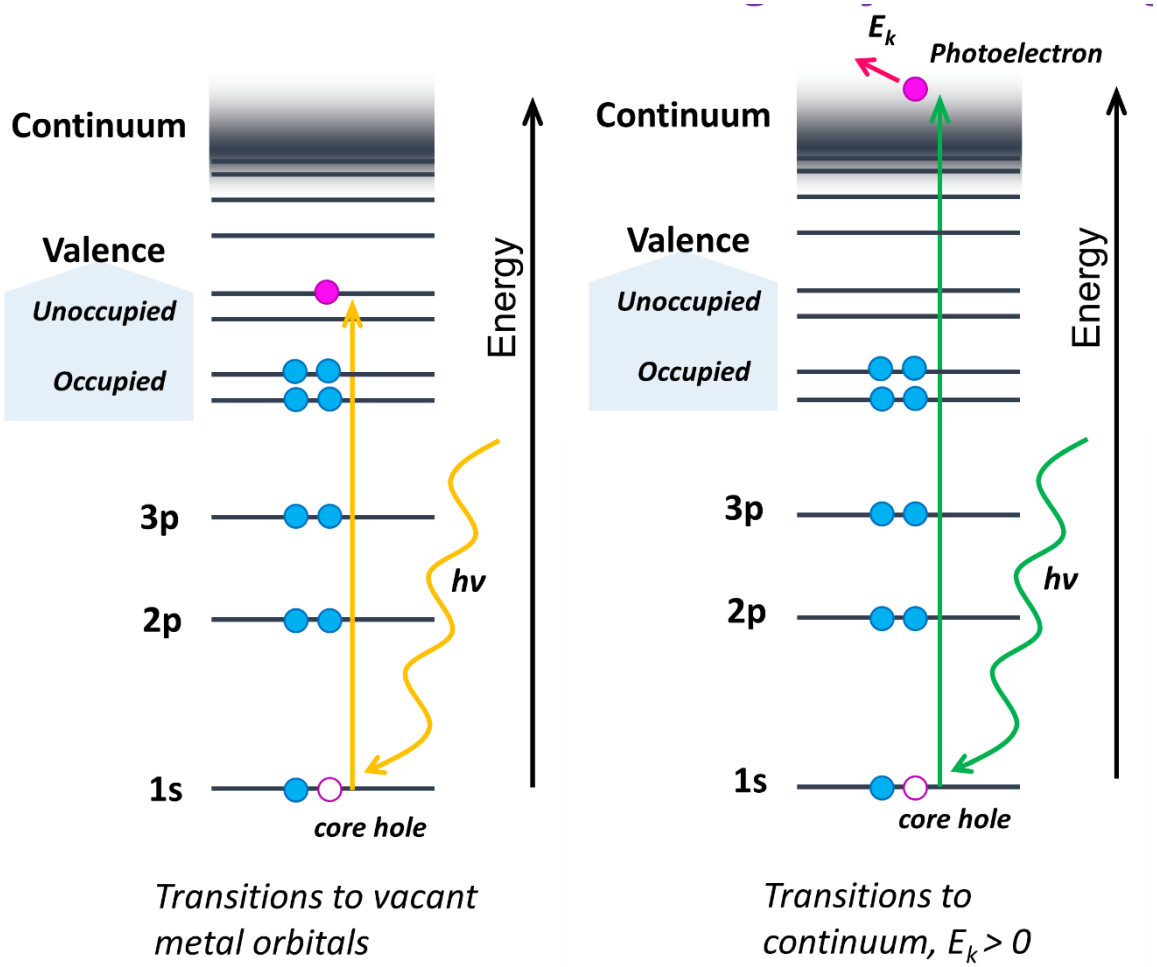

Figure 2.2: (Left) XAS transitions to unoccupied bound states above the Fermi Level but below E_0. (Right) XAS transitions for $E > E_0$, where a photoelectron of energy E_k is ejected.

2.1.2. X-ray Absorption Fine Structure

That the energy region adjacent to the absorption edge is not featureless except for bound transitions of purely metal orbital character is a result of the presence of neighboring atoms to the absorbing atom (the “absorber”). Neighboring atoms alter the electronic structure of the absorber and scatter the outgoing photoelectron wave that is created by absorption, causing what is called X-ray Absorption Fine Structure” (XAFS). These effects on the absorption edge contain a lot of detailed information describing both local geometry surrounding the absorbing atom and the influence of the coordination environment on the absorbing atom’s electronic structure, thus the term “XAFS” is used interchangeably with “X-ray Absorption Spectroscopy (XAS)” because obtaining this information is the goal of XAS.

Because the XAFS depends on the energy of the photoelectron, the absorption edge is typically split into two energy regions which are discussed separately (Figure 2.4): the X-ray absorption near edge structure (XANES), consisting of the region from immediately below the absorption edge to ~50 eV above it, and the extended X-ray absorption fine structure (EXAFS), which are oscillatory features beginning 50 eV above E_0. XANES begins with bound transitions (“pre-edge transitions”) below energies required to generate a photoelectron, which for K edges of 3d metals are typically weakly allowed transitions to vacant 3d orbitals or molecular orbitals with significant 3d character. 1s $\rightarrow$ 3d is a low intensity quadrupole allowed transition, but as the coordination of the absorber deviates from centriosymmetry, mixing with vacant 4p orbitals lends the d orbitals enough p character to become weakly dipole allowed.

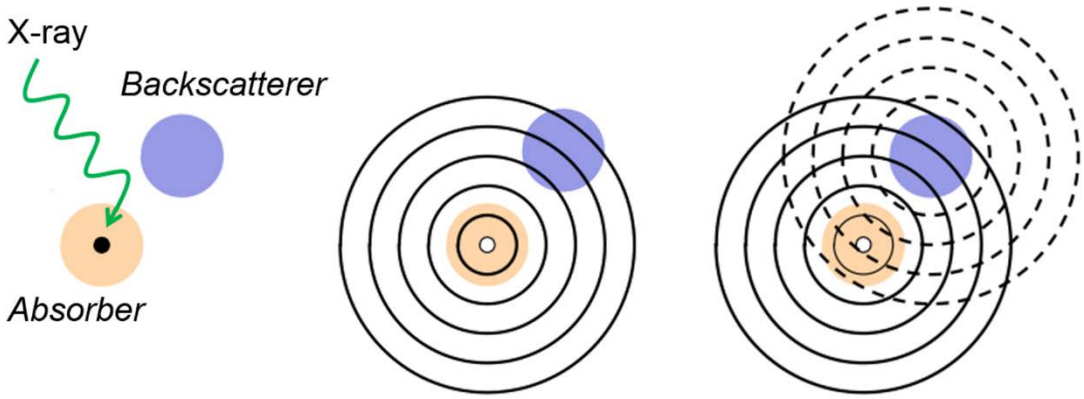

Figure 2.3: Pictorial representation of the ejection and backscattering of a photoelectron after absorption.

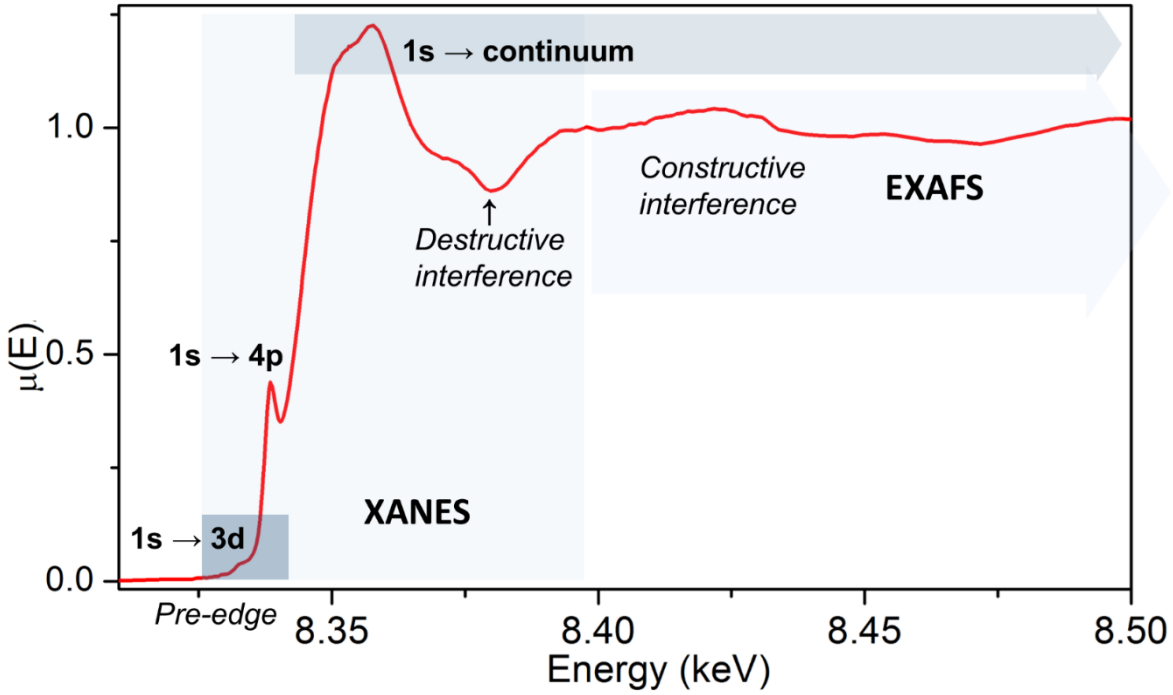

Figure 2.4: A Nickel K-edge with types of transitions and named energy regions shown.

The edge itself consists of transitions to an increasingly high density of bound states and, once above the ionization threshold, transitions to continuum states and contributions from the scattering of low kinetic energy photoelectrons. Much of this scattering is due to multiple scattering events off of neighboring atoms as the low kinetic energy of the photoelectron leads to long photoelectron mean free paths and large scattering amplitudes. Due to the convolution of these electronic and scattering effects on the XANES, it is very challenging to interpret quantitatively and theoretical descriptions of XANES often primarily model either the scattering or electronic contributions.

Conversely, the EXAFS region, beginning at 50 eV above the ionization energy and extending to several hundred eV above the edge, is purely dependent on scattering phenomena. The majority of scatting events are single scattering due to the higher photoelectron energy in this region, which leads to a photoelectron mean free path of a few Å. EXAFS is therefore a local probe of the nuclear geometry surrounding the absorber. The EXAFS signal $\chi(E)$ is defined as the normalized oscillatory part of the absorption coefficient $\mu(E)$:

$$\boldsymbol{\chi(\mathbf{E}) = \frac{\mu(\mathbf{E}) - \mu_0(\mathbf{E})}{\mu_0(\mathbf{E})}} \qquad 2.1$$

where $\mu_0(E)$ is the edge step in the absence of scattering effects. Typically χ is expressed in terms of the photoelectron wavevector k and EXAFS data is reported as the transformation of the photon energy minus the ionization energy E_0 into k-space:

$$\boldsymbol{k = \frac{\sqrt{2m(E - E_0)}}{\hbar}} \qquad 2.2$$

where m is the electron mass.

XAFS data pre-processing involves a few standard steps to normalize the edge step and extract the EXAFS signal that are briefly described here. Quadratic functions are fit to the region before the rising edge and beginning ~50 eV after E_0 and the data is "flattened" and normalized such that the difference between the pre and post edge lines $\Delta\mu(E) = 1$. This eliminates any sloping background from the XAFS and allows for comparison of the XANES for different species, but requires that some data after the edge step is taken. The EXAFS region is then transformed into k-space according to equation 2.2 and weighted by a power of k to emphasize oscillations at high k where the EXAFS signal is damped, typically either k^2 or k^3, with the goal being oscillations with even amplitude over the region that is subsequently Fourier transformed. A window in k for the Fourier transform is chosen based on data quality and the data is reported in R-space as the magnitude, real part, or imaginary part of the Fourier transform. While R values do not exactly reflect the absorber-backscatterer distances due to the interaction of the photoelectron with the backscatterer potential, these R plots are analogous to radial distributions functions of atoms about the absorber.

2.1.3. A brief physical description of XAFS

The x-ray absorption coefficient is proportional to the transition probability of photoelectric absorption at a given energy, which Fermi's Golden Rule describes as dependent on the initial state and final state wavefunctions:

$$\boldsymbol{\mu(E) \propto |\langle f|H'|i\rangle|^2 \delta(E_f - E_i - \hbar\omega)} \qquad 2.3$$

where the final and initial states are represented by *f* and *i*, *H'* is the interaction Hamiltonian between the X-ray's electromagnetic field and the electrons and δ is the density of states. While

the initial state is the localized core level, the final state is a photoelectron wave propagating from the absorbing atom which is backscattered by a neighboring atom to generate incoming photoelectron waves. The interference between the outgoing photoelectron and this backscattered photoelectron at the absorbing atom modulates the matrix element $\langle f|H'|i\rangle$ that determines the strength of the transition from *i* to *f*. With changing incident photon energy, the changing frequency of the photoelectron results in different levels of constructive and destructive interference at the absorber, modulating μ(E) with an oscillation the frequency of which depends on the distance between the absorber and backscatterer.

While a photoelectron defined only by its kinetic energy has no restrictions on its angular momentum, dipole selection rules govern the angular momentum of the photoelectron final state for XAS transitions and photoelectron emission is not isotropic. For K-edges, the ejected photoelectron has p character and is aligned with the polarization direction of the X-ray electric field. The photoelectron emission probability depends on the angle between the emission direction and the polarization of the electric field vector as:

$$\boldsymbol{P(\theta) \propto 3cos^2\theta} \qquad 2.4$$

In the EXAFS region where single scattering events between pairs of atoms dominate the signal, the spectrum can be modeled as the sum of these oscillations which each correspond to a single absorber/backscatterer pair, or *scattering path.* This sum is formalized as the EXAFS equation:

$$\boldsymbol{\chi(k) = \sum_i \frac{N_i S_0^2}{kR_i^2} f_i(k) e^{-2k^2\sigma_i^2} e^{2R_i/\lambda(k)} \sin[2kR_i + 2\delta_c(k) + \delta_i(k)]} \qquad 2.5$$

Where i is the scattering path index, N_i is the degeneracy of the scattering path, R_i is the absorber to backscatterer distance, and S_0^2 is an amplitude reduction factor.σ^2 is the Debye-Waller factor, a measure of vibrational and rotational disorder, and the $e^{-2k^2\sigma_i^2}$ term accounts for atomic motion. The $e^{2R_i/\lambda(k)}$ term accounts for the decay of the photoelectron due to elastic losses where $\lambda(k)$ is the mean free path of the photoelectron. The $\sin[2kR_i + 2\delta_c(k) + \delta_i(k)]$ term describes the oscillations themselves, whose frequency depends on $2kR_i$ and which are shifted in phase by factors describing the interaction potentials of the photoelectron with the absorber, $2\delta_c(k)$, and the backscatterer, $\delta_i(k)$. This potential depends on Z for both atoms and can be used to distinguish backscatterer atomic number.

2.1.4. X-ray fluorescence

After X-ray absorption, the absorbing atom is left with a highly unstable core level hole. Relaxation of this excited state occurs within femtoseconds by both radiative and non-radiative processes, though in this work we will focus on the former. Radiative decay takes the form of X-ray fluorescence where outer shell electrons of the absorbing atom relax to fill the inner shell vacancy. X-ray emission lines for relaxation into a 1s hole ("K" emission) are shown in Figure 2.1. The fluorescence yield ε_f for a given emission line is defined as the ratio of the emitted x-rays to the number of core level vacancies created by X-ray absorption, and because of this linear relationship the measured x-ray fluorescence I_f also has a linear relationship with the X-ray absorption cross section of the absorber:

$$\boldsymbol{I_f = I_a * \frac{\Omega}{4\pi} * \frac{\mu}{\mu_T} * \eta} \qquad 2.6$$

Where I_a is the number of X-ray photons absorbed, Ω is the solid angle collected, μ is the absorption cross section of the absorber, μ_T is the absorption cross section from the total sample absorption, and η is the quantum yield of fluorescence. For dilute samples where the absorption of the emitted fluorescence by the sample itself ("self-absorption") is minimal, $\mu(E)$ is linearly proportional to I_f normalized by the intensity of the incident X-ray beam I_0. Detecting the XAS signal via X-ray fluorescence at 90^o with respect to the incoming X-ray beam is usually denoted "fluorescence mode detection" to distinguish between measuring the transmitted intensity of the X-ray beam and is the standard for dilute solution samples.

2.2. Synchrotrons and XFELS as sources of pulsed X-rays

The X-ray beam generated by 3^{rd} generation synchrotron sources, such as the Advanced Photon Source (APS) where all sychrotron based measurements in this work were performed, and by XFELs such as LCLS is inherently pulsed, although the generation of pulsed X-rays in either case has different physical origins that have large consequences for pulse characteristics. Because XTA is a pump-probe method that distinguishes between X-ray pulses, characteristics of individual pulses are extremely important. At synchrotrons, electrons are first generated by the heating of a cathode and accelerated by a linac (the "electron gun"). They are injected into and further accelerated by a small booster ring to the energy at which they will be stored and injected into the larger storage ring, where X-rays are generated. The storage ring consists of a series of straight and arched sections. X-rays are generated from insertion devices in straight sections and bending magnets in the arched sections that deflect the X-rays into the next straight section. The insertion devices (or "undulators") are periodic arrays of alternating magnetic poles that force the electrons

into an oscillatory path in the plane of the storage ring, generating horizontally polarized X-rays as the undulators periodically modulate the electron acceleration.

Radio frequency (RF) cavities in the electron beam path supply energy to the beam lost during X-ray generation and are responsible for the “bunching” of electrons in the storage ring and therefore the pulsed nature of sychrotron radiation. The RF creates a standing electric field within the cavity and therefore only electrons with the correct phase with respect to the RF receive a boost in energy. This forces the electron beam into bunches with well-defined separation in time that depends on the RF frequency. All synchrotron XTA experiments in this work were performed in 24-bunch mode, where the total ring charge is split into 24 electron bunches. Each bunch cycles the ring with a 278 kHz repetition rate, resulting in a temporal separation between bunches of 153 ns.

While free electron lasers operate on many of the same principles, the timing structure of the X-ray pulses is dependent on the characteristics of the electron beam generated by the initial injection, linear acceleration, and X-ray generation as opposed to equilibrium conditions determined by the replacement of lost energy by RF cavities. At LCLS a pulsed electron beam is produced by irradiation of a cathode with a pulsed drive laser. The electron bunches are further compressed to ~50 fs in duration with magnetic chicances and accelerated in a linac. As the electron bunches traverse a long series of undulators (~60 m compared to 2-4 m undulators at synchrotrons) they begin to emit low intensity, out of phase x-rays. The power P of the emitted radiation follows the relationship $P = NP_1$, where N is the number of electrons and P_1 is the power emitted by a single electron. As more X-rays are emitted, the electrons begin to experience an increasing radiated field, causing some electrons to gain and others to lose energy. This leads to an

electron density modulation through the duration of the pulse with and period equal to the wavelength of radiation emitted, called “micro-bunching”. Micro-bunching initiates a positive feedback process as the temporally bunched electrons radiate in phase with behavior that resembles a single point charge. The emitted field can therefore be described as $E = NE_1$ and the radiated power as $P = N^2P_1$, resulting in an exponential increase in intensity. This process is called self-amplified spontaneous emission (SASE) and is inherent stochastic.[31] After X-ray generation, compressed electron bunches are simply dumped from the linac.

Because electron bunch energy, duration, timing are not set by equilibrium conditions as in synchrotrons, large pulse-to-pulse variations of the X-ray pulse in intensity, arrival time, and the central energy of the pulse bandwidth exist, causing some complications in the treatment of XFEL XAS data. While XFEL pulses possess some energy bandwidth between 20 and 100 eV depending on the central energy, the pulse spectrum is extremely “spikey” because certain discrete energies are enhanced in the SASE process. The repetition rate of XFEL pulses is set by the drive laser, and in all work presented here is 120 Hz, but there is also significant pulse-to-pulse timing jitter about the average arrival time. Characterization of the pulse intensity and arrival time is therefore needed for each individual pulse and care must be taken in the treatment and averaging of data to avoid the unnecessary reduction of the time resolution and the increase in standard error of the normalized XAS signal at each time point. Data treatment is described in detail in the methods sections of Chapters 3 and 4.

2.3. Generalized experimental scheme

XTA experiments at both synchrotrons and XFELs require the same basic components. The layout of the X-ray hutches at APS, beamline 11-ID-D (Sector 11, Insertion device, Station D) and LCLS, end station XPP (X-ray Pump probe), where all XTA experiments described here were conducted, share many instrumental modules that accomplish similar functions. A generalized experimental scheme is therefore laid out here while more technical details specific to each experiment are described in the appropriate chapter.

Upon generation of the x-ray beam, a pair of Si(111) crystals generates a monochromatic beam from the bandwidth of the incoming beam. The bandwidth of sychrotron radiation is much broader than that generated by SASE, which for the energy ranges in this work is about 50 eV, though in both cases the peak intensity can be tuned in energy by modulation of the undulator gap. The monochromator angle is rotated to scan across this bandwidth and collect the energy dependent XAS signal. On entering the X-ray hutch, the beam passes through an intensity monitor and focusing optics to control beam size. At 11-ID-D these consist of ionization chambers to detect beam intensity and an X-ray mirror to produce a vertically focused 200 by 500 μm spot, while at LCLS they are diodes pointed at an X-ray fluorescent screen and a series of beryllium lenses respectively. The beam then passes through a set of slits and just before the sample chamber there is photodiode that measures the intensity of individual pulses so that XAS signal normalization can be done on a pulse-by-pulse basis. At 11-ID-D, this is an avalanche photodiode (APD) that collects X-ray scattering from air, while at LCLS it is a diode pointed at a fluorescent screen. While the pulse-to-pulse variations in intensity as a percentage of average intensity are much lower at APS, this normalization process has the advantage at a sychrotron of accounting for “top up”,

where charge is periodically refilled for a given electron bunch by the APS injection system, resulting in a small increase in intensity.

The X-ray beam then enters the sample chamber, where it interacts with the sample, typically a vertical round liquid jet. Samples for XTA are chosen and prepared such that the optical absorption at the chosen excitation wavelength is not too high to prevent excitation through the entire thickness of the jet, but the concentration is at least 1 mM in the absorbing metal. The jet is collected through a port in the bottom of the sample chamber connecting it to a sample reservoir from which the sample is recirculated with a peristaltic or HPLC pump to the nozzle at the top of the sample chamber which forms the jet. The sample chamber is a closed system that is constantly purged with He of N_2, and all ports to admit detectors, the jet, etc. are sealed to prevent leakage of oxygen.

Detection is done in florescence mode with two photodiodes at 90^o with respect the incoming beam to avoid Compton scattering. Photodiodes used in XTA experiments have fast enough response times to resolve individual X-ray pulses but are total yield detectors, making them susceptible to background signals from elastic scattering of the X-ray beam. A combination of z-1 filters and soller slits are used to minimize this effect. Z-1 filters are thin sheets of metals oxides of the atomic number z-1 where z is the absorbing element. For 3d metals, X-ray emission is lower in energy than the absorption edge of the z-1 element, while the absorption edge of the absorbing metal is higher. Thus z-1 filters transmit the absorbing element’s fluorescence while absorbing elastic scattering. Soller slits are cones of overlapping blades the physically block photons scattered from angles other than the point of X-ray/laser overlap on the sample. Pulse by pulse normalization of the X-ray fluorescence signal is done internally by the electronics that control

data collection at 11-ID-D using not just the total detected signal but fitted lineshapes for the voltage vs time traces recorded by each photodiode to reduce noise. This requires the collection of both X-ray off “dark” and X-ray on “reference” lineshapes before data collection.

At APS, the excitation pulse is triggered off of the RF signal output of the APS itself, allowing for synchronization of the pump pulse with the X-ray pulse generated by the same electron bunch (the “synchronization bunch”) for every repetition of the laser, although due to the differential between the synchrotron and laser repetition rate, several thousand X-ray pulses pass between pump pulses and some of these can be integrated for long lived excited states. Conversely, the laser systems at LCLS match the repetition rate of the XFEL.A delay stage controls the relative delay between the pump pulse and synchronized X-ray pulse.

Chapter 3. Ultrafast Excited State Relaxation of a Nickel(II) Porphyrin Revealed by Femtosecond X-ray Absorption Spectroscopy

3.1. Introduction

Nickel porphyrins and phthalocyanines have been of particular interest as model complexes to provide guidance for targeted molecular design in part due to their conformational flexibility brought on by the small Ni core size and the ease with which certain ring conformers can be stabilized to tune relaxation kinetics. Nickel (II) tetramesitylporphyrin (NiTMP), which exists in the ground state as an ensemble of ring conformers, and its analogs, have complicated photochemical dynamics and have been extensively studied by optical absorption[32,33] and Raman spectroscopy.[34-39] These studies, combined with quantum-mechanical calculations, proposed a plausible pathway for the photoexcitation. Within 20 ps of the photoexcitation that initiates the $S_0 \rightarrow S_1$ transition, a porphyrin macrocycle based $\pi \rightarrow \pi^*$ transition, the electron promoted to the π^* orbital moves to an empty $3d_{x2-y2}$ orbital, the highest energy ligand field state for a square-planar complex, and an electron from an originally filled $3d_{z2}$ orbital moves to fill the hole in the π orbital of the macrocycle left by the initial photoexcitation, resulting ultimately in the lowest-lying triplet state, ($3d_{z2,}$ $3d_{x2-y2}$). This state has a 3d electronic configuration of $(3d_{x2-y2})^1(3d_{z2})^1$ and is here denoted T(d,d) (Figure 3.1).[34,40] A pump-pump-probe transient absorption measurement of Ni(II) porphyrin excited state dynamics suggested that a transient Ni(I) charge transfer state may exist with a lifetime of a few picoseconds,[33] but previously such a reaction pathway could not be substantiated by monitoring the temporal evolution of the nickel electronic configuration.

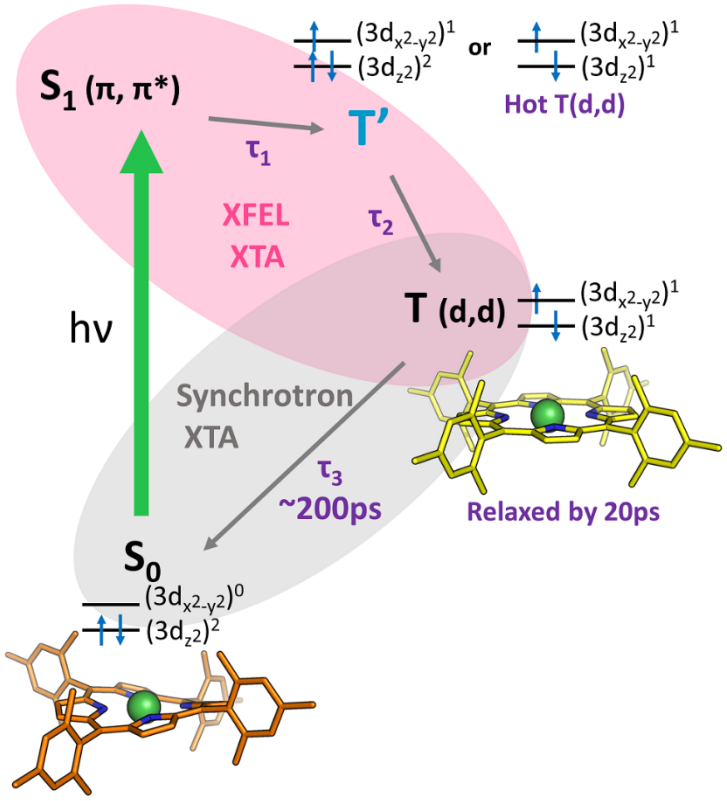

Figure 3.1: The relaxation pathway of NiTMP following Q-band excitation (e.g. at 527 nm). Structures for states characterized by XTA are shown. Within a few ps the porphyrin macrocycle S1(π, π*) population has dissipated by transfer of the excitation to the metal center. The resulting state (T') is therefore either a hot (3dz2, 3dx2-y2) state which decays to the relaxed (3dz2, 3dx2-y2) state T(d,d) via vibrational relaxation or a (π, 3dx2-y2) state with Ni(I) character that transfers an electron back to the ligand. By 20 ps the T(d,d) state is fully populated and vibrationally relaxed, and has adopted a flattened structure with elongated Ni-N bonds.[41] This T(d,d) state decays back to the ground state with a 200 ps lifetime.[32]

In comparison to these previous optical and vibrational spectroscopic studies, X-ray transient absorption (XTA) spectroscopy,[20,21] which combines a laser excitation and conventional X-ray absorption spectroscopy,[42] can directly probe the metal center electronic structure and local geometry rather than relying on the indirect deduction of excited state dynamics from relatively broad transient optical spectral features.

Previous XTA studies at a synchrotron source (the Advanced Photon Source, Argonne National Laboratory) with ~100 ps time resolution[1,2] have conclusively verified that the thermalized excited T(d,d) state has an $(3d_{x2-y2})^1(3d_{z2})^1$ electronic configuration, and have captured this state's elongated Ni-N bond length and flattened macrocycle conformation through analysis of the Extended X-ray Absorption Fine Structure (EXAFS), which arises from scattering processes with atoms neighboring the absorbing Ni.[14,41,43] However, the time resolution of the synchrotron X-ray pulses was insufficient to detect detailed excited state structural dynamics before the development of the relaxed T(d,d) state. In this study, this missing time window in the evolution of excited Ni(II)TMP is obtained by collection of XTA spectra near the nickel K-edge (8333 eV) with the sub-picosecond time resolution provided by the Linac Coherent Light Source (LCLS), an X-ray free electron capable of delivering femtosecond X-ray pulses of incredible intensity.[26,44] This study has in fact disclosed a transient charge transfer state, denoted **T'** for consistency with previous work,[45] that occurs prior to the appearance of T(d,d) (Figure 3.1) and, importantly, the X-ray absorption near edge spectra (XANES) of electronic states and geometries in the proposed photochemical trajectory were calculated and the effects of different orbital occupancies, Ni-N bond lengths, and the magnitude of repulsive potential acting on the Ni 1s electrons were correlated with trends in the experimental spectra.

3.2. Methods

3.2.1. Ultrafast XANES spectroscopy.

Ultrafast XANES spectra were collected for an 8 mM solution of NiTMP in toluene at the X-ray Pump-Probe (XPP) instrument of the LCLS[46] using a similar experimental configuration as previous XANES measurements at XPP.[26] The sample solution was delivered to the point of spatial X-ray/laser overlap within a nitrogen filled chamber as a flat 100 μm liquid jet angled at 45^{o} with respect to the incoming beam, where a pulsed laser beam nearly collinear with the incoming X-ray beam intersect. Each laser pulse generates an excited population probed by an X-ray pulse at a specified delay time with a "pump-probe" cycle of 120 Hz. A 527 nm excitation pulse from the output of an optical parametric amplifier (OPA) pumped by a Ti:Sapphire laser with a pulse duration of 50 fs (FWHM) was used to excite NiTMP through the porphyrin macrocycle centered $S_0 \rightarrow S_1$ ($\pi \rightarrow \pi^*$) transition. The laser pulse energy at the sample was between 15 and 18 μJ with a spot size of ~0.3 mm diameter. At this pulse energy, simultaneous two-photon absorption (TPA) is not expected to contribute meaningfully to the excited XAS signal due to the low TPA cross section noted for symmetrically substituted porphyrins at this energy (~10 GM). Under these excitation conditions, the TPA excitation rate is less than 1% of the linear absorption transition rate. The absorption of the S1 state at the Q-band is very weak for similar porphyrins and sequential two photon absorption is similarly discounted.

Ni K-edge (8.333 keV) XANES spectra were collected at specific pump-probe time delays by scanning a Si(111) double crystal X-ray monochromator, which at this energy has a resolution of 1.2 eV, across the XFEL spontaneously amplified stimulated emission (SASE) bandwidth. The

~50 fs pulse duration X-ray probe pulses have significant bunch-to-bunch spectral and temporal fluctuations due to the variation in electron bunch characteristics, resulting in a time-integrated energy bandwidth of ~50 eV at the Ni K-edge. The peak intensity position of this distribution was tuned to the X-ray photon energy at the center of the Ni K-edge to optimize X-ray flux in the energy region of interest. The monochromatic X-ray beam was focused to a ~0.1 mm diameter spot at the sample with a series of Beryllium lenses. To obtain the kinetics at a specific energy, scans of the pump-probe delay were performed at fixed photon energies. For both scan types, the XANES signal for each individual X-ray pulse was collected at the 120 Hz repetition rate of the X-ray pulse and integrated for two seconds for a total of 240 single pulses per point.

XANES spectra were collected via Ni K_α X-ray fluorescence using two solid state passivated implanted planar silicon (PIPS) point detectors (Canberra, Inc.) at 90^o with respect to the incoming X-ray beam. To minimize the contribution of background counts for each fluorescence detector, the majority of the elastic scattering photons were blocked by a cobalt oxide filter mounted on a Soller slit designed for a fixed distance between the detector and the sample liquid jet (6 mm) and placed in front of each detector diode. The incoming monochromatic X-ray pulse intensity was monitored for later pulse-by-pulse signal normalization by another PIPS detector located upstream of the sample chamber. XANES spectra were obtained for pump-probe delay times from –5 ps (where the X-ray pulse precedes the laser pulse) to 100 ps to obtain spectra for both a fully ground state population and for a comparable T(d,d)-ground state population mixture measured in previous experiments limited temporally by the 100 ps pulse of APS.[14,41] XANES scans were smoothed with the locally weighted regression method using the number of local data points about each energy equal to 5% of the total number of points to fit the regression. Due to variation of

energy step size through the scan, the energy window used in smoothing is therefore 0.6 eV, 1.8 eV, and 6.6 eV respectively for the pre edge, $4p_z$, and white line regions of the scan, comparable or less than the 1.2 eV energy resolution of the Si(111) monochromater where sharp features are interpreted.

UV-Vis absorption spectra of the sample taken before and after the XTA experiment were identical, verifying the integrity of the sample throughout data collection and discounting any contribution of irreversible damaging processes (e.g. interactions with solvated electrons, demetalation of the porphyrin, etc.) to the transient signal.

3.2.2. Characterization of XFEL pulses and the XAS signal.

The stochastic nature of the XFEL pulse energy distribution and temporal jitter require additional characterization of both the incoming X-ray pulse and the X-ray fluorescence signal at the sample. For each scan step, 240 individual shots were collected and characterized according to initial intensity (I_0) and fluorescence detector response (D_1 and D_2). The XAS signal amplitude at each energy step was determined from the average of normalized shots after rejection of selected individual shots when the normalized XAS signal deviated significantly from the median XAS value as described below. To account for timing jitter in the X-ray pulses, individual shots were re-binned in time for time delay scans according to up-stream diagnostic RF cavities (“phase cavities”) that record the average electron bunch arrival time (see Methods 3.2.4). Importantly, this serves to account for the long-term drift in the average pulse arrival time relative to the laser delay and replaces and reduces the contribution of the timing jitter to the overall time resolution with the uncertainty in the phase cavity response. After phase cavity re-binning, the time resolution of the

experiment was reduced from an estimated 400 fs to 300 fs based on the FWHM of the Gaussian instrument response function obtained as a fitted variable in the fits of the time delay scans.

3.2.3. Data reduction, correction, and filtering

The shot-by-shot variation in intensity and energy for XFEL pulses necessitates calculation of the XAS signal for each individual pulse as well as further characterization of the distribution of certain crucial parameters for all pulses to enable filtering of outliers and improvement of the S/N. Channels of primary interest are the non-invasive beam intensity monitor upstream of the sample chamber (I_0) and two chamber mounted PIPS diodes that detect X-ray fluorescence signal (D_1 and D_2).

The “spikey” nature of the SASE XFEL spectrum as well as its limited energy bandwidth leads to both an amplification of the noise in the shot intensity due to variation in the central energy of the pulse when the beam is monochomatized, and to occasional large jumps in intensity when the monochromater energy is aligned with a spike. The result is a distribution of shot intensities with outliers at as much as 600% of the median intensity. For each scan step in energy or delay, for which 240 shots are collected during a two second integration time, any zero intensity shots are eliminated. The X-ray fluorescence signals from detectors D_1 and D_2 are then normalized for each shot by the corresponding I_0 intensity to obtain the single-shot XAS signal. Outliers above a high threshold of 100 times greater than the median XAS signal for all shots are subsequently removed from the data set.

Further filtering of shots is accomplished by first constructing linear fits of the D_1 and D_2 shot data vs. I_0. Lower and upper rejection limits are defined as linear functions with the same slope as

the D1 or D2 vs. I_0 fit, but offset in the Y-axis about the fit line by two times the standard deviation of the D_1 or D_2 signal data for all 240 shots (light teal and purple regions in Figure 3.2). This minimizes over-rejection of shots for lower-signal energies, such as in the d-orbital transition region, while eliminating shots too far from the median XAS signal at each energy.

3.2.4. Phase cavity timing correction

Variation in the shot arrival time contributes significantly to the temporal broadening of the instrument response. In addition to this, the average shot arrival time displays some long term drift, resulting in the shift of the XAS difference signal rise with respect to the previously defined “time 0”. Two resonant RF cavities (phase cavities) positioned upstream of the experiment in the electron beam are excited by individual electron bunches and record approximate arrival times as an induced periodic electric field.[47]

The relationship between the recorded phase cavity electron bunch arrival times and the actual X-ray pulse arrival times at the sample itself is informed by a dataset taken during a separate experiment several days prior but sharing all X-ray timing characteristics. Due to the use of the polychromatic beam for this previous experiment, the precise bunch-by-bunch timing diagnostics provided by the then recently implemented laser/X-ray autocorrelator was available before the tool was optimized for the lower flux of the monochromatic beam used in the XAS experiment. A fit of the Timing tool vs. phase cavity arrival times yields a linear relationship that is then applied to the XAS experiment’s phase cavity data, providing a timestamp for each shot that can be used to re-bin them in time (Figure 3.4).

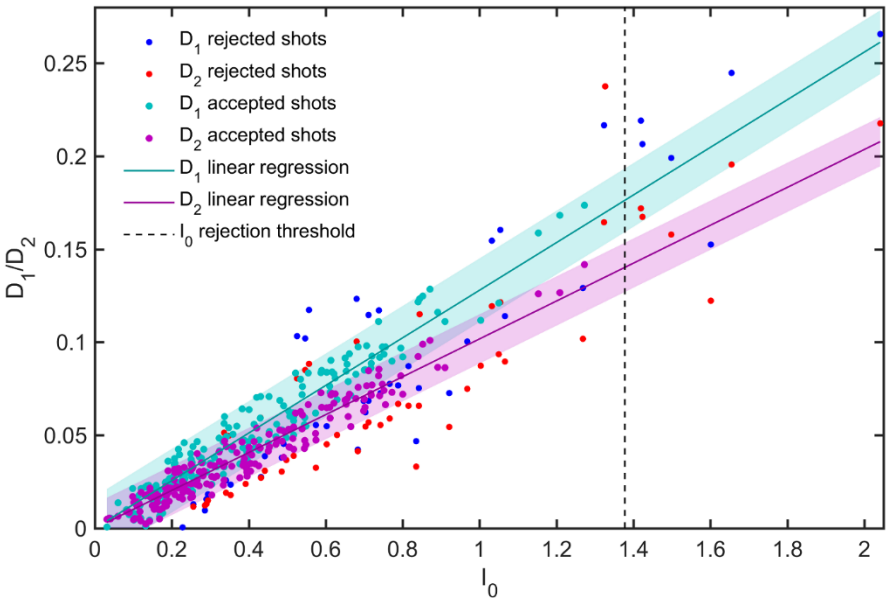

Figure 3.2: Correlations between X-ray detectors for all shots collected in a single scan step (8343 eV) after initial rejection of zero events and extreme XAS signal outliers. Linear regressions of fluorescence detectors D_1 and D_2 vs. the normalization signal I_0 are plotted with filtering limits (+/- 2 standard deviations of D_1 or D_2 for all shots) for each detector.

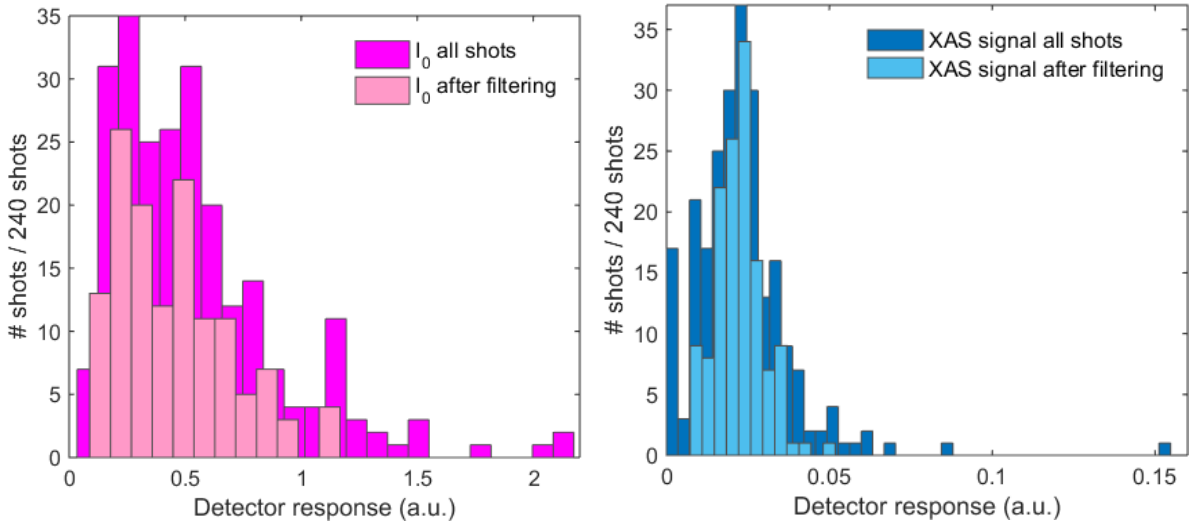

Figure 3.3: Histograms for all shots collected in a single scan step (8337 eV). (A) I_0 values before and after the filtering process described above. (B) Shot-by-shot calculated XAS signal using an average of D_1 and D_2 values before and after filtering.

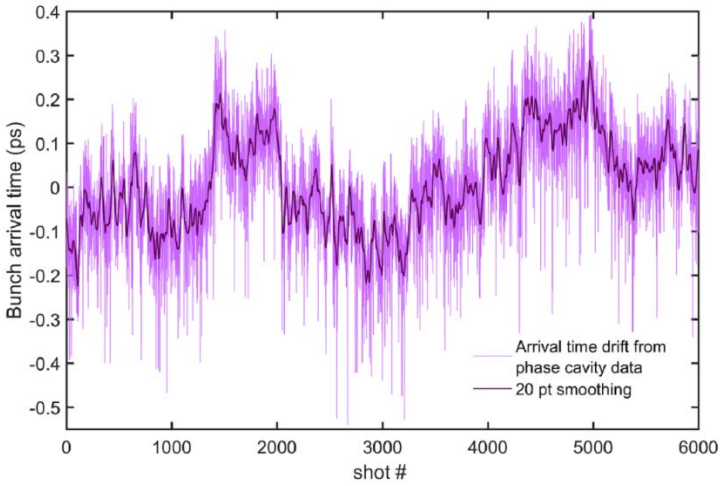

Figure 3.4: The drift of the bunch arrival time about the nominal time 0 during a scan, where the corrected bunch arrival time is obtained from the phase cavity correction.

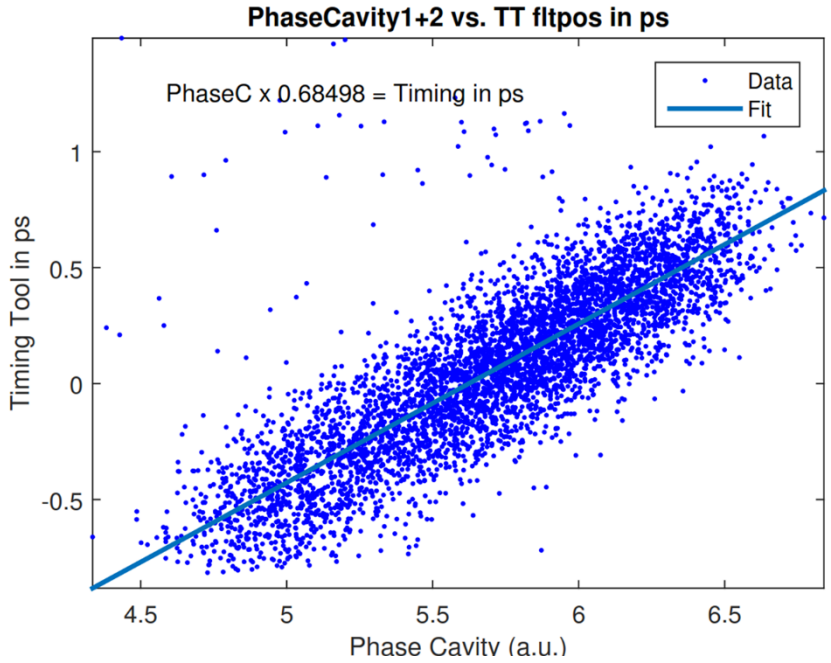

Figure 3.5: The correlation between recorded phase cavity bunch arrival times and precise arrival times obtained from the laser/X-ray autocorrelator ("timing tool"). This correlation is used as a calibration curve to calculate bunch arrival times from phase cavity data when the autocorrelator was unavailable.

Re-binning delay-scan shots according to this relationship results in a faster rise time at the energy with the most prompt rise, 8341 eV. Both the slope and the offset of this linear correction were optimized to obtain the shortest rise time at 8341 eV, but differences in the rise time between the optimized parameters and those obtained from the timing tool data are negligible. Based on the global kinetics fit to delay scans at all energies in which the width of the instrument response Gaussian is fit as a variable, the instrument response after Phase-Cavity re-binning is estimated at about 300 fs FWHM. This is due to 1) imperfect correction of the timing jitter using the phase cavity technique, 2) noise in the response and fitting of the electron bunch arrival time as measured by the phase cavities, and 3) the relative temporal broadening of the X-ray pulse compared to the optical pulse as it travels through the liquid jet due to the difference in the index of refraction of water for optical and X-ray pulses, contributing an estimated 1 fs per μm of solvent (140 fs in this case) to the broadening of the IRF.

3.2.5. Sample excitation conditions and excited state fraction

A careful assessment of the laser spot measured during the experiment (by monitoring X-ray fluorescence during a scan of the laser position across the X-ray spot at a time delay and energy associated with a large XANES difference) give us a ~300 um x 250 um spot. The extinction coefficient of the sample at 527 was 12500 $M^{-1}cm^{-1}$. For a pulse width of 50 fs and pulse energy of 18 μJ, the peak intensity is 524 GW cm^{-2}. At this pump intensity, the number of photons per area on the jet times the jet absorption cross section (Jσ) is ~1.5 and stimulated emission is expected to limit the absorption excited population, although the decay of the initially excited S_1 state is sufficiently rapid to allow for a slightly higher than 50% excitation fraction.

In previous work at a synchrotron source,[48] we determined the T(d,d) state fraction by subtracting the remaining ground state contribution at ~100 ps delay judging by the disappearance of the ground state 1s → 4pz peak, which yielded an average ~40% excited state population at 100 ps. Such a subtraction is based on a two-state model, S_0 and T(d,d). Because the X-ray pulse duration at the time was ~100 ps, the initial excitation population should be higher than 40%. Considering the T(d,d) state has a lifetime of ~200 ps, the initial excited state fraction should be about 60 ± 10% assuming that the temporal overlap between the laser and X-ray pulses was optimal. Comparison of this previous data set to the 100 ps time delay in this experiment presented in the main text yielded a very similar excitation fraction for the ultrafast XANES.

Because of the higher time resolution realized at the LCLS, a three-state model with S_1, T' and T(d,d) states must be employed as described in our manuscript. Thus, we chose to analyze the data using the difference spectra as shown in the main text. If we assume that the T(d,d) state XANES spectrum obtained from the previous synchrotron data is correct, the initial excited state fraction is also about 60% in the LCLS data. A greater than 50% yield (since our excitation fraction is ultimately limited by stimulated emission) is enabled by some relaxation to lower energy excited states within the pulse duration, which allows further $\pi \rightarrow \pi^*$ excitation. It should also be noted that this estimation of the excited state population is relatively imprecise and an uncertainty of +/- 10% is expected. Our analysis of the lifetimes involved in $S_1(\pi, \pi^*)$ decay are in line with about 5% population conversion to T'(π, d) within the optical pulse.

However, because our fitting of the kinetics relies on the XANES difference, the lifetimes extracted from this analysis are independent of the excitation fraction, assuming there are negligible nonlinear optical effects, such as two-photon absorption, or effects on the transient

signal that are a result of the moderately high laser fluence, e.g. irreversible damage to or de-metalation of the porphyrin or interactions with solvated electrons.

3.2.6. Global analysis of single energy time-delay scans.

To obtain kinetics for the NiTMP XANES evolution, pump-probe delay scans at selected characteristic X-ray photon energies were performed, primarily at those energies showing the largest signal amplitudes in the difference XANES spectra (Figure 3.6C). These kinetic traces were fit globally to simulated traces assuming a sequential kinetic scheme to describe the excited state decay, $S_1 \rightarrow T' \rightarrow T \rightarrow S_0$. Starting with the assumption of a simple three step sequential model, delay scans at all energies were simultaneously fit using a non-linear least squares method to obtain seven parameters: 1) time constants for all three processes 2) the absorption of the T' state at each energy and 3) the width of the instrument response function. The least squares method compares simulated traces generated as described below using starting values for fitted parameters, and minimizes the residual between the experimental and simulated data by varying the parameters used to calculate the simulated trace. The simulated trace is an absorption-weighted sum of the population evolution of each species. First the population of each species as a function of time is calculated by numerical integration of a system of differential equations; the differential rate expressions that describe the rate of change of each species' population included in the kinetic scheme, which depend on the fitted τ_1, τ_2, and τ_3.

$$\frac{dP_{S_1}}{dt} = -\frac{1}{\tau_1} * f_{S_1}(t) \qquad 3.1$$

$$\frac{dP_{T'}}{dt} = \frac{1}{\tau_1} * f_{S_1}(t) - \frac{1}{\tau_2} * f_{T'}(t) \qquad 3.2$$

$$\frac{dP_{T(d,d)}}{dt} = \frac{1}{\tau_2} * f_{T'}(t) \; - \frac{1}{\tau_3} * f_{T(d,d)}(t) \qquad 3.3$$

$$\frac{dP_{S_0}}{dt} = \frac{1}{\tau_3} * f_{T(d,d)}(t) \qquad 3.4$$

This yields the populations $P_{S1}(t)$, $P_{T'}(t)$, $P_{T(d,d)}(t)$, and $P_{S0}(t)$ for a specific set of τ_1, τ_2, and τ_3 values. To compute the X-ray absorption change for each energy, the sum of each species' contribution to the total signal at each energy was described as:

$$A_{total}(E,t) = \sum_{i=0}^{3} A_i(E) P_i(t) \qquad 3.5$$

Where *i* is the index of the states, *i* = 0 - 3, corresponding to S_0, $S_1(\pi, \pi^*)$, T', and T(d,d) states, $A_i(E)$ is the relative absorption of the *i*-th state at E, and $P_i(t)$ is the population of *i*-th state at *t*. The relative absorption of the ground state S_0, $A_0(E)$ and that of the T(d,d) state, $A_3(E)$ were obtained from XANES spectra at time delays with nearly 100% population of S_0 and T(d,d), respectively (before the pump laser pulse and at 20 ps pump-robe delay). The relative absorption of the $S_1(\pi, \pi^*)$ state $A_1(E)$ is assumed to be identical to $A_0(E)$ because the (π, π^*) excitation is confined on the macrocycle porphine and has little impact on the nickel center. The relative absorption of the T' state $A_2(E)$ was treated as a variable during the fits. The calculated A_{total} was then convoluted with a Gaussian instrument response function (IRF), the width of which is also treated as a variable.

3.2.7. XANES scans in the 1s → 3d transition pre-edge region.

In order to capture excitation induced changes in the Ni 3d-orbital occupation, the time evolution of the 1s → 3d quadrupole-allowed transition features was also investigated by tuning

the center of the SASE spectral bandwidth to this pre-edge region (8349 eV) and collecting energy scans. Due to relatively low signal intensities of the pre-edge features, a modified scheme to compute the XTA signal at each energy step was implemented using the slope of a linear fit of D_1 or D_2 vs I_0 rather than the average of the normalized signal for all individual shots. Monochromator scans were taken only at selected time delays of -5 ps, 1 ps, 10 ps and 50 ps. Because XAS signals in the pre-edge region contain a significant background contribution from the rising edge that varies with the time delay as the nearby $1s \rightarrow 4p_z$ transition peak shifts in energy, a second order polynomial was used to fit the background contribution of the averaged scans for each time delay. This contribution was removed to extract the individual peaks.

3.2.8. Electronic structure calculations.

To understand the overall electronic and structural evolution of the NiTMP excited states and to ascertain how changes in the electronic and nuclear structure as the molecule relaxes are reflected in the experimentally observed XTA signals, each electronic state in the proposed mechanism (Figure 3.1) was modeled separately. Initial DFT and TDDFT calculations using the BP86 functional were employed to probe the basic orbital structure of NiTMP and its excited states using the ADF package (ADF2013.01[49,50]). A double-ζ polarized (DZP) basis set was used for the description of C, N, and H atoms, and a triple-ζ polarized (TZP) basis set was used to describe the atomic orbitals of Ni. This combination of functional and basis set has previously described the orbital structure of a related Ni compound with high accuracy.[51] Subsequently, the geometries of the ground and each intermediate excited state were optimized with the BP86 functional[52-54] and the 6-31G(d) basis set[55,56] using a development version of the Gaussian software package.[54] The X-ray absorption was calculated with energy-specific TDDFT (ES-TDDFT)[57,58] using the

PBE1PBE and Ahlrichs' def2-TZVP basis set[59] with diffuse functions on the nickel atom.[60-62] For all calculations of X-ray absorption spectra, the mesityl groups on the porphyrin have been replaced with methyl groups to reduce computational cost.

3.3. Results

3.3.1. Experimental results

3.3.1.1. Ni K-edge XANES describes excited state electronic and structural dynamics.

In the Ni K-edge XANES spectra shown in Figure 3.6, the spectrum at a -5 ps pump-probe time delay (before the laser arrives) is identical to the previously obtained spectrum for the ground state S_0,[14,63] while the spectra at the 20 ps time delay and longer resemble the spectrum identified by the same study as the T(d,d) state.[14,41]

Comparing the spectra at 100 ps delay with the T(d,d) spectrum and considering the 200 ps T(d,d) state decay time constant obtained previously, we estimate the initial excited state fraction to be ~60%. XANES features for the S_0 and T(d,d) states have been assigned and share attributes characteristic of a square planar Ni(II) coordination geometry. A distinct peak at 8339 eV in the S_0 state spectrum and at 8341 eV in the T(d,d) state spectrum (Figure 3.6A, labeled E2 and E3), respectively, are assigned to the strong dipole-allowed $1s \rightarrow 4p_z$ transition.[64] Features near the "white line" absorption peak at 8351 eV are ascribed to contributions from multiple scattering resonances and transitions from Ni 1s to σ* antibonding molecular orbitals resulting from the hybridization of Ni $4p_x$ and $4p_y$ orbitals with porphyrin N 2s orbitals.

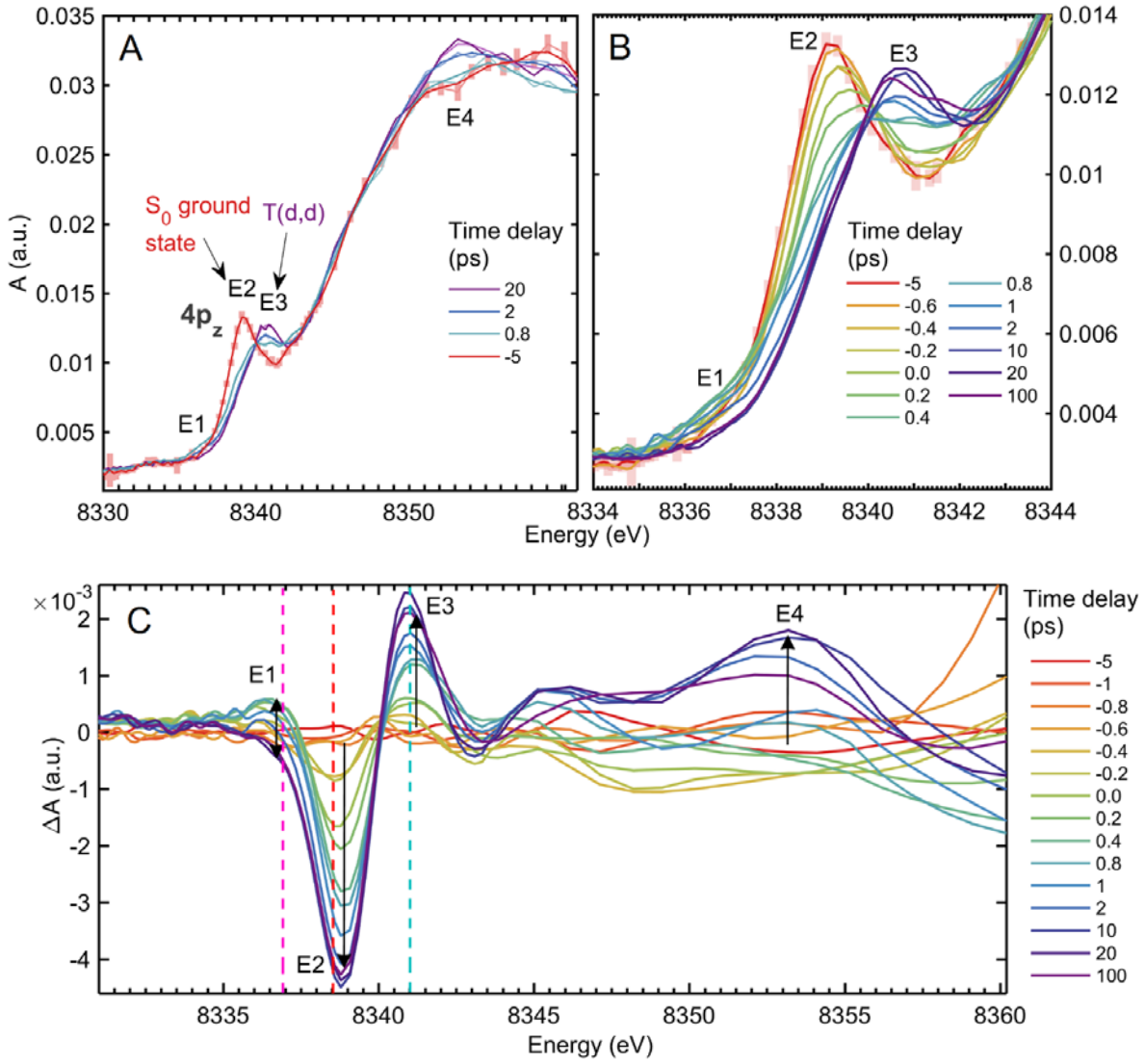

Figure 3.6: Smoothed Ni K-edge XANES spectra of NiTMP between -5 and 100 ps following 527 nm excitation. Numbered energies correspond to: E1. a transient at the low-energy end of the 1s → 4pz region, E2. the S0 1s → 4pz transition, E3. the T(d,d) 1s → 4pz transition, and E4. the white-line feature associated with shortened Ni-N bonds in the T(d,d) state. (A) Time delays characteristic of (-5 ps) S0, plotted with 95% confidence intervals to show the level of the error throughout the data set, (0.4 ps) the peak of the transient signal at 8337 eV, (2 ps) the partial disappearance of the transient at 8337 eV, the appearance of the T(d,d) 1s → 4pz peak at E2., and

the shift of the primary white line feature to E4., and (20 ps) T(d,d). (B) The evolution of the XANES from -5 ps to 100 ps within the 1s → 4pz region. (C) Difference spectra relative to S0 spectrum for delays between -5 and 100 ps, showing the dynamics of the S0 bleach (E1), the rise of the T(d,d) 1s → 4pz peak (E2), the rise and fall of the transient at 8337 eV within 2 ps (E3) and the rise of the white line feature (E4). Dotted lines correspond to energies at which delay scans were taken (Figure 3.7).

Below the rising edge in the pre-edge region from 8330 to 8336 eV are weak quadrupole-allowed 1s → vacant 3d transitions, which directly probe the 3d orbital energies and electronic occupation,[65] determined by the coordination geometry and electronic state of the Ni center. The 4p orbitals are vacant for Ni complexes, so changes in transition energies to these orbitals, as well as to all high energy bound states, are determined by perturbations to the 4p energies and changes in the energy of the core orbitals due to structural or oxidation state changes.

The progression of the electronic state population $S_0 \rightarrow S_1 \rightarrow$T(d,d) is captured by XANES spectra taken as a function of the pump-probe delay time. The peak position of the 1s → $4p_z$ transition for the S_0 state at 8339 eV (Figure 3.6A**,** label E2) clearly shifts to 8341 eV, the energy for the same transition in the T(d,d) state. Meanwhile in the less well-resolved white line region, the prominent peak feature shifts from 8359 eV to 8353 eV. While the $\sigma^*_{x,y}$ orbitals should shift to lower energy in the excited state as the Ni-N distances expand and the hybridization between the Ni $4p_{x,y}$ and Ni 2s orbitals is weakened,[66] the $4p_z$ transition blue shift has not yet been well explained due to the fact that coupling between the Ni $4p_z$ orbital and porphyrin π-orbitals is minimal.

At a glance, the spectra at time delays of -5 ps to 20 ps seem to resemble mixtures of the S_0 and T(d,d) states, but a feature around 8337 eV in the difference spectra (Figure 3.6C) is a notable exception. A transient feature at 8337 eV rises rapidly to its maximum amplitude at 400 fs to 800 fs, and decays within ~2 ps (Figures 3.6B and 3.6C). After ~2 ps, the XANES difference reflects an increasing population of T(d,d) state, whose features are fully developed by 10 ps. The ground state 1s → $4p_z$ peak depletion proceeds with an approximate time constant of ~1 ps, in contrast to the growth kinetics of the T(d,d) state 1s → $4p_z$ peak, which displays a sharp rise after ~200 fs

followed by a slower rise to the maximum peak height, suggesting the presence of an additional transient state, which we denote T' (Figure 3.1) preceding the relaxed T(d,d) state (Figure 3.6C, Figure 3.7A). The identity of the T' state is considered in Results 2.1. Other dynamics of spectral features on the ps timescale include an apparent delay between the rise of the white line peak feature at 8353 eV, which is an indication of the Ni-N bond elongation as seen in the T(d,d) state, and the rise of the $1s \rightarrow 4p_z$ transition peak associated with T(d,d). Though this region of the XANES spectrum suffers due to the drop off of the X-ray intensity at the upper limit of the SASE bandwidth, it is nonetheless clear that there is little growth of this feature until 2 ps delay time, suggesting a postponed nuclear geometry change, most likely the expansion of the Ni-N bond, relative to electronic configuration changes that lead to the blueshift of the $4p_z$ peak.

3.3.1.2. Energy dependent excited state decay kinetics.

Comparing time-delay scans at characteristic energies of 8338.5 eV (E2), 8341 eV (E3), and 8337 eV (E1), the spectral feature of the short-lived transient (Figures 3.6C & 3.7A) characterizes the decay kinetics of these electronic states along the proposed relaxation pathway (Figure 3.1).

As shown in Figure 3.7A, the bleach of the S_0 $1s \rightarrow 4p_z$ signal at E2 appears to be slower than the initial rise of the T(d,d) state $1s \rightarrow 4p_z$ at E3. The signal at E1 appears to rise almost instantaneously above that of the S_0 state then falls to the lower T(d,d) state absorption. This transient signal also interferes with the bleach of the S_0 $1s \rightarrow 4p_z$ peak at E2, causing the kinetics of the ground state bleach to appear slower than the rise of the T(d,d) $1s \rightarrow 4p_z$ peak intensity at E3. The weak transient signal again suggests that a short-lived transient species T' contributes to the overall XTA signal at those energies, manifested most noticeably at E1.

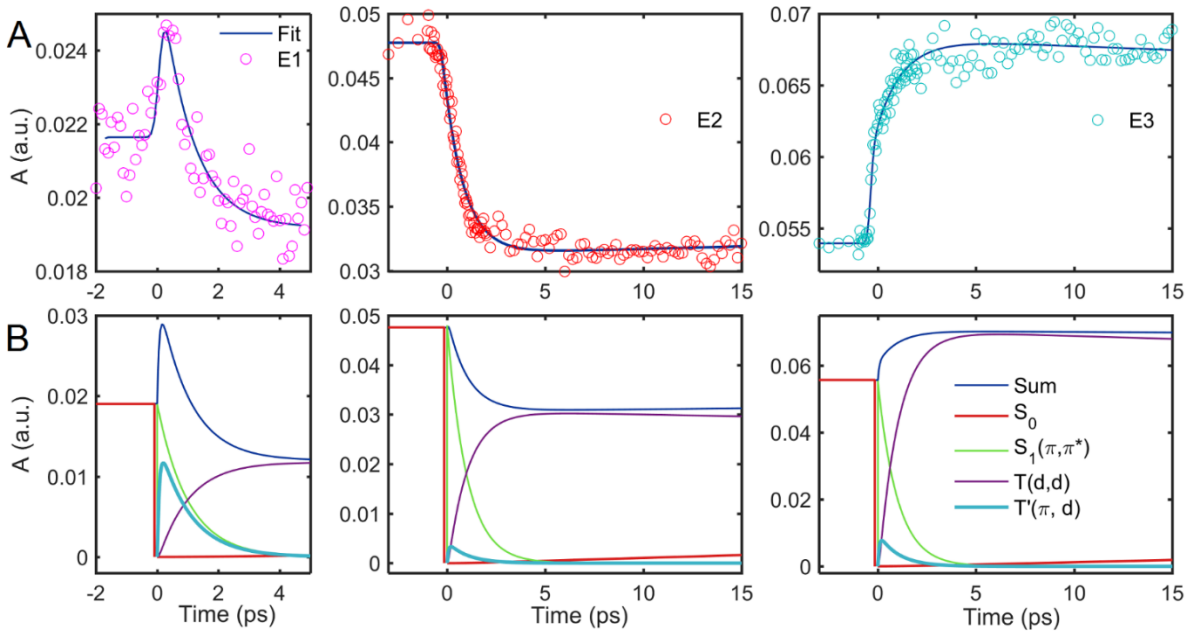

Figure 3.7: Fits of XANES kinetics. (A) Single-energy delays scans at (left to right) 8337, 8338.5, and 8341 eV with fits to kinetic model (1) (dark blue line). (B) Decomposed signal contributions from each electronic state accounted for in the fit of model (1) to the delay scans at (left to right) 8337, 8338.5, and 8341 eV determined by numerical integration of the rate expression for each species, in this case for the assignment $\tau 1 = 1.0$ ps, $\tau 2 = 0.08$ ps (<300 fs). The resulting total signal for each energy (dark blue) was fit to the delay traces.

Averaged traces at each energy were thus globally fit to the sequential kinetics model below using Equation 3.5, which incorporates the formation of T' from the initial $S_1(\pi, \pi^*)$ state and its decay into the T(d,d) state:

$$S_1(\pi,\pi^*) \xrightarrow{k_1} T' \xrightarrow{k_2} T(d,d) \xrightarrow{k_3} GS \qquad 3.6$$

where k_i (i = 1 – 3) is the rate constant and its inverse $1/k_i$ is τ_i, the time constant for the i-th step of the reaction.

As shown by the fits to the delay scans in Figure 3.7A, the totality of the data can be well-described by the scheme of Equation 3.6 with three time constants; two short lifetimes, 1.0 ± 0.05 ps and 0.08 ± 0.22 ps, and one long lifetime, 400 ± 130 ps. The ~400 ps lifetime cannot be determined accurately due to the limit of the experimental 100 ps delay time window, but it is associated with a decay of the total difference signal and can be assigned to τ_3, the decay time constant of the T(d,d) state to the ground state. This time constant has been determined previously in optical and X-ray transient absorption experiments to be ~200 ps.[14,32] The 0.08 ps lifetime is within the temporal resolution of the experiment and hence cannot be precisely determined by the current data. Hence, we interpret it as less than the width of the instrument response function (FWHM, 0.29 ± 0.17 ps). Because the absorption of T', $A_2(E)$ (Equation 3.5), is treated as a variable in the fitting, the assignment of the 1.0 ps and <0.3 ps components to τ_1 and τ_2 is interchangeable kinetically, but can be distinguished by the very different absorption of T' necessitated by the two alternatives. The scenario in which τ_1 = 1.0 ps and τ_2 <0.3 ps corresponds to a T' intermediate that absorbs much more than the ground state at 8337 eV but has little accumulation due to its rapid τ_2 decay to T(d,d). The other possibility is that T' appears with τ_1

<0.3 ps and decays with τ_2 = 1.0 ps. The alternatives have been distinguished based on the relative absorption of T' at 8337 eV, where the transient XANES signal is most easily observed, and the former is preferred because with a slow decay relative to formation, T' would accumulate significantly prior to decaying to T(d,d). As the computational results below show that T' should have a large absorption at 8337 eV, then this would require a much larger positive difference signal at this energy within the first few ps, contrary to observation. The contributions of each species in the relaxation pathway along with the sum total fitted signal are presented along with the experimental traces in Figure 3.7 for $\tau_1 > \tau_2$.

3.3.1.3. Ni 3d orbital configuration from pre-edge transitions.

Pre-edge features corresponding to quadrupole-allowed transitions from 1s to vacant 3d orbitals in the nickel center provide insight into the electronic configuration of the 3d orbitals. In synchrotron experiments, the pre-edge region of S_0 contains a single peak for the 1s → $3d_{x2-y2}$ transition arising from the electronic configuration of $(3d_{z2})^2(3d_{x2-y2})^0$ (Figure 3.8B, S_0).[14] By 50 ps after photoexcitation (Figure 3.8B, 1.), the T(d,d) excited state is fully populated and its pre-edge exhibits two peaks arising from the 1s → $3d_{x2-y2}$ and 1s → $3d_{z2}$ transitions available for the $(3d_{z2})^1(3d_{x2-y2})^1$ electronic configuration (Figure 3.8B, T(d,d)) which eventually decays to the ground state (Figure 3.8B, 4.).

Looking at the time evolution of the d-orbital transition region (Figure 3.8A), at the negative delay representing 100% ground state population, we see a single peak corresponding to the transition to the sole 3d vacancy, $3d_{x2-y2}$, consistent with previous synchrotron experiments.[14,41]

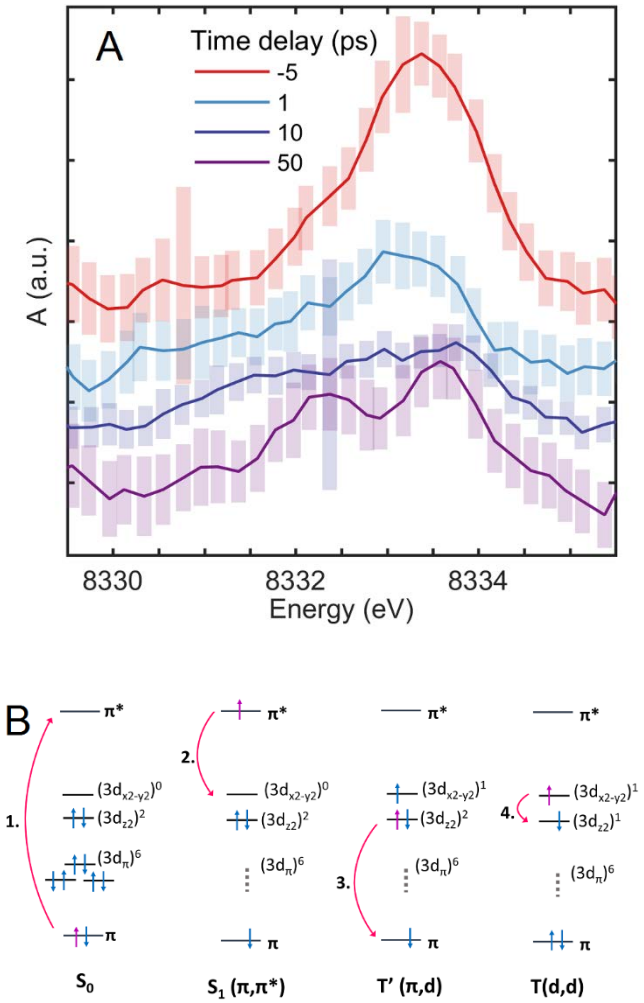

Figure 3.8: (A) XANES scans in the 1s → 3d region (Figure 2A, E0), 5 pt smoothed and with the rising XANES edge background subtracted. Offset in A(a.u.) for clarity. (B) 3d-orbital occupations of electronic states in the NiTMP relaxation pathway resulting from: (1) excitation of the porphyrin macrocycle, (2) charge transfer from the macrocycle π* orbital to the Ni metal center, (3) reverse charge transfer from Ni to the macrocycle via relaxation of a 3dz2 electron into the π hole, (4) relaxation of the $3d_{x2-y2}$ electron into the $3d_{z2}$ to recover the ground state d-orbital configuration. Note naming convention w.r.t. spin state.[51]

Following excitation, the d-orbital transitions are derived from a mixture of states which we interpret as evolving according to a series of processes represented in Figure 3.8B. At 1 ps delay time, the magnitude of this peak is diminished and slightly red shifted, while by 10 ps the pre-edge features are significantly broadened with some intensity growing in at lower energy. At 50 ps delay time, we see features associated with the T(d,d) state, where single vacancies in the $3d_{x2–y2}$ and $3d_{z2}$ lead to a split peak, although the splitting energy is 1 eV less than the 2.3 eV observed at 100 ps during synchrotron experiments. This splitting is not clearly discernable by 1 ps, but may influence the shape of the broadened features at 10 ps. The absence of a split peak by 1 ps is contradictory to the full conversion of the excited population to T(d,d) by 350 fs, as suggested by previous studies.[67] Total population of the vibrationally hot T(d,d) state is more consistent with the 10 ps spectrum where the $1s \rightarrow 3d_{x2- y2}$ and $1s \rightarrow 3d_{z2}$ transitions appear to be broadened with the $1s \rightarrow 3d_{x2- y2}$ slightly higher in energy, possibly due to the shorter Ni-N bond length. Directly detecting T' features for these weakly absorbing transitions is complicated by the fact that T' appears to be short lived, present at low accumulation, and exists simultaneously with several other electronic states. Features at 1 ps are likely ascribable to a combination of the S1 state, T', and broadened T(d,d) features.

3.3.2. Electronic structure and XANES calculation

3.3.2.1. TDDFT determination of excited state energies and geometries.

DFT and TDDFT calculations identified possible electronic states participating in the relaxation pathway. Ground and excited state geometry optimizations of these potential intermediate electronic states provided their relative energies and structural characteristics (see Methods: Computational Modeling for details of the calculation).

Using the optimized ground state geometry, the $S_1(\pi, \pi^*)$ state Frank-Condon excitation energy, which has B excitation symmetry, is computed to lie at 2.31 eV above the ground state. Any potential intermediate states in the singlet manifold should be rapidly populated according to Kasha's rule and TDDFT excited state geometry optimizations performed on the lowest lying singlet excited states of both A and B symmetry found the lowest A state at 1.31 eV and the lowest B state at 1.81 eV. The lowest A singlet state, which possesses (π, $3d_{x2-y2}$) orbital character, is chosen as a point of probable intersystem crossing and triplet states computed using the geometry optimized in this lowest A state reveal a corresponding triplet state with the same orbital character that lies close in energy at 1.25 eV. This A state provides an excellent candidate for the identity of T' because 1) it is the lowest energy state in the singlet manifold and 2) the proximity of the singlet and triplet of (π, $3d_{x2-y2}$) character in energy may enable rapid intersystem crossing. For subsequent calculations, we identify T' as a (π, d) state with the d-orbital configuration $(3d_{z2})^2(3d_{x2-y2})^1$ as suggested by the experimental XANES pre-edges.

To determine any symmetry restrictions on intersystem crossing (ISC) between these electronic states, NiTMP was modeled without the mesityl substituents to obtain a higher symmetry group. Energies calculated for corresponding states of interest are very similar to those found in the lower symmetry geometry. Group theory considerations show that ISC from the singlet to triplet manifold is allowed, as the product of the irreducible representation of $^1(\pi, 3d_{x2-y2})$ and $^3(\pi, 3d_{x2-y2})$ belong to the irreducible representation of the angular momentum operator R_z.

Relaxed geometries for the ground, $S_1(\pi, \pi^*)$, T', and T(d, d) states show significant structural differences. Both the ground state and $S_1(\pi, \pi^*)$ state geometries have a short (1.94 Å) Ni-N distance and a significant out-of-plane ruffling distortion of the porphyrin macrocycle. This

structural similarity is not surprising given the identical Ni electronic occupation in these two states. The T(d,d) state, on the other hand, exhibits 1s $\rightarrow \pi$ an expansion of the Ni-N distances by 0.1 Å, very similar to the 0.08 Å shift derived from 100 ps resolved EXAFS experiments,[14,41] and a flattening of the macrocycle conformation. A 0.8 Å Ni-N expansion is apparent in the T' state, suggesting that a *relaxed* T' geometry would have much the same structure as the T(d,d) state.

3.3.2.2. Modeling of inner shell XAS bound transitions.

Solutions to the Self Consistent Field (SCF) equations that converge to a higher energy than ground state solutions have long been recognized as useful approximations to excited state wave functions.[68-70] These solutions allow excited states to be treated in a single determinant framework whose response can be modeled with TDDFT. In order to obtain these higher-energy SCF solutions, a set of natural transition orbitals (NTOs)[71] for the state of interest was first generated at the excited state geometry. The initial guess for the SCF density of this higher-energy solution was then formed by a HOMO-LUMO swap of the dominant NTOs. A second-order optimization scheme was then used to converge to the state of interest.[72] The XANES spectra of these intermediate states were then calculated with ES-TDDFT at the same level of theory as the ground state (discussed in Computational Modeling).

Due to the neglect of scalar and spin-orbit relativistic effects in this simulation, the calculated transitions are much lower in energy than the experimental results. However, it has been shown that these operators have little effect on relative transition energies[73] and uniform shifts are routinely applied to calculated XANES spectra to better compare transition energies with experimental data.[73-75] A uniform shift of 172 eV is applied to all calculated spectra and all

transitions are convoluted with Gaussian functions to match experimental lineshapes; 2.2 and 1.8 eV FWHM for the $4p_z$ and 3d transitions respectively.

The dipole allowed 1s → 4p transitions are the dominant transitions in all calculated XAS (Table 3.1, Figure 3.9A). The electronic environment around the Ni atom has changed minimally between the S_0 and $S_1(\pi, \pi^*)$ states, so little change is seen in the 1s → $4p_z$ transition. However, a red and a blue shift is observed for the T' and T(d,d) states respectively. These trends reproduce those of the experimental data where the T(d,d) 1s → $4p_z$ transition is clearly blue shifted compared to the S_0 and a short-lived rise and fall is evident red of the S_0 peak.

It's worth noting, however, that the calculated transitions are pure populations of their respective electronic states, which do not exist in the relaxation of the excited NiTMP and the experimental data reflects of a mixture of states. For this system, the modeled 1s → 3d transitions reflect the expected 3d-orbital occupation for the ground and T(d,d) states. Modeled transitions to $3d_{z2}$ and $3d_{x2-y2}$ roughly coincide with the two peaks apparent in the experimental XANES at 50 ps delay (Figure 3.9B) and are very similar to those observed in the pre-edge region at 100 ps during our previous synchrotron experiments.[14,41] The experimental 1s → $3d_{x2-y2}$ peak at 1 ps is slightly red shifted compared to the ground state and this same behavior is seen for the modeled transition for the T' state. This red shift is notable as it contrasts with the blue shift observed for the same transition at 50 ps and for the modeled T(d,d) state. A weakly dipole allowed 1s → π transition is apparent in the calculated spectra of the $S_1(\pi, \pi^*)$ and T' states, although these are not plotted because their contribution is removed during background subtraction of the experimental data.

Table 3.1: Orbital energies for the electronic ground state and changes in those energies in various excited states (blue -occupied and red - unoccupied).

	Inputs for excited-state XAS modeling							
Wave function	**S_0**	**$S_1(\pi, \pi^*)$**	**T'**	**T(d,d)**	**S_0**	**S_0**	**T(d,d)**	**T(d,d)**
Geometry	**S_0**	**$S_1(\pi,\pi^*)$**	**T'**	**T(d,d)**	**T'**	**T(d,d)**	**S0**	**S1**
	Calculated Ni orbital energies							
	eV	---------- ΔeV ----------						
1s α	8167.47	-0.05	2.02	-1.17	0.37	-0.34	-0.67	-0.61
1s β	8167.47	-0.05	2.03	-1.17	0.37	-0.34	-0.67	-0.61
$4p_z$ α	1.39	-0.07	0.18	-0.23	0.06	-0.03	-0.15	-0.16
$4p_z$ β	1.39	-0.06	0.05	-0.44	0.06	-0.03	-0.34	-0.34

Table 3.2: Ni 1s and 3d orbital energies for the electronic ground state and changes in those energies in various excited states (blue -occupied and red - unoccupied)

Geometry	***Ground state***	***$S_1(\pi,\pi^*)$***	***T'***	***T(d,d)***	***T'***	***T(d,d)***	***Ground State***	**$S_1(\pi,\pi^*)$**
Wave function	***Ground state***	***$S_1(\pi,\pi^*)$***	***T'***	***T(d,d)***	***Ground state***	***Ground state***	***T(d,d)***	**T(d,d)**
Units	***eV***	***ΔeV***						
1s α	-8167.47	-0.05	2.02	-1.17	-0.37	-0.34	-0.67	-0.61
1s β	-8167.47	-0.05	2.03	-1.17	-0.37	-0.34	-0.67	-0.61
$3d_{z^2}$ α	-6.61	-0.04	0.69	3.96	-0.28	-0.25	4.29	4.23
$3d_{z^2}$ β	-6.61	-0.04	1.66	-2.99	-0.28	-0.25	-2.71	-2.68
$3d_{x^2-y^2}$ α	-0.50	-0.03	-4.00	-5.15	-0.93	-0.95	-4.58	-4.04
$3d_{x^2-y^2}$ β	-0.50	-0.03	3.12	-0.18	-0.93	-0.95	0.91	0.86

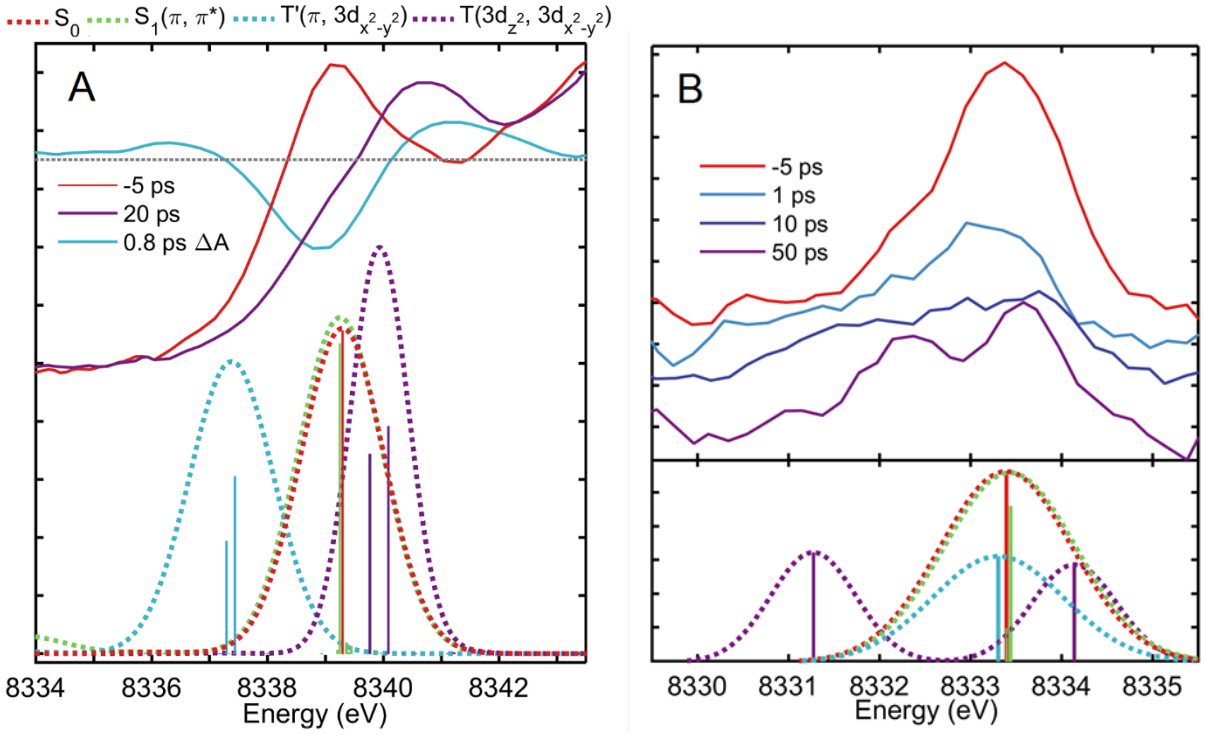

Figure 3.9: Gaussian-*broadened* calculated XAS transitions of relevant excited electronic states compared to experimental spectra in (A) the rising edge regions where 1s → $4p_z$ transitions dominate and (B) the pre-edge region.

Furthermore, these are relatively short-lived states, the contribution to the total signal is quite small, and this region of the spectrum is very noisy due to low XAS signal, so well-defined peaks for these weak dipole allowed transitions are not observed experimentally.

3.4. Discussion

This study, which is among early examples of XTA measurements at LCLS, allows us to establish a kinetic scheme describing the decay of photo-excited NiTMP and to distinguish the short-lived Ni(I) state T' as an intermediate preceding the formation of the previously characterized T(d,d) state. Inner-shell transitions characterized by the combined experimental and computational results are analyzed to derive properties not directly measureable using other ultrafast methods. Here, we discuss the evidence for the charge transfer nature of the short-lived T' state, discuss the interpretation of the modeled XAS transitions towards discerning the impact of electronic occupation on Ni orbital energies, reflect on the role of structure in determining excited state properties, and present our views on the implications of our findings for potential applications.

3.4.1. Evidence for a transient Ni(I) center due to intramolecular electron transfer.

In combination with calculated XAS transitions relating transient XANES features to corresponding electronic states, global analysis of the XTA signal as a function of the X-ray photon energy and delay time allowed us to overcome challenges in the assignment of T' to a CT state: 1) the weak T' state signal compared to those of the S_0 and T(d,d) states through the rising-edge; 2) the ambiguity of previous ultrafast optical absorption measurements with regards to changes in the Ni orbital occupation; and 3) the uncertainty of the correlation between the 3d electronic configuration and the energy of the prominent $1s \rightarrow 4p_z$ transition.

Global fitting of kinetic traces at three characteristic X-ray energies results in three time constants for the three-step sequential model (Equation 3.6). However, the assignment of these time constants to specific processes requires an idea of the relative absorption properties of each state involved. This was determined with the DFT assignment of the difference XANES spectral feature at E1 to the 1s → $4p_z$ transition peak of the T' state. This assignment would have been otherwise challenging due to evolving background signals near the rising edge and the lack of available XANES data for Ni(I) square planar systems. The decomposition of the total signal (Figure 3.7B) shows that the apparently faster rise at E2 compared to the decay at E1 arises from a small positive contribution to the signal from T' at both energies that rises and decays quickly. The kinetics of the T' state absorption (Figure 3.7B, cyan curves) initially appear to be the result of an ultrafast (< 300 fs) generation time constant τ_1 and a relatively slow (~1 ps) decay time constant τ_2 for the T' species. However, taken by itself the integrated rate law for the T' population derived from the sequential kinetic model (Equation 3.6) cannot distinguish between this assignment and τ_1 = 1 ps, and τ_2 < 0.3 ps. This second case results in low T' population accumulation. Given the expected large absorption of T' at 8337 eV due to its redshifted 1s → $4p_z$ transition, the modest increase in signal at this energy supports the latter assignment.

Because the T' state decays significantly faster than it forms, so-called "inverted kinetics" govern the T' population. The 1 ps decay of the T' population reflects the 1 ps decay of the $S_1(\pi, \pi^*)$ population from which T' is being constantly generated, while the <0.3 ps decay of the T' state limits T' accumulation even when the population of $S_1(\pi, \pi^*)$ is large. This manifests as the population rise time and the rise of the T(d,d) state closely follows the rate of formation of this

intermediate state, as this is essentially rate limiting. These population kinetics follow our observation that the transient T' state is only detectable for 1-2 ps.

Relaxation through a charge transfer (CT) state that produces a transient Ni(I) intermediate has been previously hypothesized based on double-excitation optical methods that observed the relaxation of an excited π electron through d-orbital vacancies in the long-lived T(d,d) state in NiTPP.[33] Such a CT state has also been implicated as the route of excited porphyrin deactivation in Ni tetraphenylporphyrin (NiTPP), Ni octaethylporphyrin (NiOEP), heme[76], and several other open-shell metalloporphyrins[77] by pump-probe photoelectron spectroscopy measurements in the gas phase, which report fast time constants for the evolution of the NiOEP excited state absorption very similar to this work (100 fs and 1.2 ps).

A short lived CT state, T', is compatible with the population of the T(d,d) state on the picosecond time scale as observed by previous studies,[67,78] although these did not implicate a charge transfer state and depicted the $S_1(\pi, \pi^*)$ relaxation process as the direct transfer of the excitation to the metal center, resulting in a hot T(d,d) state. Vibrational relaxation of the hot T(d,d) state was observed within 10-20ps.

During this period, vibrational relaxation processes likely occur and these results do not preclude the involvement of an unrelaxed T(d,d) state in the S1 decay. However, a purely vibrational model that does not assign T' as a CT state is not as well supported by the current analysis of the $4p_z$ region, where XANES differences before T(d,d) is fully populated are ascribed to the rearrangement of the Ni electronic structure. Ni orbital energies calculated for a T(d,d) electronic configuration but an S0 or S1 geometry, approximating an unrelaxed T(d,d) state, show

that such a state cannot account for the transient signal at 8337 eV due to an overall blue shift in the 1s → 4pz transition (Table 3.1). One other (d,d) state, ($3d_{xz}/3d_{yz}$, $3d_{x2-y2}$) is energetically allowed and may have a slightly redshifted 1s → 4pz peak, at least at the S_0 geometry, due to the localization of electron density on Ni as charge shifts from orbitals highly hybridized with the porphyrin π orbitals to $3d_{x2-y2}$ but this is likely small compared to a LMCT state. Furthermore, the relaxation of this state to T(d,d) would require an additional d → d relaxation process which is unlikely to proceed with the rapidity we observe for the T' decay.

Nuclear movement during vibrational relaxation affects the 3d orbital energies, especially those involved in coordination to the porphyrin ring, which is reflected in the dynamics of the 1s → 3d transition region as general broadening of the 3d transitions in T(d,d). An increased linewidth for NiTMP 1s → 3d transitions due to conformational heterogeneity was previously observed for the NiTMP ground state.2 This may provide an explanation of the apparent broadening of 3d transitions at 10 ps when T(d,d) is fully populated although a full description of the relaxation processes in terms of nuclear movement requires additional measurement with more direct structurally sensitive techniques.

3.4.2. XAS transitions reflect photo-induced electronic structural changes in the metal center.

Because it directly probes transient metal orbital energies and occupancy, XTA on the fs time scale can determine the dynamics of photoinduced metal electronic configuration and orbital energy changes well before thermalization of the excited states. While optical transient absorption measurements can clearly identify the kinetics of $S_1(\pi,\pi^*)$ state decay, they are not able to directly detect optically dark electronic states arising from changes in *metal centered* electronic occupation or metal orbital energy changes in subsequent excited states. This study has directly obtained

energies of the transitions 1s → 3d and 1s → $4p_z$ in Ni for different electronic states, from which these properties have been obtained for short-lived transient states.

Changes in the observed Ni K-edge transition features, such as the red shift and subsequent blue shift of the 1s → $4p_z$ transition energy, agreed with the calculated inner shell transitions (Table 3.1) and their energies are interpreted in terms of the evolving electronic configuration. With the assignment of T' to Ni(I), T' state formation can be understood as the intramolecular charge transfer from the π^* orbital to the $3d_{x2-y2}$ orbital. Computational results indicate a rise of the 1s energy by ~2 eV for the T' electronic configuration, where charge transfer results in greater nuclear shielding and therefore a lower electron binding energy. The rise of the 1s orbital energy in turn reduces the 1s → $4p_z$ transition energy in the T' state. This is identical to the core-level shift seen in X-ray photoelectron spectroscopy (XPS)[79] and the effect of oxidation on K-edge spectra has also been observed in previous XAS experiments.[80,81]

This computed red shift is seen experimentally as the rise and fall of intensity around E1 in <2 ps. Only about 0.2 eV of the ~2 eV shift in the 1s → $4p_z$ transition energy change from the ground state to the T' state transition is due to the shift of the $4p_z$ orbital energy. Similarly, the blue shift in the 1s→$4p_z$ transition energy of the T(d,d) state can be attributed to a change in the repulsive potential felt by the core electrons as the $3d_{x2-y2}$ orbital is far more hybridized with the ligand orbitals than the $3d_{z2}$ orbital (Figure 3.13). Relative to the ground state, which has a doubly occupied $3d_{z2}$ and an unoccupied $3d_{x2-y2}$ orbital, the T(d,d) state has less electron density around the Ni atom, lowering the 1s orbital energy and blue-shifting the 1s → $4p_z$ transition by 1.5 eV.

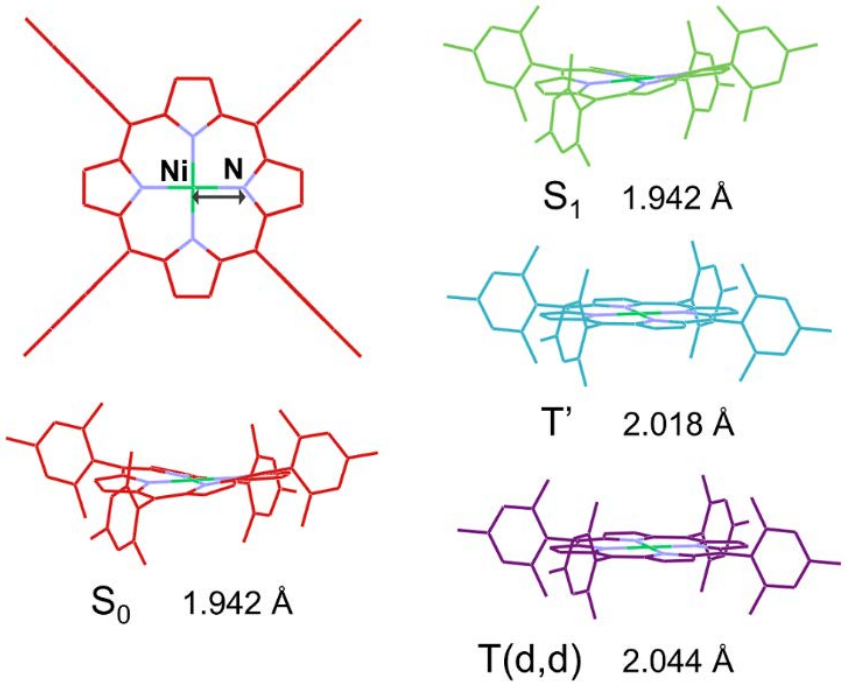

Figure 3.10: Relaxed geometries of each electronic state in the NiTMP decay pathway as calculated by TDDFT. Occupation of the Ni $3d_{z2}$ orbital drives expansion of the Ni N bond length and subsequent flattening of the macrocycle.

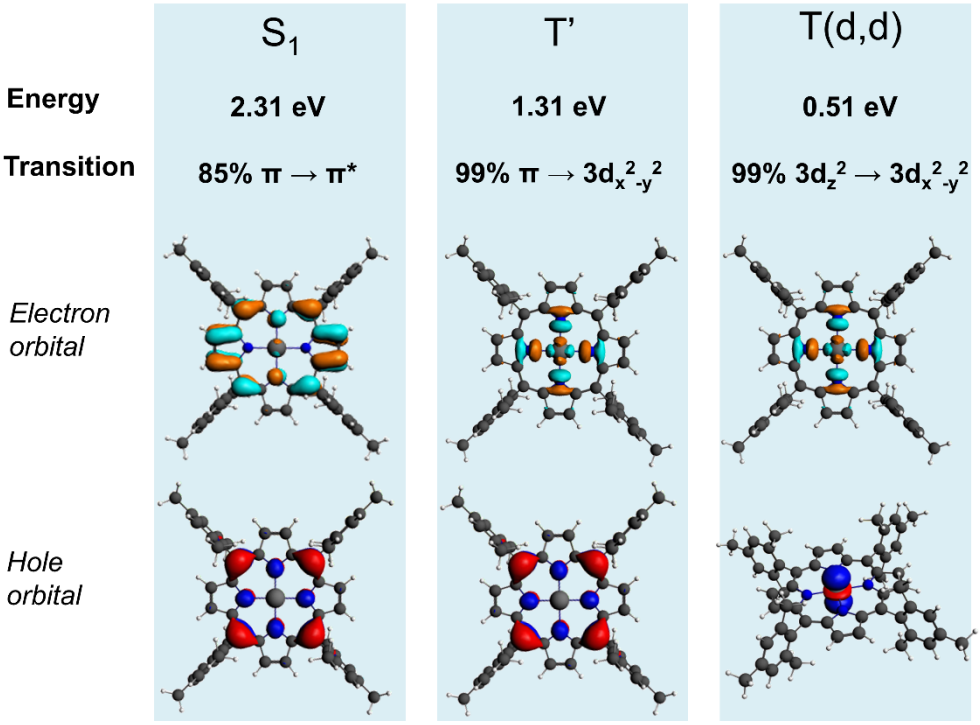

Figure 3.11: Molecular orbitals involved in each excited electronic state transition. Many features of the excited state XANES can be explained based on the movement of electron density on or off of the metal center.

As evidenced by the computed changes in the Ni 1s energy experimental 1s → 3d transition energies cannot be solely relied upon to determine changes in d-orbital splitting. Though the 1s → $3d_{x2-y2}$ transitions, for example, are within half an eV of each other according to the experimental spectrum, we can expect the $3d_{x2-y2}$ orbital energy to change much more significantly to remain consistent with the shifts in the Ni 1s energy. Calculated transition energies are very similar to those experimentally observed with the possible exception of the T(d,d) state, though even here the trend in the movement of the transitions with respect to the ground state is preserved.

3.4.3. Macrocycle structural response to NiTMP electronic evolution.

The identification by TDDFT of T' as the lowest energy singlet as well as a state with a triplet state lying close in energy lends credence to the identification of T' as a (π, d) state. The optimized geometries of the involved electronic states (Figure 3.10) provide insight into the behavior of the NiTMP structure in response to electronic changes and the subsequent energetic rearrangement of Ni orbitals.

Macrocycle expansion and flattening in the T(d,d) state is explained based on the net movement of electron density from $3d_{z2}$ to $3d_{x2-y2}$, which sits in the porphyrin plane and aligns well with the Ni-N bonds. This bond expansion is a repulsive response to additional electron density localized between the Ni and N atoms. Because the macrocycle need no longer accommodate the unusually short Ni-N bond length, the constrained ruffled geometry relaxes to a more energetically favorable flattened conformation that allows greater delocalization of π electrons. Interestingly, the majority of the Ni-N bond length expansion has already occurred in the relaxed geometry of the T' state, which has a flattened porphyrin conformation and a Ni-N

bond length expansion of 0.08 Å, suggesting that the occupation of $3d_{x2-y2}$ is the main driver of porphyrin expansion.

Comparisons to 1s, $4p_z$, and 3d orbital energies calculated for the T' and T(d,d) optimized geometries but using the ground state wave function to describe the electronic state are used to separate electronic vs. structural effects on the excited-state XANES. In spite of the significant difference in structure between the ground state and the T' and T(d,d) states, the difference in the $4p_z$ orbital energies is very modest and the shift in the 1s energy is only about -0.3 eV for both geometries (Table 3.1). We can therefore conclude that the $1s \rightarrow 4p_z$ transition energy is largely determined by the electronic state of Ni, which is in line with the fact that the 1s shift dominates the observed transition shifts and that $4p_z$ has less interaction with ligand orbitals than other valence Ni orbitals. The relative insensitivity of the $1s \rightarrow 4p_z$ energy to solely structural changes in the porphyrin conformation and Ni-N bond length also discounts the explanation of the short-lived transient signal as pure vibrational broadening of the T(d,d) state $1s \rightarrow 4p_z$ feature.

Based on our observation of the Ni(I) state's lifetime and the corresponding structural evolution, we can speculate on the participation of the ring structure and conformation on the stabilization of this species. Porphyrins with large out-of-plane ground state distortions generally have dramatically different photophysical properties compared to analogous planar porphyrins, exhibiting low fluorescence yield and shorter excited state lifetimes owing to an increase in accessible nonradiative decay pathways through a high degree of conformational flexibility.[35,82] A TDDFT survey of Ni porphine, NiTPP and NiOEP singlet and triplet states noted that the lowest energy singlet states in all cases are CT states of $^1(\pi, 3d_{x2-y2})$ character, the energy of which increases for NiTPP which has a higher degree of macrocycle out-of-plane distortion, in this case

ruffling.[51] Meanwhile, the lowest energy triplet state, the T(d,d) state, is destabilized to an even greater degree as ruffling increases, reducing the energy gap between these states and (π, $3d_{x2-y2}$) states. This suggests that not only are more routes to radiationless deactivation available for distorted porphyrins, but the relevant electronic states along the proposed route of deactivation are closer together in energy and the decay process is faster according to the energy gap law.

In the ground state, Ni porphyrins have a low barrier to interconversion between various distorted conformers of the macrocycle,[83,84] e.g., ruffled, domed, etc., as evidenced by the relative broadness of the $1s \rightarrow 3d_{x2-y2}$ transition peak.[41] The lowest in energy of these conformers is a ruffled geometry according to our own geometry optimization. Geometry optimizations of the T' state indicate the Ni-N bond length should expand, and therefore flatten the macrocycle. Based on the delay in the rise of the white line feature at 8353 eV, closely related to the Ni-N bond length, with respect to the features associated with the $1s \rightarrow 4p_z$, this expansion is delayed compared to the change in the electronic state. Because the T' state appears to initially retain a ruffled geometry while the molecular structure has yet to respond to the electronic change, its conversion to the T(d,d) may be accelerated by the structural effect mention above, causing relaxation to T(d,d) to occur before the molecule has time to flatten.

Out-of-plane distortions are structural factors that influence electronic state energies mainly through the destabilization of the π and $3d_{x2-y2}$ orbitals, an effect that when taken to a greater extreme in substituted Ni phthalocyanines begins to lead to *longer* CT state lifetimes. While the CT state reported here and in previous studies of Ni porphyrins is very short-lived, on the order of <2 ps, octamethyl and octabutoxy substituted Ni phthalocyanines have been described as having long-lived LMCT states with lifetimes in the hundreds of picoseconds.[82,85] Here, ring substitution

leads to the decrease of the relative CT state energy compared to the equivalent ($3d_{x2-y2}$, $3d_{z2}$) state to the point where the CT state is the lowest energy triplet state, extending the lifetime of the Ni(I) to the point of potential catalytic utility.

3.5. Summary

Ultrafast XANES at the Ni K-edge was successfully measured for optically excited Ni(II)TMP on a previously unachievable sub-picosecond timescale, providing insight into its ultrafast electronic and structural relaxation processes. Importantly, a transient Ni(I) (π, d) electronic state (T') is implicated as an intermediate through the interpretation of a short-lived excited state absorption. The assignment of this absorption is confirmed by agreement with calculated XAS transitions for the postulated (π, d) electronic states at this energy.

The observed and computed inner shell-to-valence orbital transition energies demonstrate and quantify the influence of electronic configuration on specific metal orbital energies. The strong influence of the valence orbital occupation on the inner shell orbital energies indicates that one should not use the transition energy from 1s alone to draw conclusions about the d-orbital energies of different states. A transient electronic configuration could influence d-orbital energies up to a few eV and any potential photocatalytic application should account for this to ensure that energy levels are well matched and that the photoexcitation can be used optimally in driving desirable processes.

NiTMP structural dynamics have been deduced from DFT optimized geometries and structurally sensitive features in the Ni K-edge XANES. Structural changes such as macrocycle expansion and flattening appear to have little impact on the energies of Ni axial orbitals observed

in this study compared to the electronic changes that occur as the molecule relaxes. However, the influence of the porphyrin macrocycle conformation on relaxation kinetics may be significant enough to affect the kinetics that govern the limited population accumulation of Ni(I). The short lifetime of the T’ state and the delay of the nuclear rearrangement to a longer Ni-N bond length and flattened macrocycle with respect to its formation suggests the still-ruffled macrocycle expedites T’ decay.

Chapter 4. Ultrafast Myoglobin Active Site Dynamics Following Ligand Photolysis

4.1. Introduction

Iron porphyrins are extremely abundant functional groups in nature. The hemoproteins are a large and diverse family that spans a vast array of enzymatic activities, including electron transfer, catalytic oxidation or reduction of metabolites, neutralization of damaging reactive species, and famously the binding of diatomics such as dioxygen, carbon monoxide, and nitric oxide for transportation and sensing.[3,15-19]

The globins are a subset of diatomic-binding hemoproteins, the most famous and widely studied examples of which are the oxygen transporters Hemoglobin (Hb) and Myoglobin (Mb). [86-89] However, globins have been increasingly demonstrated to have a complex set of physiological functions that extend beyond O_2 transport,[90,91] including their participation in a number of signaling pathways as sensors of endogenous CO and NO. In binding these signaling molecules, as in the binding of O_2 by hemoglobin,[92] the movement of Fe from a domed square pyramidal structure into the porphyrin plane triggers a long range allosteric conformational change.[93] The mediation of ligand binding by structural and electronic factors imposed on the heme by the protein matrix plays a large role in the regulation of enzymatic activity, as demonstrated by the variation of diatomic binding affinities between globins and as a result of changes in the allosteric state exemplified by the R to T transition in hemoglobin.

Because the dissociation and subsequent recombination of diatomics such as CO and NO can be synchronized through an optical excitation of the porphyrin, diatomic ligand binding in hemoproteins is amenable to scrutiny by dynamic structural and electronic spectroscopies.[3,94-100] For CO association and dissociation from Mb, the dynamics of both structural and electronic

changes at the heme promise to reveal the complex relationship between function and spatial and temporal physical properties.

In Carbmonoxymyoglobin (MbCO), the low spin Fe(II) is bound in a pseudo octahedral configuration by the porphyrin nitrogens (N_p), the nitrogen of an axial histidine (N_{His}, His 93), and CO, a strong field ligand.[101,102] On excitation of the porphyrin Soret or Q bands, photolysis occurs within 50 fs, although there is an ongoing debate about the mechanism of CO photolysis and the subsequent relaxation of heme. With the loss of CO, the now low spin iron adopts a square pyramidal structure with the axial histidine and comes ~0.3 Å out of the porphyrin plane, perturbing the position of His93 and the alpha helix in which it sits (Figure 4.1).[17,95,103,104] Protein control of this movement is critical both because it is the first step of the mechanism of cooperativity in hemoglobin O_2 binding and because it may lead to a conformational rearrangement of the heme pocket that allows CO to escape and avoid geminate recombination.[105] It's therefore of great interest to link dynamic structural and electronic changes at the heme during ligand dissociation to more large scale conformational changes, especially on the timescale of ligand departure and heme doming, which is expected to take place within picoseconds. To this end we have recently obtained XAS dynamics on the sub-ps time scale at XPP, LCLS with the simultaneous detection of the protein scattering signal. The scattering data is currently being analyzed by collaborators and is not discussed.

4.1.1. Synchrotron X-ray Transient Absorption of carbmonoxymyoglobin photolysis

Time-resolved XAS measurements of CO dissociation from Mb have evolved for three decades with the capabilities of synchrotron and laser technology.

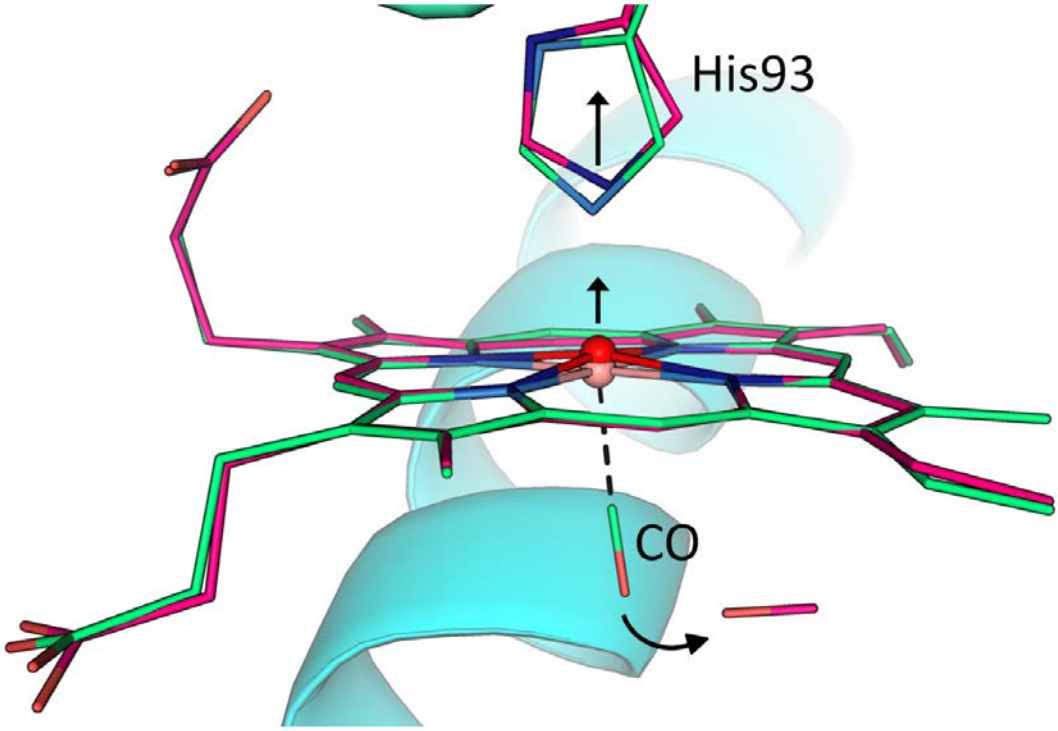

Figure 4.1: Myoglobin active site structural changes following CO photolysis. Upon photoexcitation, ground state MbCO (green) loses its bond to CO and adopts a square pyramidal structure with His93 (pink), resulting in the “doming” of the porphyrin where the Fe (red) comes out of the plane of the macrocycle. Structures are from photolysed MbCO trapped at low temperature [99] and ground state [96] MbCO, where their crystal structures are aligned by their respective porphyrin carbons.

Pioneering work by Mills[106] observed changes in the Fe K-edge position following the photolysis of CO with a time resolution of 300 μs. This edge shift is due in part to the loss of the electron withdrawing effect of the back bonding CO ligand in addition to other electronic and scattering effects. Utilizing advancements in the laser repetition rate to achieve much higher signal to noise, later work by Wang[107] improved this time resolution to 100 μs. Improvements in overall signal quality made analysis of the weak Fe 1s to 3d transitions possible, enabling the observation of the low spin to high spin transition of the d electrons on photolysis.

More recently, diatomic Mb recombination dynamics have been assessed with ps- resolved XTA (Figure 4.2). With an energy range covering both the XANES and EXAFS portions of the iron K-edge, our group was able to investigate both electronic changes in the Mb metal center, such as the rearrangement of the d-level energies and occupancy, and structural changes in the iron heme[102]. Within the 100 ps limit determined by the width of the X-ray pulse, a large change in the Fe edge position takes place following photodissociation.

The edge shift is accompanied by changes in the XANES energy region associated with the quadrupole allowed metal 1s to 3d transitions of the Fe pre edge. Two well separated d transitions can be attributed to orbital vacancies. These are orbitals with a lot of $3d_{x2-y2}$ and $3d_{z2}$ character for the lower energy transition, and with 3d → CO back bonding antibonding character for the higher energy transition (Figure 4.3). 100 ps following photolysis, these distinct peaks disappear and are replaced by a broader, weaker, red shifted feature. This can be rationalized based on the transition from a low spin d^6 pseudo octahedral coordination environment to one that is high spin and square pyramidal with the loss of a strong field axial ligand.

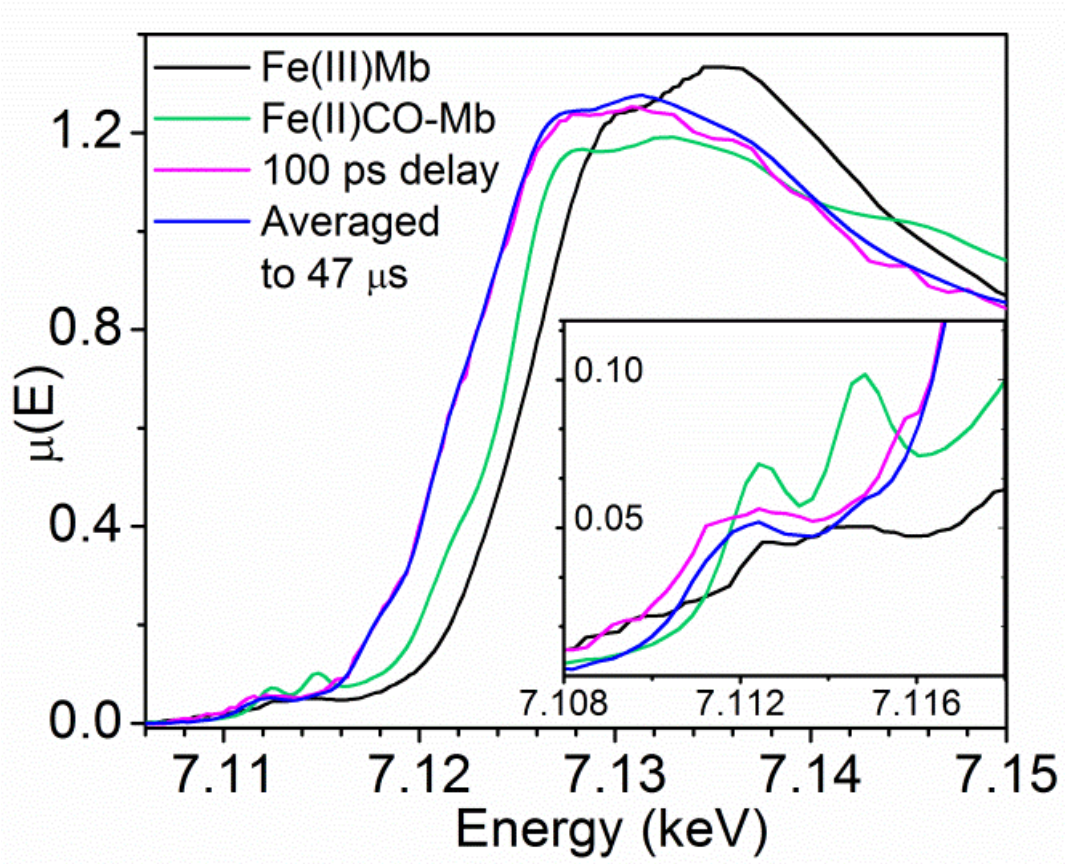

Figure 4.2: Fe K-edge XANES measured after CO photodissociation with 100 ps time resolution. Ground state XANES and the expanded pre-edge region (inset) for metmyoglobin and MbCO are shown in addition to photoexcited MbCO at various delay times. CO has a long recombination rate and all pulses to 47μs can be averaged to represent the CO dissociated state.

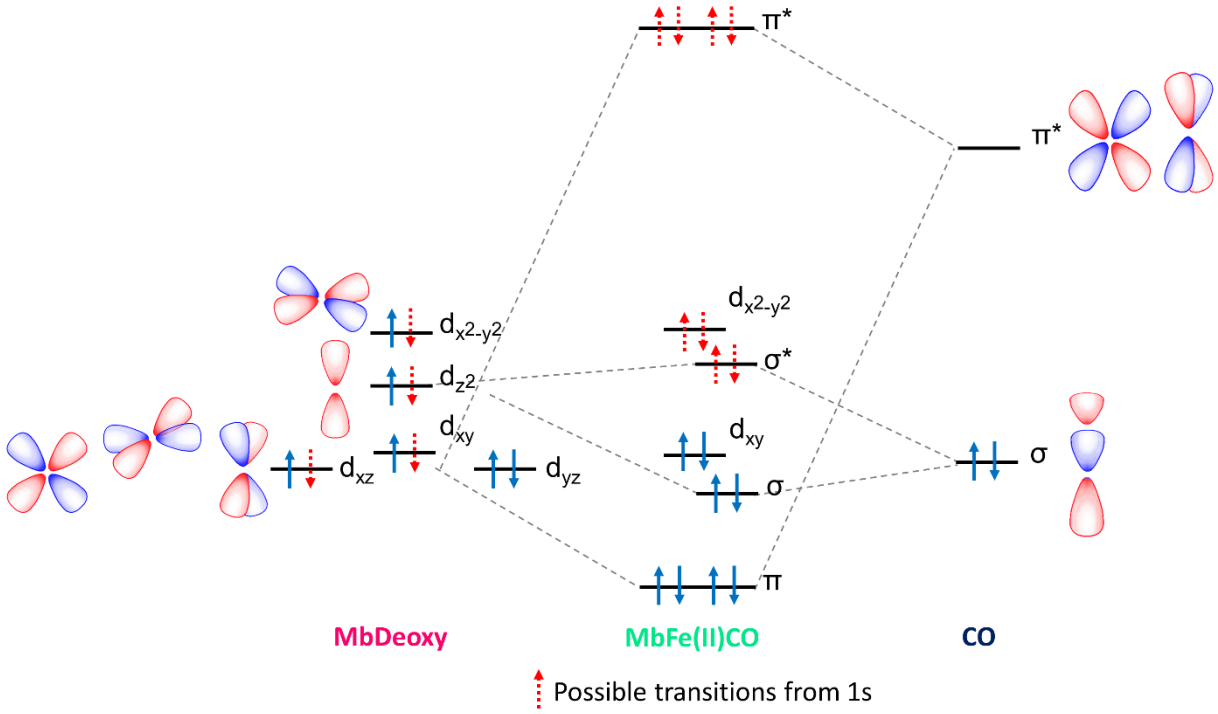

Figure 4.3: Ligand field picture of CO bonding to deoxymyoglobin, including relevant Fe atomic and CO molecular orbitals. Red dashed arrows show possible transitions from 1s and indicate the origin of the pre-edge peaks for MbDeoxy and MbCO.

With the reduction of crystal field splitting and the transition to high-spin d^6, red shifted transitions to all 3d-chararacter orbitals become available at diminished intensity, as they are half filled, and the back bonding antibonding orbital ceases to exist. However, changes in the first 100 ps persist for 10s of μs, indicating that the process of heme relaxation is complete within the first 100 ps. Optical and vibrational studies also find little change in the heme absorption after 20 ps save for recombination of the CO,[95,108] but on the sub-ps to ps timescale several heme relaxation processes occur.

4.1.2. Ultrafast processes in heme relaxation and opportunities at XFELS

Before totally thermal equilibration by 20 ps,[109] the heme must necessarily undergo the transition from low spin to high spin d^6, the elongation of Fe-N_p and Fe-N_{His} bonds, and the movement of iron out of the heme plane. While heme cooling has been observed by time-resolved Raman techniques on the timescales of a few to 10s of ps[108,110] and transient absorption spectroscopy shows the development of broad excited state absorption features red of the bleached Soret that decay with time constants of ~3 ps and ~300 fs, an active discussion exists in the literature as to whether these features are attributable to a decay through a series of intermediate electronic species[101,111-113] or through an exclusively vibrational relaxation pathway.[109,114] More recent models involving transient electronic states implicate the 300 fs and 3 ps components to the decay of a rapidly formed (<50 fs) MLCT state to a mixture of (d,d) states, followed by relaxation to the high spin deoxy heme.[101] Vibrational models, on the other hand suggest the transition to the high spin deoxy ground electronic state is very rapid, as the Fe-His mode associated with the 5-coordinate ground state appears in <100 fs,[109]

Because Fe K-edge XTA is sensitive both to the heme electronic structure and the local structural geometry during heme relaxation, measurements of the XANES should distinguish between these mechanisms, but only if very fast timescales are resolvable. In this regard, XTA at LCLS provides a rare opportunity to investigate these relaxation processes with a technique with both high temporal and structural resolution.

4.1.3. Optical Polarization Selected XTA

Even with tools of modern electronic structure and multiple scattering theory, dynamic features in the XANES can be difficult to assign, especially in the absence of a full XANES spectrum. Polarized XAFS has long been used to identify features in ordered, steady state samples by determining the dependence of the XAS dichroism on the angle between the incident X-ray and the sample plane from which order can be defined. This takes advantage of the horizontal polarization of synchrotron (and XFEL) radiation and the selection rules that govern transitions into bond states and photoelectron propagation direction.

The fs time resolution of LCLS allows us to probe excited molecules at times much shorter than their rotational diffusion time, and in this study we expand the capabilities of ultrafast XTA by implementing Optical Polarization Selected XTA (OPS-XTA). The core concept of OPS-XTA is that creating a partially oriented excited population in solution with an optical pulse and varying the orientation direction of this population with respect to the X-ray pulse polarization will lead to XANES dichroism as different bound state orbitals and absorber-backscatterer directions are probed (Figure 4.4). The orientation of the excited population depends on alignment of the polarization direction of the *pump* pulse electric field vector $\hat{e}$ with the molecular electronic transition dipole moment μ of randomly oriented molecules in solution. The probability of

excitation via a dipole mediated transition for a single molecule is proportional to the relative angle of these vectors Θ (Figure 4.4A):

$$\boldsymbol{p(\theta) \propto \langle \hat{e} \cdot \mu \rangle \propto cos^2 \theta} \qquad 4.1$$

The XANES signal for the parallel orientation of the optical and X-ray polarization ($s_{\parallel}$) therefore probes scattering and electronic transitions of the correct symmetry parallel to the transition dipole moment μ while the signal for the perpendicular orientation ($s_{\perp}$) probes in either orthogonal direction (Figure 4.4B). The dichroism between $s_{\parallel}$ and $s_{\perp}$decays as the excited population undergoes rotational diffusion, or as the coordination and electronic environment about the absorber becomes more symmetric. For myoglobin, the rotational diffusion time (~3 ns) far exceeds the window of our experiments and its effects on the polarization dichroism can be neglected.

That the XAS features selectively probed in each polarization depend on the relative orientation of the orbital or atom that originates them to the transition dipole introduces another level of sensitivity in electronic structure and local geometry determination to XTA, and this technique is uniquely applicable to study CO photolysis from myoglobin. The optical excitation used to trigger photolysis in this work is a $\pi \rightarrow \pi^*$ transition, a mixture of two nearly degenerate transitions dipoles that lie in the plane of the porphyrin. Therefore $s_{\parallel}$ is preferentially sensitive to changes in the heme structure and electronic environment that take place in the heme plane, for instance Fe-N_p bond elongation that occurs as a consequence of heme doming as the complex becomes 5-coordinate, while $s_{\perp}$is more selective to changes normal to the heme plane, such as CO loss and Fe-histidine bond elongation.

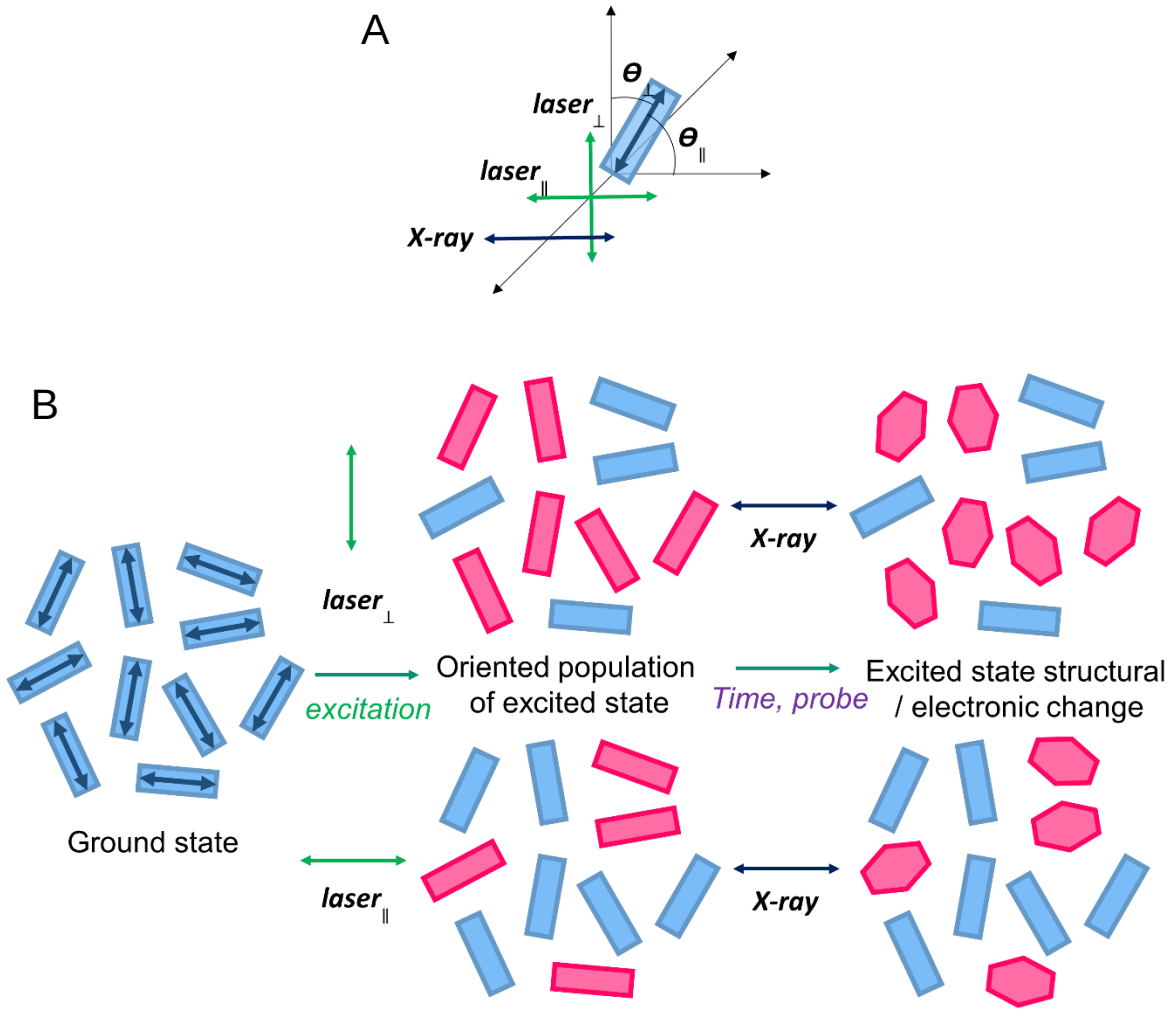

Figure 4.4: A) Definitions of relative polarizations of the X-ray and laser pulses. The probability of molecular excitation depends on the angle Θ between the laser polarization direction and the molecular dipole moment. B) Scheme showing the development of a partially ordered population of excited molecules on excitation with a laser pulse polarization perpendicular (above) and parallel (below) to the horizontal X-ray polarization.

For a description of the expected polarization dependence of each X-ray photon energy probed, see Results 4.3.1.

4.2. Method

4.2.1. Sample preparation and handling

A fresh solution of equine MbCO in a buffered, CO saturated solution was prepared for every 12 hr shift. For each batch, lyophilized ferric (Fe^{3+}) met-myoglobin (metMb) (Sigma) was dissolved in 50 ml of 100 mM potassium phosphate buffered to 7.4 pH to a concentration of 6 mM. A few drops of polypropylene glycol, a de-foaming agent, were added and the protein solution was sealed with a rubber septum. The solution was sparged for several minutes with a low flow of inert He via a gas line connected luer lock needle inserted into the septum. ~1.5 ml of a 0.75 M solution of sodium dithionite that was similarly de-oxygenated in a small vial was anaerobically added to the metMb solution via a gastight syringe needle to fully reduce the protein to the ferrous (Fe^{2+}) form and to eliminate any remaining dissolved oxygen. The ferrous deoxymyoglobin (deoxyMb) solution was saturated with CO by sparging for a few minutes to produce carbmonoxymyoglobin.

The MbCO solution was anaerobically transferred under slight positive He pressure to the beamline sample reservoir at the XPP endstation. In this case, the sample was circulated with an HPLC pump through a series of inline filters and to a small capillary nozzle that delivered a stable 50 um liquid jet to the He purged sample chamber and to the point of X-ray/laser overlap. A tube inlet at the base of the chamber recovered the sample for recirculation.

Before sample loading, full conversion to Carbmonoxymyoglobin was confirmed via UV-vis. Microliter aliquots were taken from the sample after loading and periodically throughout the shift to ensure the sample remained reduced and in a MbCO ligation state and that radiation damage from the X-ray or laser beams (which can lead to sample oxidation and aggregation) was minimal.

4.2.2. OPS-XTA measurement of CO photolysis

X-ray absorption measurements were taken at various energies up the Fe-K edge, primarily between 7111.0 eV and 7220eV, at the XPP endstation of LCLS. The 50 μm liquid jet was flowed vertically through a He purged airtight chamber with quartz and capton entrance ports for the nearly collinear laser and X-ray beams, respectively. CO photodissociation was triggered with a linearly polarized excitation pulse from the output of an optical parametric amplifier (OPA) pumped by a Ti:Sapphire laser. The 80 fs (FWHM) pulse duration, 20μJ/pulse optical pulse was used to excite a strong porphyrin-centered absorption feature at 527 nm, the porphyrin $S_0 \rightarrow S_1$ ($\pi \rightarrow \pi^*$) transition. The laser beam was focused to a 150 μm circular spot on the sample. These conditions were chosen based on the minimum laser power necessarily to achieve the optimal XAS difference signal. The polarization of the optical beam was controlled remotely with a motorized waveplate. Because the XFEL beam is horizontally polarized, the horizontal and vertical polarizations of the optical beam correspond to parallel and perpendicular polarizations in the lab frame respectively.

To obtain monochromatic X-rays (~1 eV bandwidth), a double Si(1,1,1) crystal monochromater was employed Unlike the channel cut Si(1,1,1) monochromater used in the NiTMP XAS experiments (see Methods Chapter 3), the ‘Large Offset” monochromater cannot be

quickly scanned to obtain a full time resolved XANES spectrum. Because changes in the beam energy involved a fairly time consuming process of re-alignment, we opted to take time scans of the XAS signal evolution at a few characteristic energies. To accomplish this we set the central energy of the XFEL bandwidth and monochromater angle to the energy of interest, realigned the lenses to position the beam on a fixed target position on an X-ray fluorescent screen, and performed scans of the pump-probe delay. This process was repeated for each change in the X-ray probe energy. The nominal X-ray pulse duration was tuned to 50 fs (FWHM). The X-ray beam was focused on the sample to a spot size of ~30 um (FWHM) upstream of the sample with XPP's series of Beryllium focusing lenses.

The XAS signal was collected in fluorescence mode by monitoring the total X-ray fluorescence in the horizontal plane of the of the sample and beam propagation direction using two solid state passivated implanted planar silicon (PIPS) point detectors (Canberra, Inc.) at 90^{o} with respect to the incoming X-ray beam. The incoming monochromatic X-ray pulse intensity was monitored for later pulse-by-pulse signal normalization by another PIPS detector located upstream of the sample chamber. The XAS signal for each individual X-ray pulse was collected at the 120 Hz repetition rate of the X-ray pulse and integrated for four seconds for a total of 480 single pulses per point. For about 6% of all shots (1 of every 17 shots), the optical pulse was dropped to allow monitoring of the ground state fluorescence signal as delay scans are collected. This acts as an indicator of drifts in the total ground state XAS signal that are independent from variations in shot-by-shot intensity, for instance due to fluctuations in the X-ray beam position or jet stability. Using these "drop shots" to calculate the total ground state fluorescence for each time step (I_{off}), the XAS

difference signal is reported as the ratio between the excited sample fluorescence and the ground state fluorescence as a function of time (I_{on}/I_{off}).

Unlike for our Ni K-edge experiments, the recently implemented XPP timing tool[115] was available to better characterize the pump-probe delay time, allowing us to significantly improve the time resolution of our experiment compared to the phase cavity correction employed at previous beamtimes. Although the intrinsic timing jitter of the XFEL pulses remains ~300fs, the timing tool provides shot-to-shot information on the relative arrival times of both the optical and X-ray pulse to a precision of a few femtoseconds, allowing for re-binning of all shots according to corrected arrival times. The timing tools acts as an X-ray/laser autocorelator, where the X-ray pulse changes the transmission of a thin substrate. The 300 fs timing jitter allowed us to take large steps (200 fs) in the nominal delay time relative to the experimental time resolution as the distribution of pulse arrival times ensured all later timing bins would be populated. The time resolution of the experiment was estimated to be ~80fs and is in this case limited by a combination of the optical pulse duration and the difference in velocity of the X-ray and laser pulses going through a 50 um thick water jet. This is in contrast to the NiTMP experiment where the time resolution was effectively limited by the timing jitter of the X-ray pulse.

Scans were taken from -1ps to 3ps delay time with respect to the optical excitation 200 fs increments. For each energy, groups of scans were taken with the laser polarization alternating every four scans.

4.2.3. Data processing

Data processing was carried out similarly as for the NiTMP data set with a few exceptions owing to the increased XAS signal strength due to machine improvements, the additional use of the XPP timing tool, and use of drop shots to correct for long term drifts affecting the XAS signal. After an initial rejection of very low X-ray intensity shots according to the upstream pulse intensity monitor I_0, this monitor was corrected for non-linearity with respect to the fluorescence detectors, which occurs at for high intensity shots (Figure 4.4) . Using the laser drop shots for each delay scan, the detector/normalization monitor correlation for both diodes was fit to a polynomial and shots in the non-linear region translated to a linear regression of the linear response region. This correction was then applied to pulse intensity data for all shots in that scan and the XAS fluorescence signal for each shot was normalized by the corrected intensity data. Shots were not rejected due to deviation from the detector/normalization correlation for a given time step as in previous experiments due to 1) much high quality D/I_0 correlations with narrower standard deviations compared to previous experiments and 2) a significant contribution to the spread of D/I_0 data for a single nominal time point is due to the XFEL timing jitter as opposed to detector noise, and this is later corrected in the re-binning of shots according to the timing tool data. The XAS difference signal for each shot was then calculated as the ratio between the normalized XAS signal for that individual shot and the average of all laser drop shots within 500 shots.

Finally, shots were filtered and binned according to the timing tool determination of their pump-probe delay. For each nominal time point, shots that fell out of a relatively narrow range about the nominal time (~200 fs FWHM) were discarded (Figure 4.6). Shots for the entire time scan were then sorted into 20 fs bins and the median XAS difference is reported for each bin.

4.2.4. Global fitting of the time dependent XAS difference

X-ray photon energies were selected for pump-probe delays scans based on features evident in the XANES difference spectrum obtained from previous APS experiments (Figure 4.7). The averaged perpendicular and parallel scans at each energy were fit globally to simulated traces based on a sequential kinetic model (equation 4.13). The simulation and iterative fitting of kinetics was conducted using a very similar method as in previous NiTMP analysis (see Chapter 3 Methods) with the exception that each species or population in the decay pathway was fit as a contribution to the XAS difference as opposed to the total XAS intensity. All other treatment of the simulated traces is identical, but the total *difference* in XAS absorption is expressed as a function of the X-ray photon energy E and the pump-probe delay time t at each energy,

$$\Delta \boldsymbol{A_{total}}(\boldsymbol{E}, \boldsymbol{t}) = \sum_{\boldsymbol{i=0}}^{\boldsymbol{n}} \Delta \boldsymbol{A_i}(\boldsymbol{E}) \boldsymbol{P_i}(\boldsymbol{t}) \qquad 4.2$$

4.3. Results and Discussion

4.3.1. Selection of X-ray probe energies

X-ray photon energies were selected based on features of the XANES difference signal obtained from previous synchrotron experiments.[116] Electronic and vibrational relaxation of the heme itself precedes the 100 ps delay at which XANES were previously measured, but CO recombination occurs on a much longer millisecond timescale. This difference signal therefore represents the spectral differences between a relaxed, deoxy-like state 100 ps after photolysis and the ground state MbCO spectra (Figure 4.7, Figure 4.2).

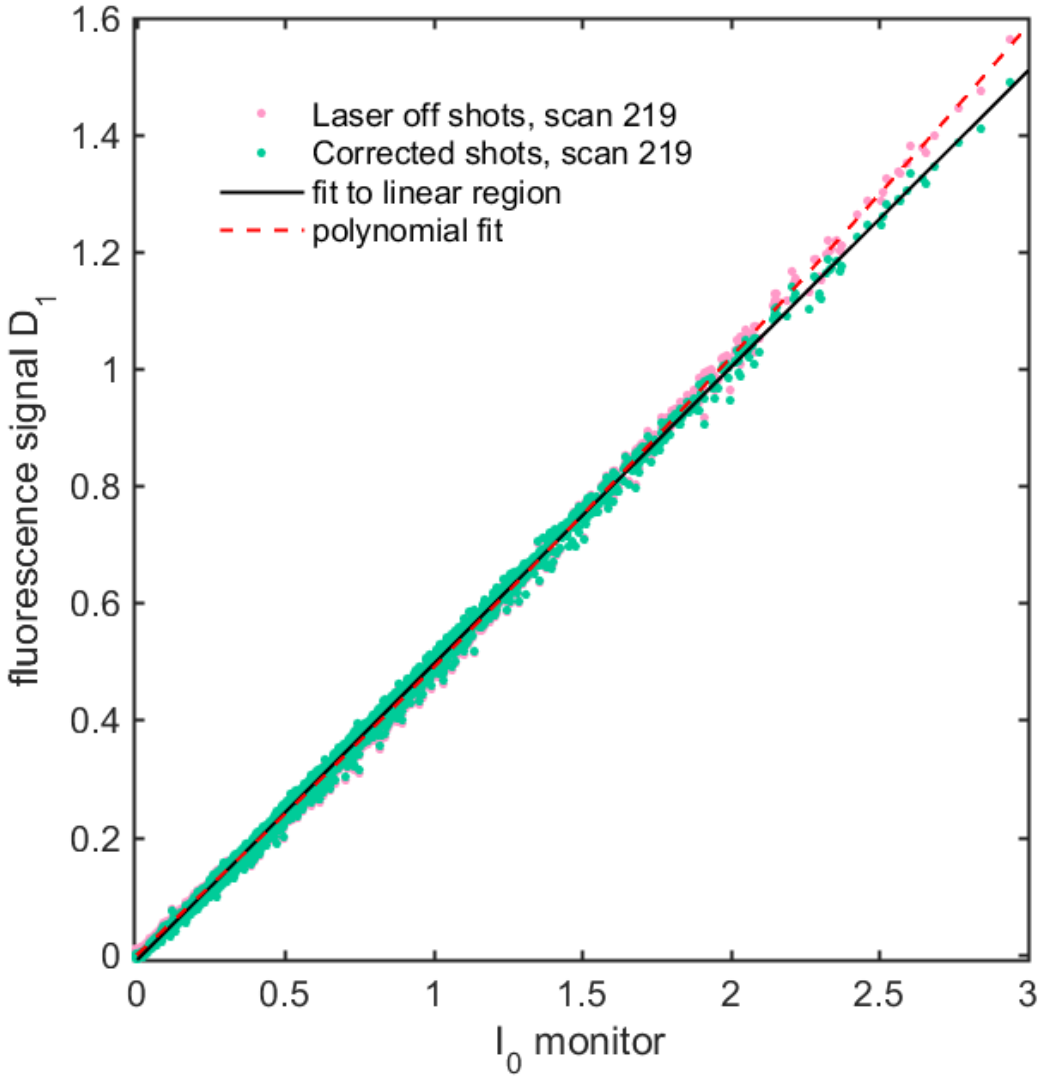

Figure 4.5: Correlation plot and correction of detector nonlinearity for a single scan. The fluorescence signal detected by each diode vs the intensity of the incoming X-ray pulses is fit to a second degree polynomial and fluorescence data for all shots is shifted by the difference between the polynomial fit and a linear fit to all shots for which $I_0 < 1$.

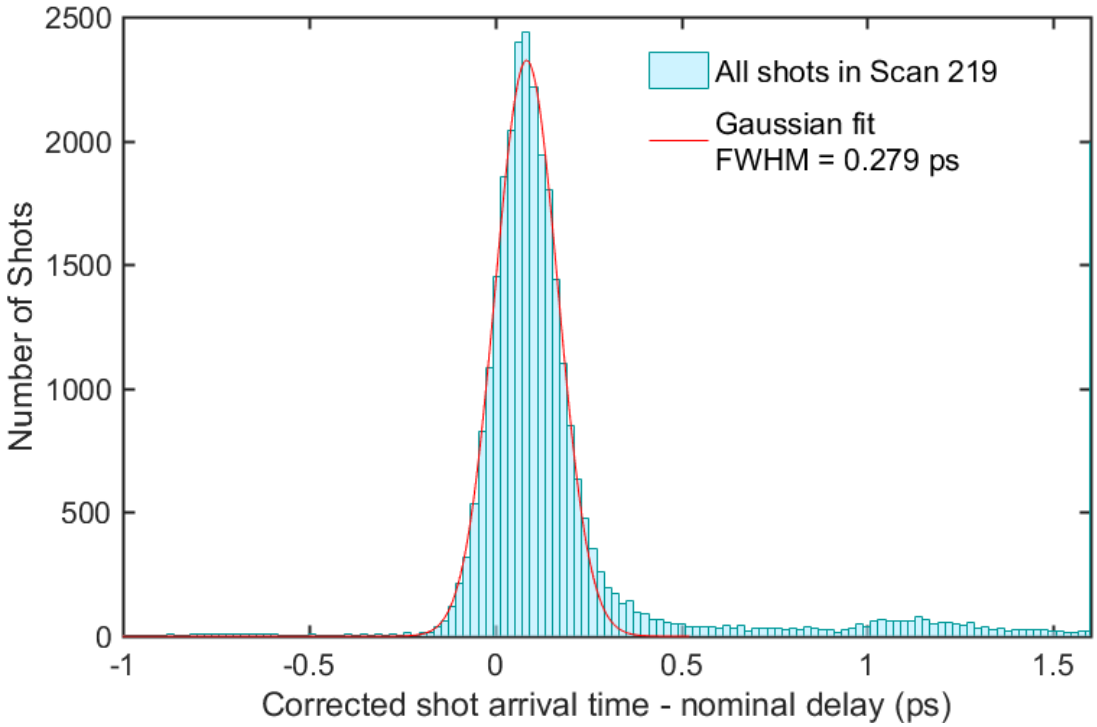

Figure 4.6: Distribution of shot arrival times for one time point. Each time point has four seconds integration time. Arrival times are reported as measured by the timing tool.

Several groups have partially assigned features of the MbCO and deoxyMb XANES based on a combination of electronic structure calculations and both steady state XANES of Mb in solution[117] and through series of polarized XANES of single MbCO and cryogenically trapped Mb*CO where CO is dissociated but bound elsewhere in the heme pocket. [118,119] [118,119] [118,119] Choices of X-ray probe energies were guided by which features showed the most polarization dichroism in these studies and which were assigned to scattering resonances or electronic transitions that had the most relevance to the myoglobin relaxation mechanism.[118,119]

The selected energies describe slightly different physical properties depending on the energy region of the spectrum. The pre-edge region (~7106 eV – 7117 eV) contains quadrupole allowed 1s → 3d transitions. Mixing of the 3d orbitals with the 4p grants more p character to the final state as the centriosymmetry of the environment decreases, making these transitions weakly dipole allowed for MbCO. Mixing and bonding with ligand orbitals also occurs and because the coordination environment is somewhat complex it's helpful to describe these transitions from a ligand field perspective. The MbCO XANES has two distinct peaks in the pre-edge region of the Fe K-edge at 7112 and 7115 eV. The first of these have been assigned to a combination of transitions of mostly 1s → d_{z2} and 1s → d_{x2-y2} character with significant hybridization with Fe 4p orbitals. These are transitions into the antibonding orbitals of the Fe-C σ sigma bond ($[3d_{z2} + \sigma(CO)]^*$) and the Fe-N_p σ bonds ($[3d_{x2-y2} + \pi_{porph}]^*$) respectively. The higher energy pre-edge peak is a signature of Fe-CO back bonding, where the occupied Fe $3d_{xz}$ and $3d_{yz}$ orbitals donate electron density to the π antibonding orbital of CO. This peak is derived from the antibonding orbital of this strong π bond, $[3d_{xz,}\ 3_{yz} + \pi^*(CO)]^*$.

Going higher up the edge, transitions into other vacant orbitals are expected and can be distinguished from the growing density of states at the rising edge if they have sufficient oscillator strength. One such feature is a low energy shoulder appears in the main edge shift peak at 7118 eV in the 100 ps difference spectrum (Figure 4.7), which is heme-normal polarized in polarized single crystal experiments.[118] DFT calculations of ground state deoxyMb K-edge transitions below and near the rising edge identify this feature as consisting mostly of Fe $4p_z$ hybridized with various orbitals of the His nitrogen.[117]

The edge position itself is determined by a combination of electronic and structural contributions, and for myoglobin the strong positive peak at 7123 eV in the difference spectrum (Figure 4.7) is thought to originate from several factors. First is the change in overall electron density centered on iron (Z_{eff}), which is greater in deoxyMb than MbCO due to electron density withdrawing from Fe d_{xz} and d_{yz} orbitals to CO as a result of back bonding, leading to a relative increase in energy of Fe 1s and shift in the edge to lower energy. Secondly, steady state polarized XANES on single crystals of MbCO and its photolysis product trapped at low temperature Mb*CO show that a large portion of the edge shift is heme-normal polarized,[118,120] suggesting that the electronic relaxation of the bound states with p_z symmetry going up the edge contributes to the reduction of the transition energy from 1s since there is now only one bond in the z direction. Finally, due to scattering contributions from first shell atoms, as the average Fe-ligand bond distance increases the edge position shifts to lower energies according to the Natoli rule.[121] This effect is often invoked to explain ligation or de-ligation induced edge shifts in hemes that have nominally unchanged Z_{eff}.[122,123]

Beyond the absorption edge, 7172 eV is on the low energy end of the EXAFS region, where contributions from single scattering events dominate. This energy is therefore insensitive to any electronic changes and changes depend only on nearest neighbor distances. The broad positive feature centered at 7170 eV in the 100 ps difference spectrum is indicative of a shift in the sum of the EXAFS oscillations, both due to the loss of an axial ligand and to the shift of the oscillation associated with the Fe-N_p scattering to higher frequency as the bond length increases.

4.3.2. Determination of the z component of the XAS signal

Because the two nearly degenerate $\pi \rightarrow \pi^*$ transition dipoles are orthogonal but both in the plane of the ring, the parallel polarization probes changes in the heme plane but acquires sensitivity to the heme normal from the distribution of heme orientations in solution where the projection of the electric field vector $\hat{\boldsymbol{e}}$ onto the molecular dipole moment μ is sufficient to excite the molecule but the angle between them, Θ, is non-zero. However, the perpendicular polarization contains contributions from both the heme plane and heme normal because these are equivalently orthogonal for an in-plane vector. Defining the heme normal direction as Z, and the plane of the heme as the X-Y plane gives us the axis of the molecular frame where X and Y are drawn along the Fe-N_p bonds (Figure 4.8A&B). Thus, the two transition dipole moments only have X and Y components and “in-plane” refers to changes in the X-Y plane. To isolate axial contributions to the signal, we have adapted a formalism used by Dau et. al. to describe steady state X-ray polarization anisotropy in partially ordered samples.[124]

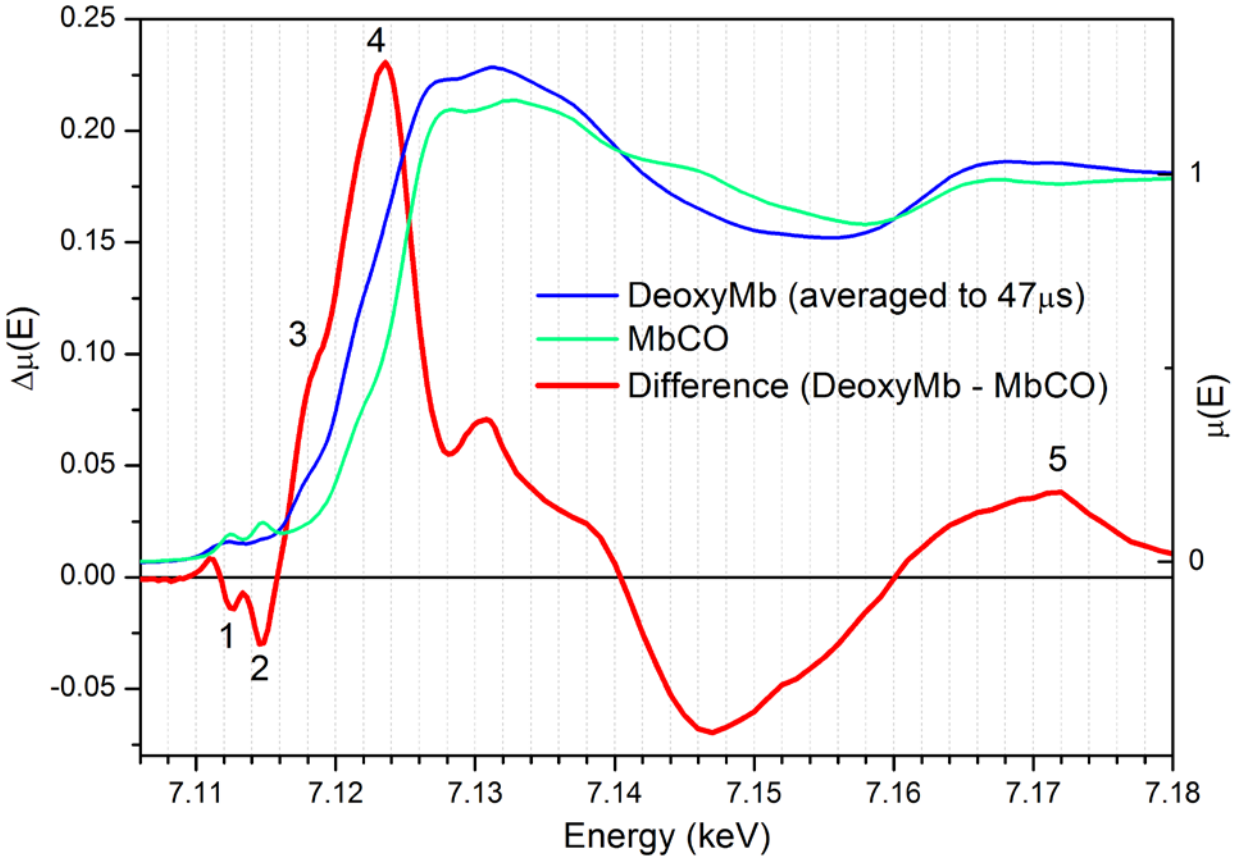

Figure 4.7: XANES and Difference spectrum obtained from sychrotron experiments.[116] Energies selected for measurement of polarization dependent dynamics are marked: (1) the depletion of the ground state transition of $1s \rightarrow 3d_{z2}$, $3d_{x2-y2}$ character, (2) the disappearance of the pre-edge peak associated with the CO back bonding antibonding orbital, (3) the rising edge shoulder that appears in deoxybyoglobin, (4) the edge shift, and (5) an EXAFS energy where changes are purely based on changes in the local geometry.

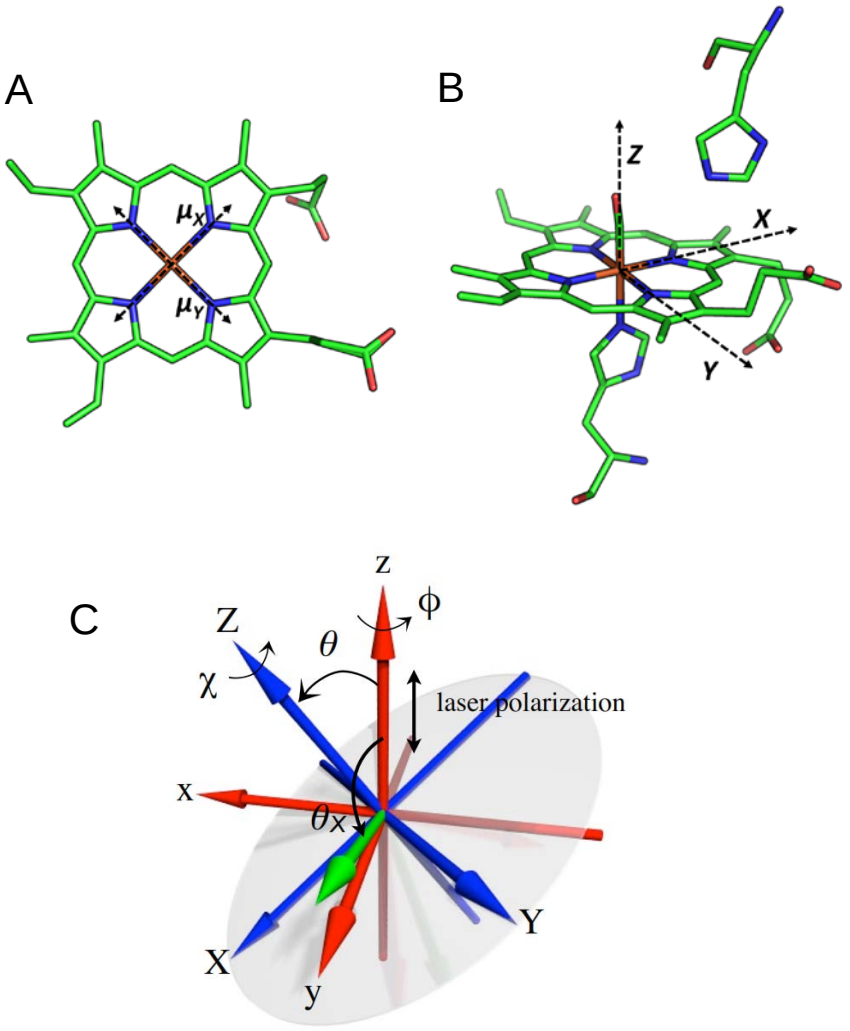

Figure 4.8: A) X and Y components of the in-plane transition dipoles for the π→π* transition. B) The molecular frame is defined by X,Y,and Z where Z is normal to the heme plane and the heme lies in the XY plane. C) Euler angle definitions used to solve for the c_z signal component. The heme is represented by the gray disk. The lab frames is defined by x,y, and z and translation between the lab frame and molecular frame is described by $\phi, \chi,$ and θ. The X-ray polarization vector (green) is at an angle θ_X from the laser polarization vector, which is aligned with z.

This formalism essentially develops an expression for the parallel and perpendicular signals ($s_{\parallel}$ and $s_{\perp}$) in terms of the contribution to the signal along each molecular axis by averaging the molecular signal contribution over an orientational distribution of excited molecules, which a probability distribution that depends on the alignment of the molecular axis with the laser polarization diection.

First we define the axes of the lab frame (x,y,z) with respect to the axis of the molecular frame (X,Y.Z) (Figure 4.8C). The angles θ and χ represent the rotation of the molecular frame about its own y and z axes respectively, ϕ represents the rotation of the molecular frame about the Z axis. Thus, every molecule in the solution orientation ensemble has an orientation defined by θ, χ, and ϕ in the lab frame. Because this formalism was developed for experiments in which the angle of the incident X-ray was varied and the axis about which order is defined is stationary, we define the laser polarization direction as static and parallel to the z axis while the X-ray polarization direction is described by the angle θ_X between the X-ray polarization vector and the z axis (laser polarization direction). To compute the contribution of a molecule to the total XAS signal as a function of its orientation, we translate the molecular orientation into the lab frame and the X-ray polarization direction onto the z axis:

$$s(\theta, \phi, \chi) = c_x(\hat{u}_x \cdot \hat{\varepsilon})^2 + c_y(\hat{u}_y \cdot \hat{\varepsilon})^2 + c_z(\hat{u}_z \cdot \hat{\varepsilon})^2 \qquad 4.3$$

where c_x, c_y, and c_z are the components of the polarization dependent absorption signal from each molecular coordinate, $\hat{u}_x$, $\hat{u}_y$, and $\hat{u}_z$ are unit vectors along the molecular axis in the lab frame, and $\hat{\mathcal{E}}$ is a unit vector along the X-ray polarization direction.

Because $\hat{\varepsilon}$ is defined only by an angle between the x and y axis, θ_X, the angle between the X-ray and laser polarization vectors, $\hat{\varepsilon}$ has only x and y components dependent on θ_X:

$$\hat{\varepsilon} = (0, -\sin\theta_X, \cos\theta_X) \qquad 4.4$$

We would like to obtain an expression for the Z component of the X-ray signal that only depends on the relative polarizations of the X-ray and laser, θ_X. Thus, we must account for the orientational distribution of excited molecules created by the laser pulse. The probability distribution of excited molecules created by optical excitation can defined as a function of θ because this defines the angle between laser polarization vector, parallel to z, and the molecular transition dipoles in the X-Y plane. This probability distribution takes the same form as equation 4.1 where $P(\theta) \propto cos^2\theta$. For an orientational distribution of excited molecules with the probability distribution $P(\theta)$, the *total* signal s is a rotational integration about ϕ, χ, and θ to account for all orientations in solution:

$$s = \int_0^{2\pi} d\phi \int_0^{2\pi} d\chi \int_0^{\pi} s(\theta, \phi, \chi) P(\theta) \sin\theta d\theta \qquad 4.5$$

Integrating out ϕ and χ and substituting in the expression for $s(\theta, \varphi, \chi)$ (Equation 4.3),

$$s = \frac{1}{3}(c_x + c_y + c_z) - \frac{1}{6}(2c_z - c_x - c_y)(3\cos^2\theta_X - 1)I_{\text{org}} \qquad 4.6$$

where I_{org} is the "order parameter", a measure of the relative degree of order in θ. The absolute value of I_{org} varies between zero for an isotropic distribution and unity for perfect orientation:

$$I_{\text{org}} = 2\pi^2 \int_0^{\pi} (3\cos^2\theta - 1) P(\theta) \sin\theta d\theta \qquad 4.7$$

Using the normalized rotational distribution for $P(\theta)$,

$$P(\theta) = \frac{3}{16\pi^2} \sin^2\theta \qquad 4.8$$

I_{org} can be integrated to yield $I_{org} = -\frac{1}{5}$. Substituting this solution into (4.7) results in:

$$s = \frac{1}{3}(c_x + c_y + c_z) - \frac{1}{30}(2c_z - c_x - c_y)(3\cos^2\theta_X - 1) \qquad 4.9$$

Now that we have an expression for the total signal that depends on θ_X, we can write expressions for the parallel and perpendicular signals where $\cos(\theta_X)$ has values of 1 or 0 respectively,

$$\cos\theta_X = 1 \quad s_{\parallel} = \frac{1}{3}(c_x + c_y + c_z) - \frac{1}{15}(2c_z - c_x - c_y)$$
$$\cos\theta_X = 0 \quad s_{\perp} = \frac{1}{3}(c_x + c_y + c_z) + \frac{1}{30}(2c_z - c_x - c_y) \qquad 4.10, 4.11$$

Solving for c_z in terms of $s_{\parallel}$ and $s_{\perp}$,

$$s_{\perp} - \frac{3}{4} s_{\parallel} = c_z/4 \qquad 4.12$$

Thus, the component of the signal dependent on out-of-plane dynamics (c_z) can be relatively simply extracted from the perpendicular and parallel delay scans. However, this subtraction significantly compounds the level of noise in these traces, which become very sensitive to small relative fluctuations in the parallel and perpendicular signal. They are plotted with the respective

parallel and perpendicular traces at each energy to emphasize the difference between the dynamics for each polarization but are not separately analyzed to obtain kinetics.

Averaged parallel and perpendicular scans are shown with c_z for 7112, 7115, 7118, 7123, and 7172 eV (Figures 4.9-4.13). At all energies, perpendicular scans have consistently faster rises (or decays in the case of a negative signal) than their corresponding parallel traces. This is consistent with the fact that the fastest and most dramatic coordination change, the dissociation of CO, is focused along the Z axis.

The red-shift of the Fe K-edge position, monitored chiefly at 7123 eV (Figure 4.12) where the XANES difference signal is maximized and also at 7118 eV (Figure 4.11) which is at the low energy end of the rising edge, mostly appears to occur very rapidly (<100 fs) and this rapid growth accounts for the majority of the XANES difference at these energies. The perpendicular polarization is more sensitive to this fast phase, suggesting that the initial edge shift cannot be solely attributed to the expansion of the Fe-N_p bonds as CO dissociates and heme the heme domes. The parallel and perpendicular polarizations at 7123 eV are slightly separated in intensity even after several picoseconds, which indicates that the edge shift is more dependent on Z direction contributions even after some relaxation, although based on the slight ~ 500 ps decay of c_z there are slower processes in the heme plane that lead to depolarization.

The perpendicular polarized scans at 7172 eV (Figure 4.13) also exhibit a fast rise followed by a slower increase in the difference signal.

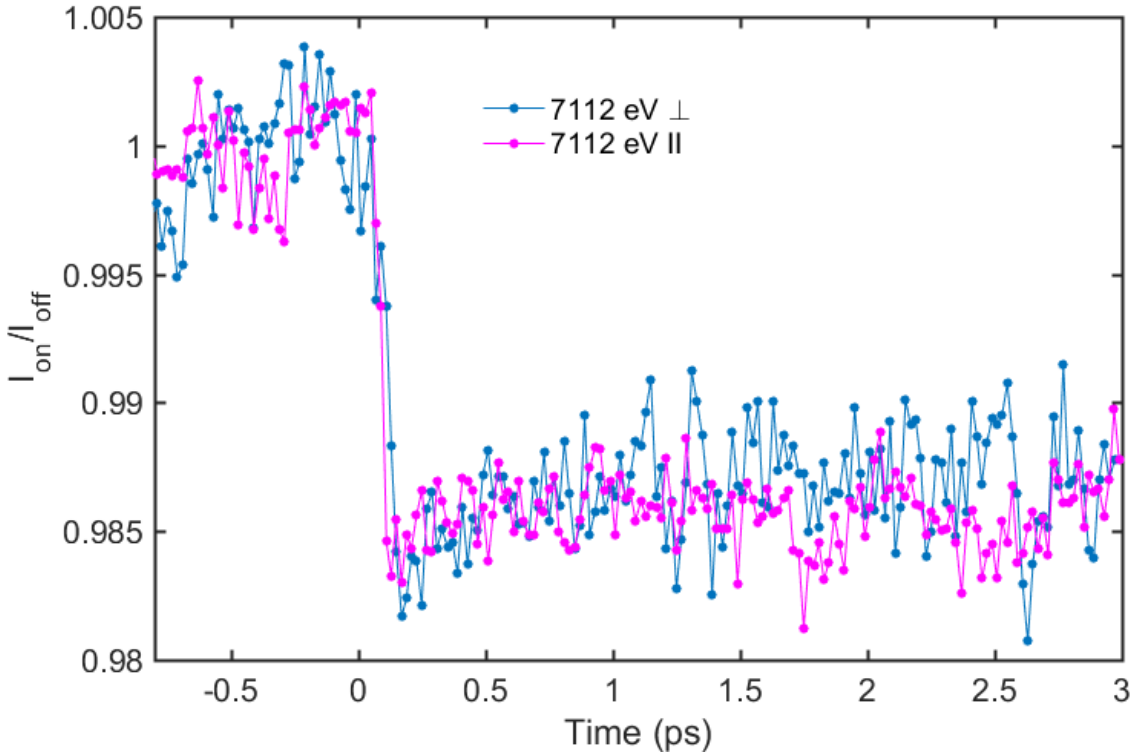

Figure 4.9: Averaged time delay scans at (1) 7112 eV for the parallel and perpendicular polarizations. Data is normalized by the ground state signal intensity measured by laser drop shots throughout the scan and is represented as I_{on}/I_{off}.

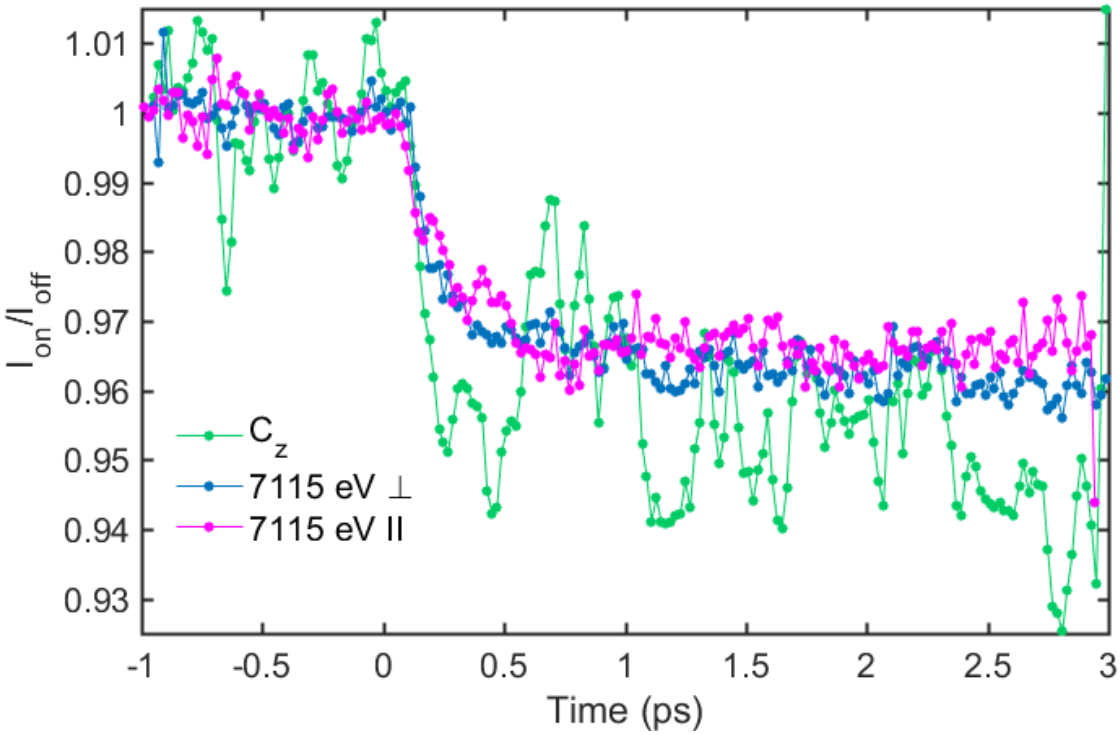

Figure 4.10: Averaged time delay scans at (2) 7115 eV for the parallel polarization, perpendicular polarization, and the z component of the signal, c_z.

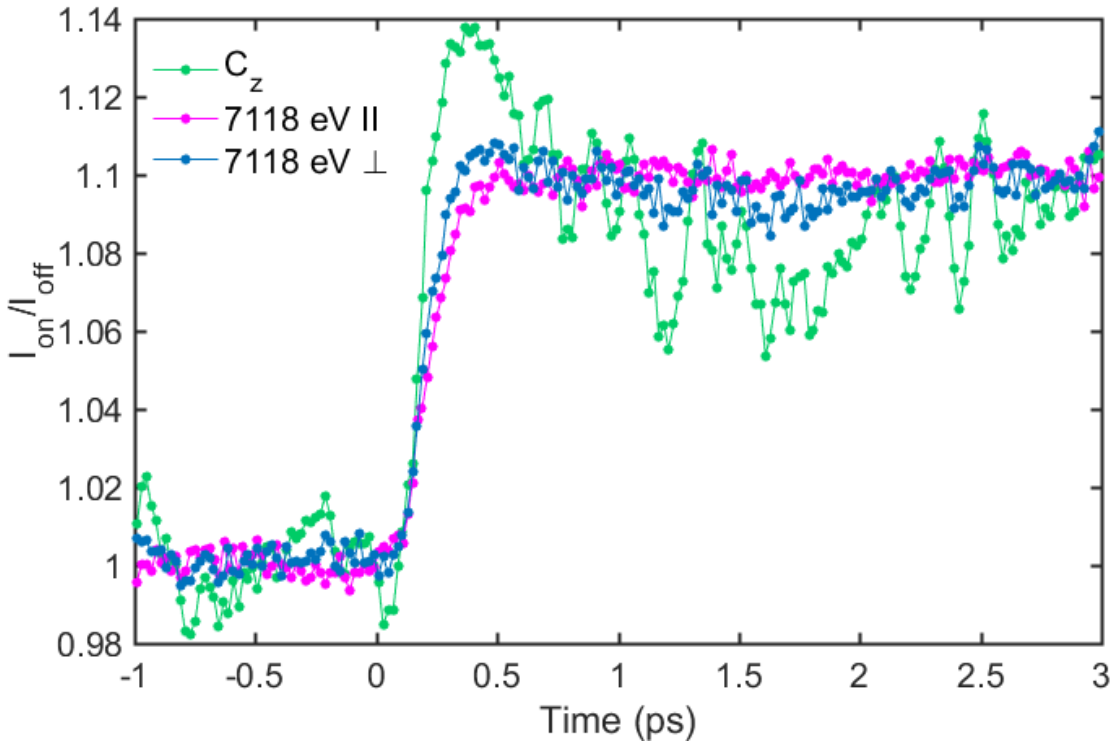

Figure 4.11: Averaged time delay scans at (3) 7118 eV for the parallel polarization, perpendicular polarization, and the z component of the signal, c_z.

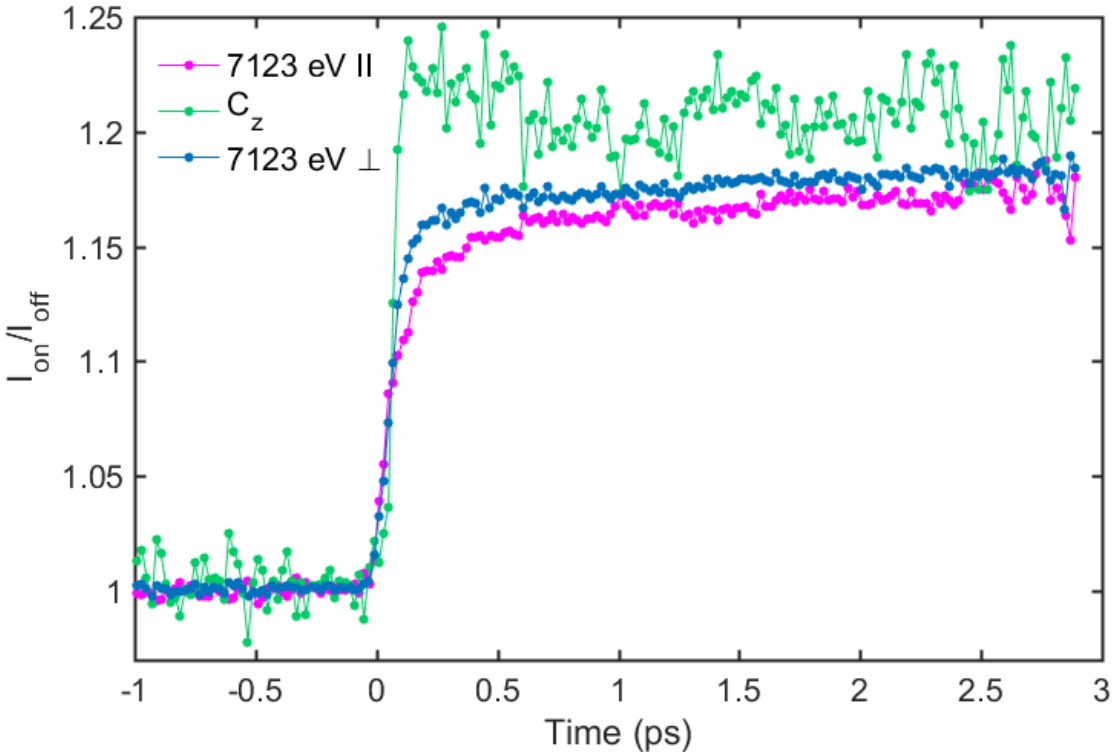

Figure 4.12: Averaged time delay scans at (4) 7123 eV for the parallel polarization, perpendicular polarization, and the z component of the signal, c_z.

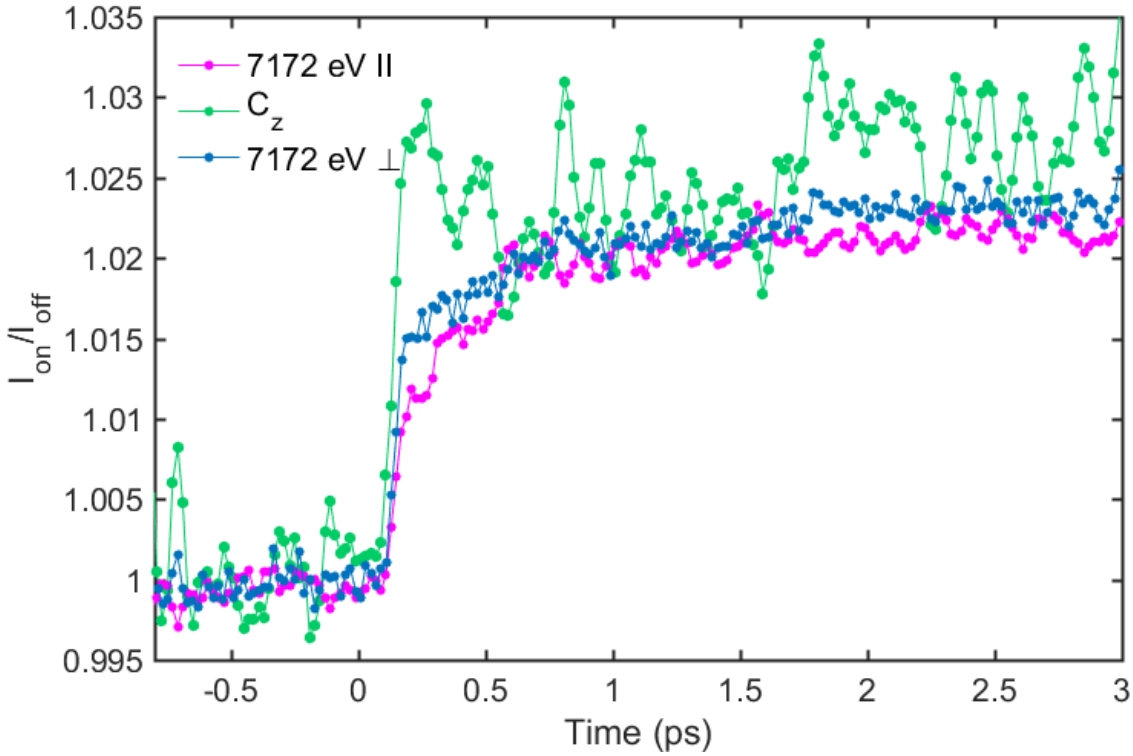

Figure 4.13: Averaged time delay scans at (5) 7172 eV for the parallel polarization, perpendicular polarization, and the z component of the signal, c_z.

Because this energy is mostly dependent on the number ligands directly coordinating Fe and their relative bond lengths, we can interpret this sharp rise as directly due to the loss of CO as an axial ligand. The perpendicular polarization has less of this sharp rise and evolves more slowly within the first picosecond.

In scans at 7118 eV (Figure 4.11), a rapidly forming component grows in within 100 fs and for perpendicular scans exceeds the XAS signal at later times and decays within about 1 ps. This component is noticeably z polarized, but c_z reflects the relative decay of the Z contribution to the perpendicular difference signal as the perpendicular scans dip below the parallel difference. At 7115 eV (Figure 4.10), the slowness of the signal decay is surprising given that this transition is assigned to the CO back bonding antibonding orbital. Ultrafast optical and vibrational techniques agree that the departure of CO occurs in less than 100 fs and while some component this feature's decay is rapid, there are also large contributions from slower dynamics.

At 7112 eV (Figure 4.9), the dynamics for both polarizations can generally be described as a very fast drop followed by an essentially featureless plateau with a hint of slow decay in the negative difference that mirrors the dynamics of 7123 eV c_z, although the signal is quite weak at this energy and more subtle evolution may not be resolvable given the low signal to noise. This pre edge peak shifts slightly lower in energy in deoxyMb, but not enough to explain this sharp drop as the shift of the pre edge to lower energy, after which no other dynamics are observed. That the drop at 7112 eV is so immediate and does not further evolve suggests that the processes that have the most impact on the magnitude of this feature occur simultaneously and within 100fs. These are the loss of CO to reduce the ligand field splitting and increase 4p mixing, which is expected to be very rapid, and the transition from a low spin to high spin system.

A sub 100 fs spin transition would have implications for the mechanism of myoglobin relaxation following photolysis. Several models that view the relaxation of the (π, π^*) state as proceeding through a series of electronic intermediate states describe the spin transition as occurring on the hundreds of femtoseconds to picosecond timescale. A sub 100 fs spin transition would be more in line with models that portray myoglobin relaxation as the rapid population of the high spin deoxyMb ground electronic state followed by various structural and vibrational relaxation events.

4.3.3. Global fitting of XANES difference evolution

The advantage of collecting delay scans at both polarizations is that kinetics can be more easily assigned to specific electronic or nuclear relaxation process based on their polarization dependence. To better determine the distinct relaxation processes involved in the XAS dynamics, both polarizations at each energy were globally fit to a sequential model as described in Methods with the exception of data at 7112 eV. The lower energy pre edge feature was excluded due to low signal level and the apparent lack of dynamics. Fitting was attempted using several different simple kinetic models but a sequential model was chosen because it was required to fit certain features of the data.

The vast majority of pump probe studies of CO photolysis in myoglobin find their data can be described as a three or four step sequential process beginning with the (π, π^*) Franck Condon state (S_1) and ending with the partially relaxed high spin deoxy heme (Mb_{HS}). Full vibrational relaxation of the heme is thought to occur within 15-20 ps, but we will focus on processes within the first few picoseconds.

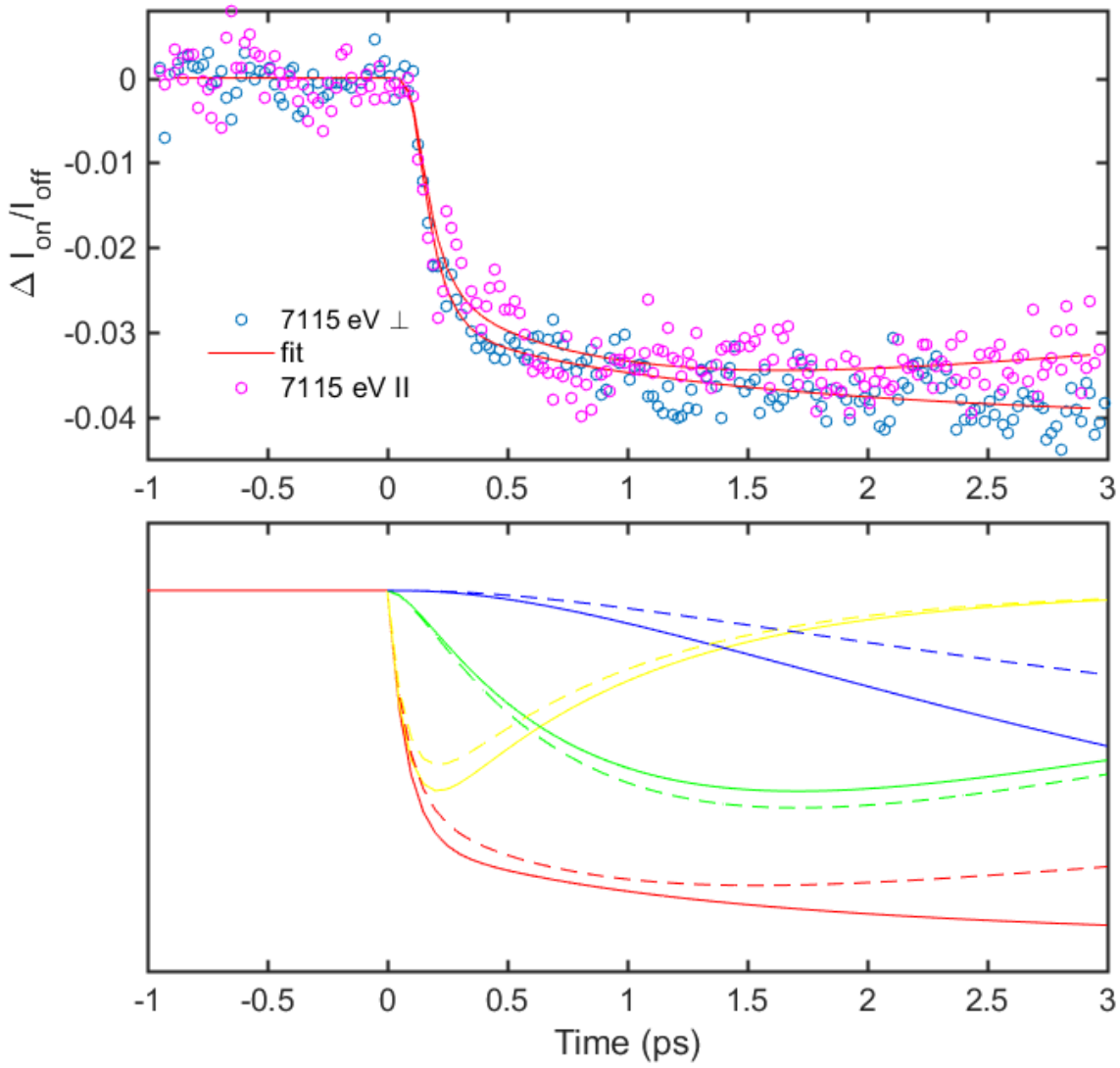

Figure 4.14: Global fits to a three step sequential model for both polarizations at (2) 7115 eV. Components of the fits from each species are shown in the lower panel for the perpendicular (solid) and parallel (dashed) polarizations.

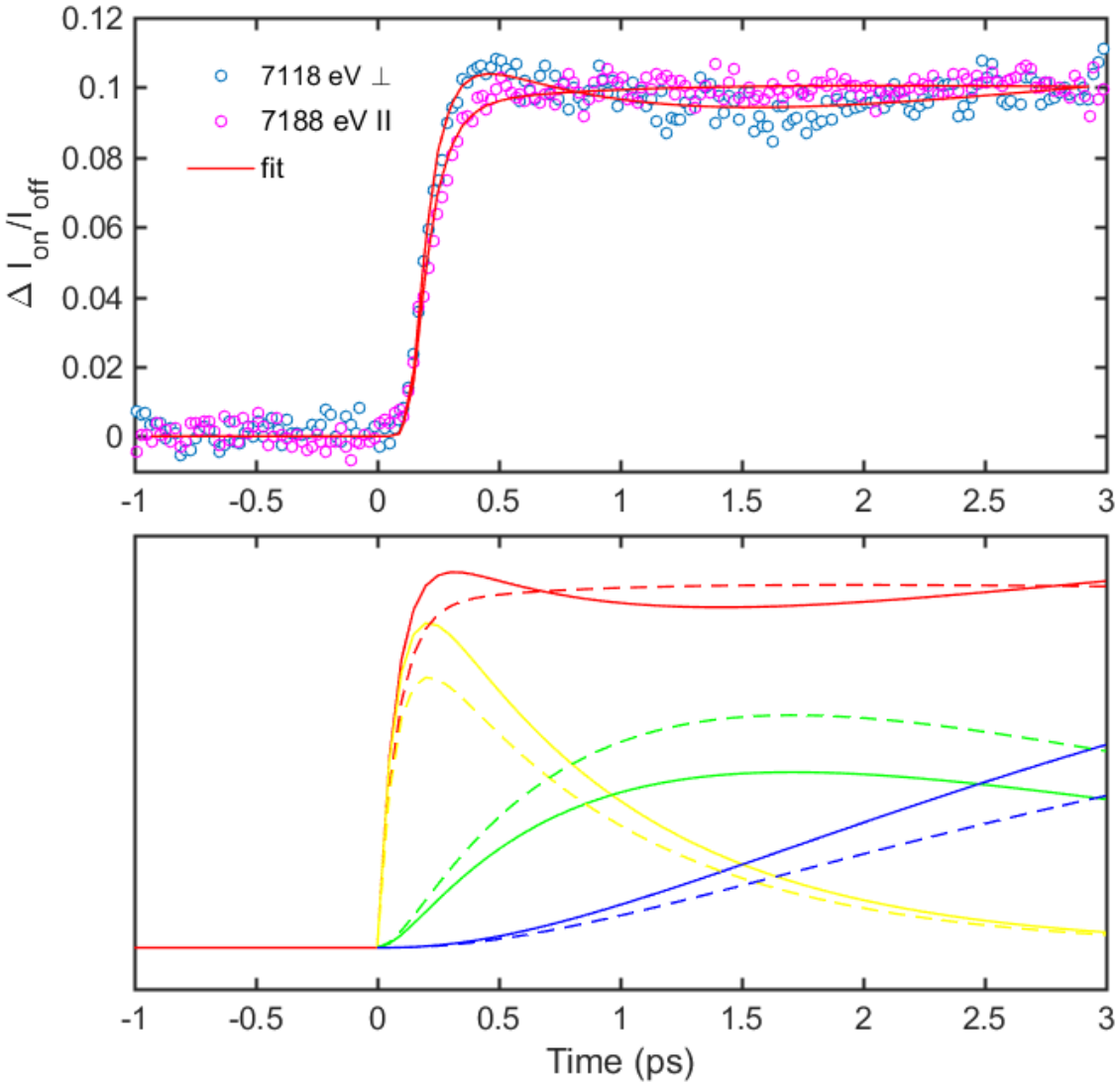

Figure 4.15: Global fits to a three step sequential model for both polarizations at (3) 7118 eV. Components of the fits from each species are shown in the lower panel for the perpendicular (solid) and parallel (dashed) polarizations.

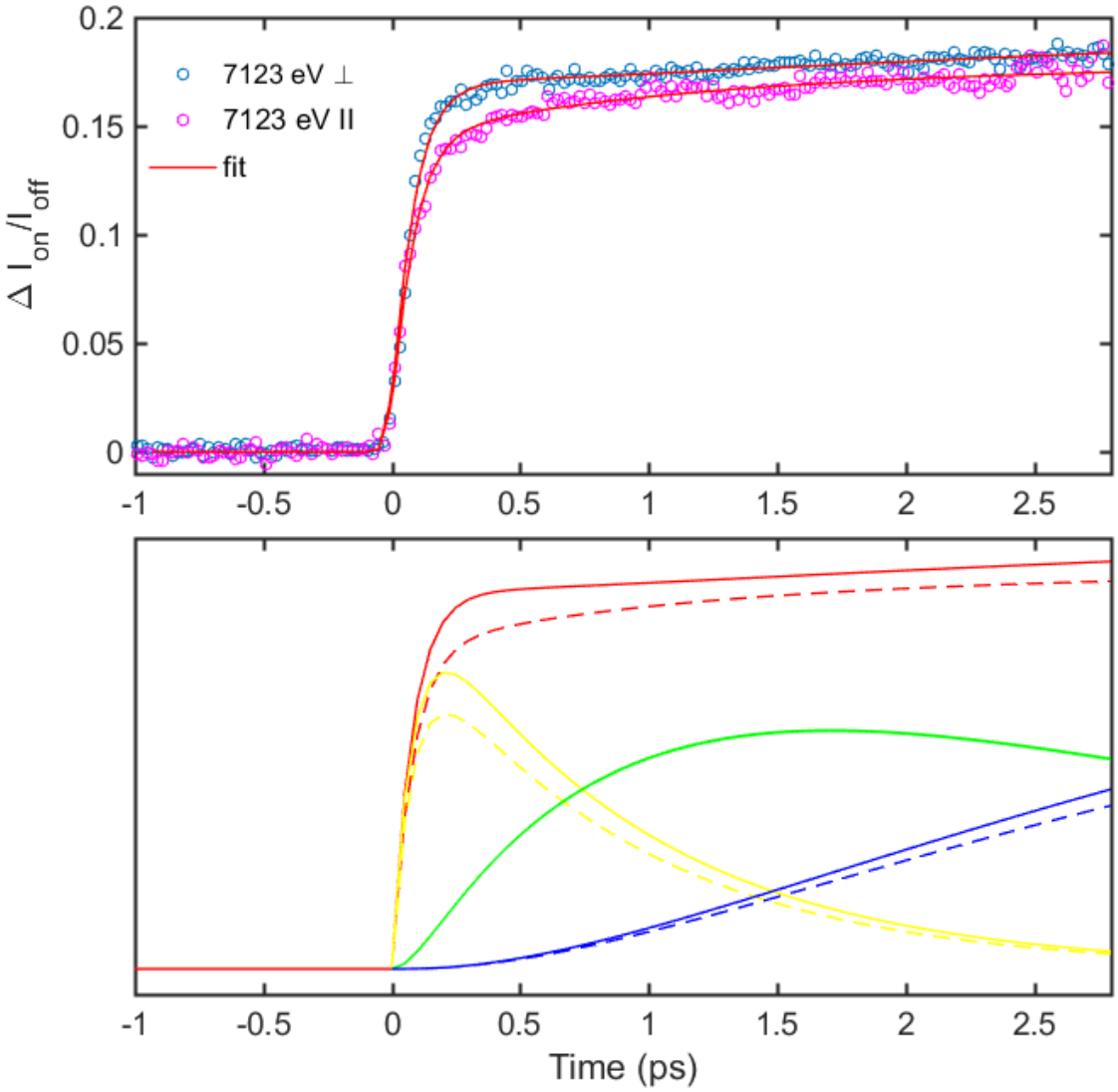

Figure 4.16: Global fits to a three step sequential model for both polarizations at (4) 7123 eV. Components of the fits from each species are shown in the lower panel for the perpendicular (solid) and parallel (dashed) polarizations.

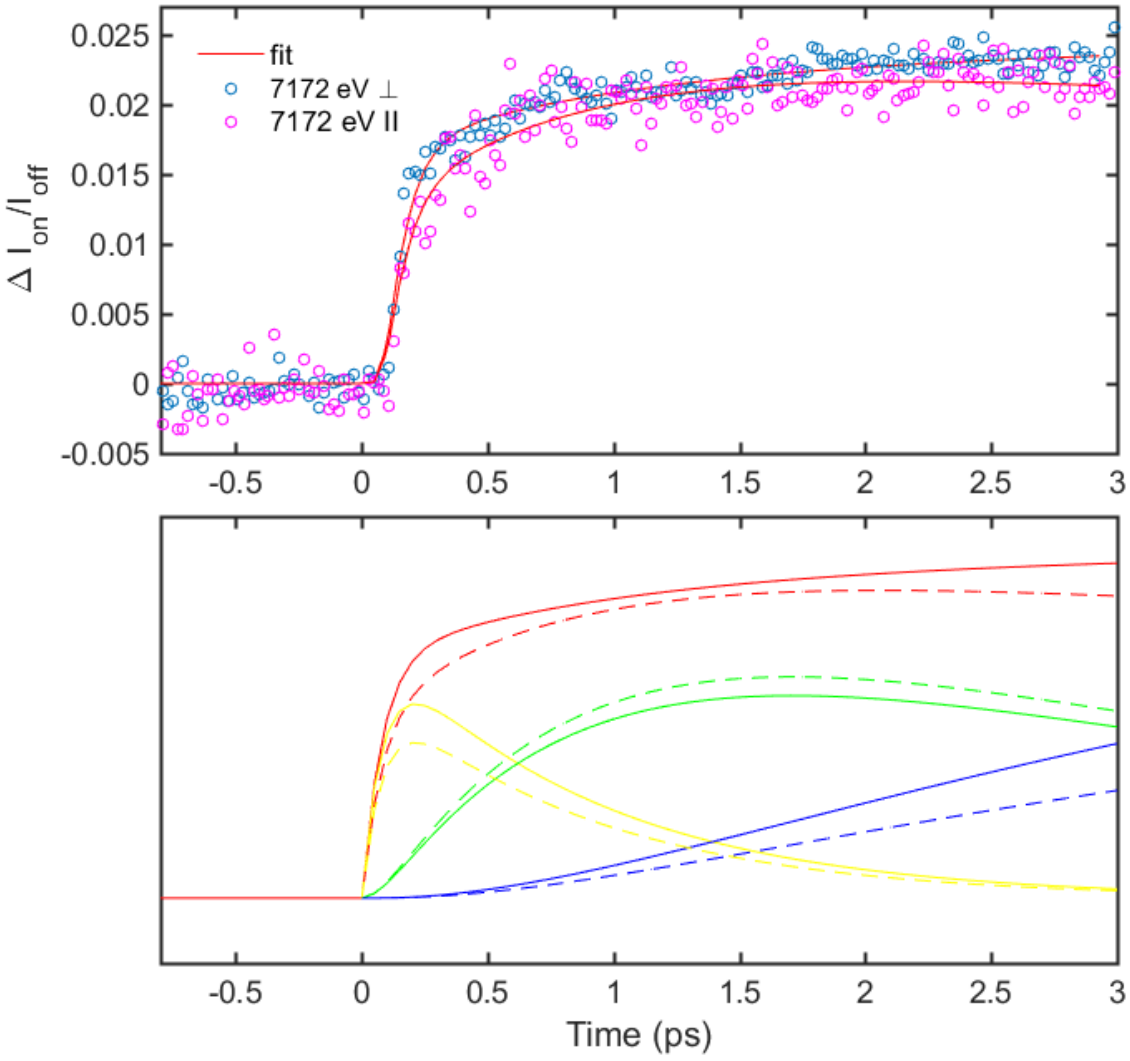

Figure 4.17: Global fits to a three step sequential model for both polarizations at (5) 7172 eV. Components of the fits from each species are shown in the lower panel for the perpendicular (solid) and parallel (dashed) polarizations.

The scheme used to fit the kinetics data is defined:

$$S_1 \overset{\tau_1}{\rightarrow} Mb^{*I} \overset{\tau_2}{\rightarrow} Mb^{*II} \overset{\tau_3}{\rightarrow} Mb_{HS} \qquad 4.13$$

where Mb^{*I} and Mb^{*II} are undefined species or populations prior to assignment by comparison of their polarization dependence. Three time constants and three species or populations were required to adequately fit the data as represented in equation 4.13, where $\tau_1 = 0.08 \pm 0.01$ ps, $\tau_2 = 0.89 \pm 0.12$ ps, and $\tau_3 = 3.46 \pm 2.01$ ps. Because we only sample the first 3 ps after excitation, the 3.46 ps time constant is at the upper limit of what is resolvable under our experimental conditions, but fits invariably fail without the inclusion of a longer time constant. The instrument response function obtained from the global fit was 0.07 ± 0.01 ps, close to our estimate of 0.08 ps.

Fits for each energy and polarization are plotted in Figures 4.14-4.17 in the top panel while the contribution of Mb^{*I}, Mb^{*II}, and Mb_{HS} to the difference signal is shown in the lower panel. Values of ΔA for each component are tabulated in Table 4.1. Because the S_1 state is very similar in geometry and in the electronic structure of orbitals with a lot of iron character (as the excitation is localized on the ligand), S_1 is expected to have a negligibly small ΔA and it is not included in the fits.

Table 4.1 Fitted values of ΔA for Mb^{*I}, Mb^{*II}, and Mb_{HS} at each energy and polarization data was taken.

Energy (eV)	**$\Delta A_\perp$**			**$\Delta A_\parallel$**		
	Mb^{*I}	Mb^{*II}	Mb_{HS}	Mb^{*I}	Mb^{*II}	Mb_{HS}
7115	-0.026	-0.033	-0.037	-0.023	-0.036	-0.020
7118	0.10	0.07	0.11	0.083	0.090	0.085
7123	0.14	0.15	0.18	0.12	0.15	0.16

7172	0.015	0.020	0.022	0.012	0.022	0.015

For all energies, the absolute value of ΔA for Mb^{*I} and Mb_{HS} is larger in the perpendicular polarization than in the parallel polarization, while the opposite is true for Mb^{*II}. Except for 7118 eV in the perpendicular polarization, Mb^{*I} ΔA is smaller than Mb^{*II} ΔA, especially for the parallel polarization. Mb^{*II} $\Delta A_{\perp}$ is in turn smaller than Mb_{HS} $\Delta A_{\perp}$, while Mb_{HS} $\Delta A_{\parallel}$ is smaller than or about the same magnitude as Mb^{*II} $\Delta A_{\parallel}$.

4.3.4. Implications of XAS dynamics for CO photolysis and the heme relaxation mechanism

Put together, the time constants and ΔA values obtained by the global fit, observations at individual energies, and building on information supplied by other studies, some conclusions can be made in the relaxation processes of myoglobin after photolysis and Mb^{*I} and Mb^{*II} can be assigned. That energies that are only sensitive local geometry have the same rapid time constant as energies that are more dependent on the iron electronic state suggests that an initial structural change occurs simultaneously with an initial electronic change with no lag in nuclear relaxation. Based on the immediacy of the signal drop and subsequent modest evolution at 7112 eV, which as discussed above cannot come solely from the change in ligand field on CO departure, these processes appear to be the high spin to low spin transition and the dissociation of CO. Thus, the initial Z polarized component, Mb^{*I}, embodies all the effects on the XANES directly related to CO departure: the loss of the $[3d_{xz,}\ 3_{yz} + \pi^*(CO)]^*$ antibonding orbital at 7115 eV, the fraction of the edge shift at 7123 eV and 7118 eV caused by the increase in Z_{eff} and by relaxation of states with p_z symmetry, and the loss of an axial scattering path at 7172 eV. The heme plane polarized nature of Mb^{*II} is compelling evidence that the rise of this species is due to Fe-N_p bond elongation.

Recent ultrafast small angle scattering studies by Levantino and Cammarata show that the force exerted on the F-helix where the axial histidine of myoglobin is bound causes the helix to move with a time constant of 400 fs.[125] This provides a benchmark of the Fe-N_{His} bond expansion time after it is compressed by Fe out of plane movement following CO dissociation, which must occur on the same timescale as F helix movement. The ~800 fs time constant, which determines the decay of Mb^{*I} and the rise of Mb^{*II}, is the best matched time constant and the structural implications of this assignment can be rationalized with the data. Mb^{*I} is formed with the dissociation of CO and it is likely that some amount of Fe out of plane movement happens nearly simultaneously with CO departure, leading to small changes in the Fe-N_p distances and the compression of the Fe-N_{His} bond. The 80 fs time constant derived from the global fit therefore describes a simultaneous CO departure and F-N_{His} compression (Figure 4.18).

Initially, the F-helix likely restricts the degree of out of plane moment of iron. In single crystal steady state XANES studies where CO phototolysis was induced in myoglobin at cryogenic temperature, a structural analysis of the XANES found a similar unrelaxed heme structure to that proposed for Mb^{*I} as the movement of the F-helix was arrested.[120]. The heme plane polarization of Mb^{*II} indicates that it is responsible for the majority of the Fe-N_p elongation, which must happen simultaneously with the elongation of the Fe-N_{His} bond and the further movement of iron out of the heme plane as the F-helix is displaced. The 800 fs time constant accounts for this secondary structural relaxation process and the XANES reflect the effects of Fe-N_p elongation, which additionally contributes to the edge shift and lends a slow rise to the dynamics at 7172 eV. This also explains the trend of larger values of ΔA for Mb^{*II} compared to Mb^{*I} as these changes positively compound on the difference signal that arises from the formation of Mb^{*I}.

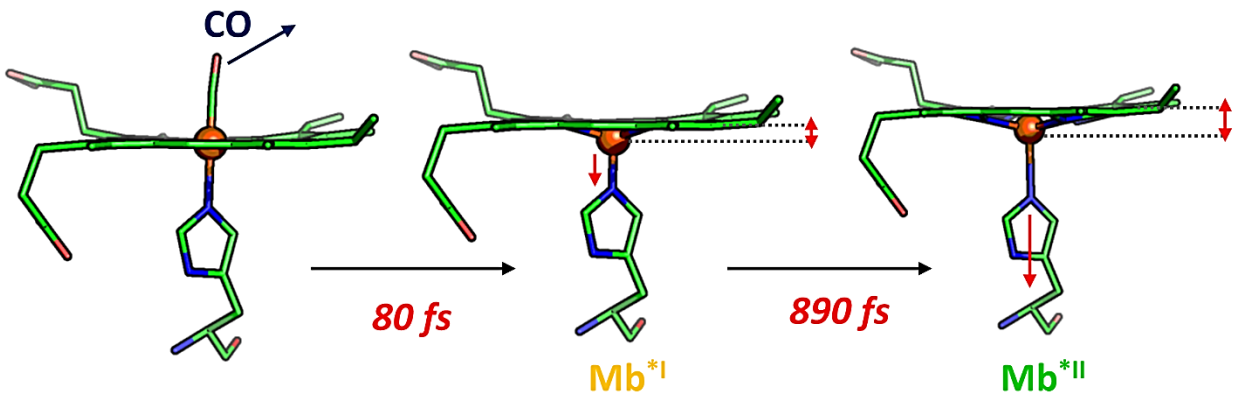

Figure 4.18: Proposed mechanism of heme relaxation following photodissociation of CO. The 80 fs components is attributable to CO loss, the low spin to thigh spin transition, a small displacement of Fe out of heme plane, and compression of Fe-N_{His} bond. The 890 fs component is due to Fe-N_{His} bond elongation as the F helix moves, and heme conformational relaxation (expansion of Fe-N_p bonds, heme doming, and further Fe out-of-plane plane displacement).

The ~3 ps rise of Mb_{HS} can therefore be ascribed to some component of the vibrational relaxation of heme. Picosecond resonance Raman studies find a similar time constant (~3 ps) for the relaxation of high frequency in-plane modes of heme.

However, the behavior of $\Delta A_{\perp}$ at 7118 eV, especially for Mb^{*I}, is not fully explained by this assignment. DFT calculations by Lima et al. suggest this feature in deoxyMb is due to a high density of states with mixed histidine ligand – Fe 4pz character, but without additional calculation it's difficult to speculate on how these states are affected by the changing Fe-N_{His} bond length. The dynamics at 7115 eV are similarly dominated by electronic effects and appear to be influenced changes in addition to the loss of the CO back bonding antibonding orbital which additional electronic structure calculations would help elucidate.

4.4. Summary

We have demonstrated that a polarization dependent dichroism of the evolution of the XANES signal can be detected and interpreted even for an excited population with relatively low order compared to systems usually studied by polarization-dependent XAS. To our knowledge this is the first observation of polarization-dependent XAS dynamics for an oriented population generated only by photoselection, which represents an additional dimension of structural and electronic information that can be extracted from ultrafast XAS. While myoglobin's nanosecond rotational diffusion time ensures almost no decay of the excited state orientational anisotropy, this effect should also be observable for molecular systems for short time delays.

We have interpreted the polarization dependence of global fit kinetic fit components towards a mechanism for myoglobin active site relaxation. In sum, the data indicates a rapid displacement

of iron out of the heme plane which occurs with a time constant of 80 fs as CO dissociates, accompanied by a low spin to high spin transition and the compression of the Fe-N_{His} bond. Movement of the F-helix, elongation of the F-N_{His} bond, and expansion of the F-N_p bonds occur simultaneously with a time constant of 0.89 ps, while the initial relaxation of in-plane modes occurs with a time constant of 3.4 ps.

Chapter 5. Jahn Teller Dynamics in Zn-substituted Hemoproteins and Model Compounds

5.1. Introduction

Long-range electron transfer (ET), a critical process in redox-active biological systems particularly in energy transduction processes such as respiration and photosynthesis, is often carried out by hemoproteins. Hemoprotein active site structure has a profound influence on factors that affect ET, such as ligand affinity,[126] redox potential,[127-129] adjustment of the active site electric field.[130], and heme conformation.[18,131,132] The protein environment perturbs the heme conformation through direct ligation to iron, covalent linkages between binding site resides and heme side groups, and non-bonding contacts with the amino acids that compose the heme pocket.

Protein interaction with the heme moiety also has a profound effect on its spectral properties. Like all porphyrins, the visible absorption of heme is dominated by transitions from the macrocycle π bonding HOMO orbitals $a_{1u}(\pi)$ and $a_{2u}(\pi)$ to two π antibonding LUMO orbitals $e_g(\pi^*)$, which are degenerate under D_{4h} symmetry. The $Q_{0,0}$ transition absorption band, for which the transition dipoles to these strongly interacting degenerate orbitals nearly cancel, shows spectral splitting and band asymmetry for some hemoproteins,[133-136] suggesting a lifting of the degeneracy of $e_g(\pi^*)$. While it is sometimes suggested that this splitting is due to populations of different protein conformations,[137] optical and resonance Raman studies indicate that $e_g(\pi^*)$ is split through interaction with the asymmetric protein environment[133,136,138] though a Jahn-Teller mechanism.

Similar phenomena have been observed for other metalloporphyrin complexes, primarily Zinc porphyrins suspended in alkane host matrices at cryogenic temperature,[139,140] where the lifting of the $e_g(\pi^*)$ orbital degeneracy is ascribed to a Jahn Teller distortion. For systems with four fold symmetry, this distortion occurs through vibrational coupling along b_{1g} or b_{2g} Jahn Teller active

modes,[140-142] breaking the in-plane symmetry and resulting in two Jahn Teller states associated with shifts along the Jahn Teller active mode in opposite directions. In an asymmetric environment, these degenerate distorted states are split by an energy δ_{JT} (the "Jahn Teller splitting") due to unequal interactions with the environment. [142,143].

Because Zn(II) has no vacancies in the 3d orbitals, Zinc porphyrins (ZnP) excited states cannot relax through charge transfer or energy transfer to the metal orbitals and have very long lived $^3(\pi, \pi^*)$ states in the absence of a triplet quenching species. Zn Porotoporphyrin IX (ZnPPIX) has the same double degeneracy, and thus excited state Jahn Teller instability, as heme, and the long lifetime of ZnPPIX $^3(\pi, \pi^*)$ has been exploited to investigate the impacts of axial ligation and the protein environment on the splitting of $e_g(\pi^*)$. EPR studies of metastable triplet populations of free ZnPPIX and ZnPPIX substituted into hemoproteins reveal significant dependence of an in-plane distortion of the macrocycle on axial ligation, interactions with the protein environment, and porphyrin substituents.[144-146]. These studies observed non-zero values of the zero-flied splitting parameter E, which is a measure of the in plane tetragonal distortion via the splitting of X and Y EPR transitions, while the temperature dependence of the X and Y transition coalescence gave a measure of the δ_{JT} for each system. Zinc proteins, especially Zinc myoglobin (ZnMb) and Zinc cytochrome c (ZnCc), have large values of E and δ_{JT} compared to symmetric four coordinate ZnPs, followed by substituted ZnPs in solution with coordinating ligands (Figure 5.1).

The long lived, highly reducing excited states of Zinc-substituted hemoproteins have also long been used to deduce the kinetic mechanisms of photo-initiated long distance inter-protein electron transfer.

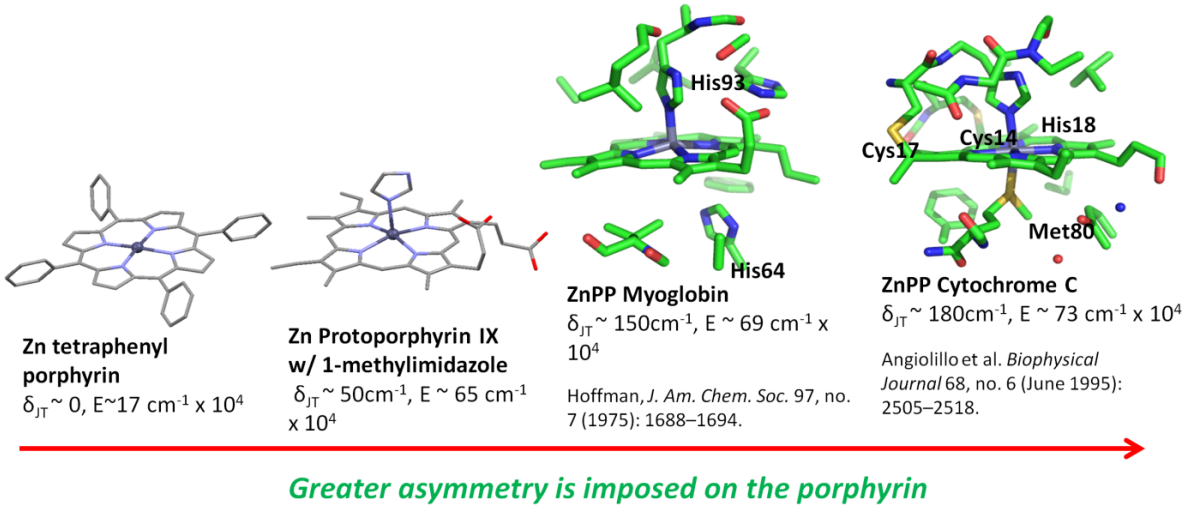

Figure 5.1: Model complexes and Zn hemoproteins studied with EPR measured values of the Jahn Teller splitting, $\boldsymbol{\delta_{JT}}$, between distorted Jahn Teller states as well as E, a measure of the tetragonal distortion.

By exchanging the iron heme in an ET hemoprotein's active site with a Zn porphyrin, ET to a nearby acceptor site can be photo-initiated and protein effects on the ET rate established. Because ET reactivity is in part determined by perturbation of porphyrin structure and electronic structure by the protein itself, and the degree of the Jahn Teller distortion is dependent on the porphyrin environment asymmetry, interactions between the protein environment and this Zn porphyrin excited state reflected by the degree and dynamics of distortion are linked to how hemoproteins effect their enzymatic function through control of ET reactivity.

To assess the excited state structures of Zn tetraphenylporphyrin (ZnTPP), ZnPPIX coordinated to 1-methyimizazole (1-MeIm), ZnMb, and ZnCc, Zn K-edge XANES and EXAFS were measured by both XTA and "steady state" XAS where a metatstable triplet population was generated under constant illumination. ZnMb and ZnCc have different heme pocket makeup and different coordination to the Zn. While ZnMb is five coordinate, the Zn(II) of ZnCc is additionally ligated by an axial cysteine, an interaction which should effect the JT distortion in its excited states. The dynamics of the JT distortion in addition to its structural nature are a critical and so far little studied aspect. Because porphyrin conformation plays such a large role in determining chemical properties, the development of the JT distortion may have transient effects on the ET process for Zn hemoproteins. Because ET itself is a dynamic process, structural dynamics in the active site are reflective of how the protein itself may exert control of physiologically critical ET kinetics.

5.2. Methods

5.2.1. XTA studies of ZnTPP and ZnPPIX with 1-MeIm

Time resolved Zn K-edge XANES and EXAFS were collected for ZnTPP and ZnPPIX at the 11-IDD beamline of the Advanced Photon Source, Argonne National Lab. ZnTPP was measured at 2 mM in toluene and ZnPPIX was measured in basic aqueous solution (pH 9.0) with 10% 1-MeIm. Samples were thoroughly sparged with N_2 to eliminate dissolved oxygen and measured under slightly N2 positive pressure in the sample chamber to maintain a closed oxygen free environment. Both samples were excited with a 527 nm, 5 p sFWHM optical pulse from an Nd-YLF laser (Quantronix). at a 1.2 KHz repetition rate to generate the porphyrin $^1(\pi, \pi,^*)$ state as 527 nm is on the high energy shoulder of the Q-band for both samples. Initial X-ray probe pulse delays were set to 100 ps for ZnTPP and to 50 ps and 500ps for ZmPPIX. Zn K-edges were collected in fluorescence mode with two avalanche photo diodes (ApD) and copper oxide Z-1 filters to reduce counts from elastic scattering of the probe pulse.

5.2.2. Preparation of Zn-substituted Myoglobin

Apomyoglobin was first prepared from lyophilized equine myoglobin (Sigma). 200 mg of the lyophilized protein was dissolved in 100 ml of cold 25 mM potassium phosphate buffer (pH 7.0). The solution was brought to 100 mM in potassium fluoride with a 1 M KF solution. F- coordinates the myoglobin heme Fe and raises the pH necessary to break the heme-protein linkage. While stirring gently on ice and continuously monitoring pH, the pH of the protein solution was brought down to 3.2 with the drop wise addition of cold 100 mM HCl, The now unbound heme was removed from solution with an organic phase extraction. An equal volume of cold 2-butanone was

iteratively added to the protein solution, shook, allowed to separate from the aqueous phase, and removed until the aqueous layer became colorless. The apomyoglobin solution was dialyzed against 10 mM Tris HCL (pH 7) over 24 hours to remove excess butanone.

Substitution of Zn Protoporphyrin IX (Frontier Scientific) into the myoglobin active site was done with minimal light on ice. The protein solution was brought to 100 mM Tris HCl (pH 8.0) and 8 M guanidine chloride, and a 4 fold excess of ZnPPIX dissolved in basic aqueous solution was added. The solution was stirred in the dark for several hours and monitored optically for the broadening of the Zn porphyrin Soret band, which signals incorporation into the protein. The protein solution was dialyzed against 25 mM potassium phosphate buffer (pH 7.0), loaded onto a CM-52 ion exchange column equilibrated with 25 mM acetate buffer, and eluted with a 25 mM acetate, 0 - 500 mM NaCl gradient.

5.2.3. Preparation of Zn-substituted Cytochrome C

To prepare metal free Cyt C, lyophilized quine heart Cyt C (Sigma) was first demetalated. In a fume hood, ten milliliters of 70 % HF in pyridine for every 30 mg of lyophilized Cyt c were added to a small Teflon beaker containing the dry protein. The solution was gently stirred for 20 min with a low nitrogen flow over the surface to evaporate the majority of the HF. The reaction was quenched with of 10 ml of 50 mM ammonium acetate buffer (pH 5.0) and stirring was continued with low nitrogen flow for 20 min. The solution was applied to a short Sephadex G-50 size exclusion column equilibrated with 50 mM acetate buffer (pH 5.0) to remove excess iron and pyridine. Metal free Cyt c was dialyzed (10 kDa MWCO) against 2-3 changes of 50mM acetate buffer over a two day period to remove residual pyridine. The solution was diluted by a factor of

2, loaded onto a CM-52 ion exchange column equilibrated with 25 mM acetate buffer, and eluted with a 25 mM acetate, 0 - 500 mM NaCl gradient.

Following demetalation, Zn was inserted into the metal free Cyt C. The protein was concentrated to a few ml and a 100 fold excess of Zn acetate dissolved in 50 mM, pH 5 acetate buffer was added. The solution was stirred gently at 37 ^{o}C for one hour and the insertion was monitored by observing the rise of a sharp soret peak at 423 nm, and Q-bands at 549 and 584 nm via UV-Vis. Excess zinc was removed with a second Sephadex G-50 size exclusion column and the protein was further purified from any misfolded or aggregated components with a second CM-52 ion exchange column.

5.2.4. Steady state XAS experiments at cryogenic temperature

Zn K-edge XANES and EXAFS of three samples, ZnPPIX + 1-MeIm, ZnMb, and ZnCc were collected at the 12-BM beamline of the Advanced Photon Source, Argonne National Lab. ZnPPIX was acquired from commercial sources (Frontier Scientific) and dissolved to 1 mM in basic aqueous solution containing 30% glycerol and 10% 1-methyl imidazole. Small volumes (~ 500ul) of both metalloprotein samples were prepared to1 mM in Zn for ZnMb and 0.5 mM in Zn for ZnCc in 100 mM potassium phosphate buffer (pH 7.0) containing 30% glyercol to act as a glassing agent. The samples were deoxygenated in an anaerobic chamber (< 10 ppm O_2) and injected into homemade sample holders consisting of a 2 mm by 6 mm oval hole in a 1 mm thick copper disk sealed on both sides with clear mylar tape.

The sample holders were clamped to the cold finger of a He-recycling cryostat to ensure good thermal contact and cooled to about 240 K to freeze the sample into a glass. The cryostat was

evacuated once the samples were solid and cooled to 16 K. The samples were illuminated from the back with the 2 mm focused beam of a 50 W Xe lamp through a special quartz window in the cryostat. The Zn K edge of both the ground state and illuminated sample was collected in fluorescence mode through a mylar window in the cryostat with a 13 element germanium detector. The germanium detector has a long integration time (~seconds) but is energy discriminating. This allows the user to select an energy window to integrate to obtain fluorescence data corresponding to a K emission peak of the element of interest, reducing background from other elements and inelastic scattering from the incident X-ray.

5.2.5. XTA studies of stationary Zn hemoproteins at cryogenic temperature

To probe the structural evolution of the Jahn Teller distortion in ZnMb following a porphyrin-centered excitation and to determine the effect that the protein matrix has on the dynamic process, Zn K-edge XANES and EXAFS were collected at the 11-ID-D beamline at various time delays. ZnMb was prepared and deoxygenated as in the steady state experiments, though at a higher concentration (2 mM in Zn), and loaded and sealed anaerobically in 0.7 mm quartz capillaries.

Capillaries were loaded in a special copper mount attached to the cold-finger of a cryostat adapted to mount on the underside of the existing sample chamber. A copper attachment to the existing cold-finger was designed to protrude through the port in the bottom of the sample chamber normally occupied by the jet catch tube that links the sample chamber to the reservoir and hold sample capillaries vertically. This allowed the capillaries to occupy the same vertical position normally occupied by the liquid jet in conventional XTA experiments. The sample chamber was outfitted with seals on all ports to allow the chamber to be evacuated to 10^{-8} torr via a turbopump

connected to the sample environment through the croystat's existing vacuum system. While under vacuum, the capillaries were cooled to 77 K during the course of data collection. The capillary was vertically translated between each scan to minimize laser and X-ray damage to the stationary sample. ZnMb was excited with a the Nd-YLF 527 nm picosecond optical pulse whch was reduced to at a 20 Hz repetition rate. The X-ray probe pulse was set to an initial time delay of 1 ns with subsequent bunches arriving at 153ns increments measuring in 24 bunch mode.

5.3. Results and Discussion

5.3.1. XTA studies of ZnTPP and ZnPPIX

TRXAS measurements of ZnTPP were carried out to establish a baseline of comparison for 5-coordinate and protein bound porphyrins. Because ZnTPP is a meso-substituted porphyrin, we expected to excite the system from the a_{2u} molecular orbital (HOMO) to the e_g (LUMO). This causes a change in the electron density distribution on the nitrogen atoms that coordinate Zn^{II} and a likely shift in this bond length in addition to the predicted JT in-plane distortion.

There are time-dependent changes in the ZnTPP XANES, especially in the rising edge region surrounding a prominent edge feature at 9.655keV, assigned by polarization dependent XAS studies as Zn 1s→4p_z transition[147,148] (Figure 5.2). These consist of either a slight shift of the peak to higher energy or a general shift of the absorption edge upon excitation, followed by recovery to the ground state spectrum in successive pulses. These can be visualized with absorption difference spectra of this energy region over time (Figure 5.3). The decay of the difference signal at the pre-edge peak energy (9.654keV) is consistent with known decay kinetics of ZnTPP, which has a singlet lifetime of 2.7 ns and a triplet lifetime of 1.2 ms in dilute solutions but is quenched very

rapidly at mM concentration by ground state ZnTPP.[149] We assign the 100ps spectrum to be ^{1}ZnTPP, while following spectrum at 153 ns consists primarily of ^{3}ZnTPP. Interestingly, the XANES difference for the spectrum consisting mostly of ^{1}ZnTPP appears to have a slightly smaller difference amplitude than ^{3}ZnTPP.

TRXAS measurements of ZnPPIX + 10% 1-MeIm in aqueous solution collected sets of scans at laser delays of both at 50 ps and 500 ps to look for signs of geometric relaxation to a distorted state slower than 50 ps but faster than the 153ns to the next probe pulse. Both of these delays are within the 1.8 ns singlet lifetime.[150] For ZnPPIX, the shoulder on the rising edge at 9.668 keV also has mixed $4p_z$ character, though the main $1s \rightarrow 4p_z$ peak is shifted to higher energy and into the high density of transitions higher on the edge due to ligation with 1-MeIm. A close look at the absorption difference spectra at 50 ps, 500 ps, and successive pulses indicates the decay of the most prominent feature of the difference at about 9.67keV (Figure 5.4, Figure 5.5).

This difference signal shares some features with that of ZnTPP in that there is a positive feature just below the peak of the Zn edge, though the negative feature at the 4pz shoulder is much less pronounced. Meanwhile, there is an additional negative feature at the peak of the edge. At 500 ps, the difference signal is similar but smaller in magnitude than that for 50 ps. The difference decays seemingly quite rapidly, though like ^{3}ZnTPP, ^{3}ZnPPIX is very susceptible to concentration dependent quenching.[150] Changes in the EXAFS for ZnTPP and ZnPPIX on excitation are quite small in magnitude, especially compared to the XANES difference signal for ZnTPP. Fits of the EXAFS were attempted for the ground state and time delays corresponding to the singlet state (100 ps/50ps) and triplet state (153ns) for both samples, but changes in the distances between Zn and

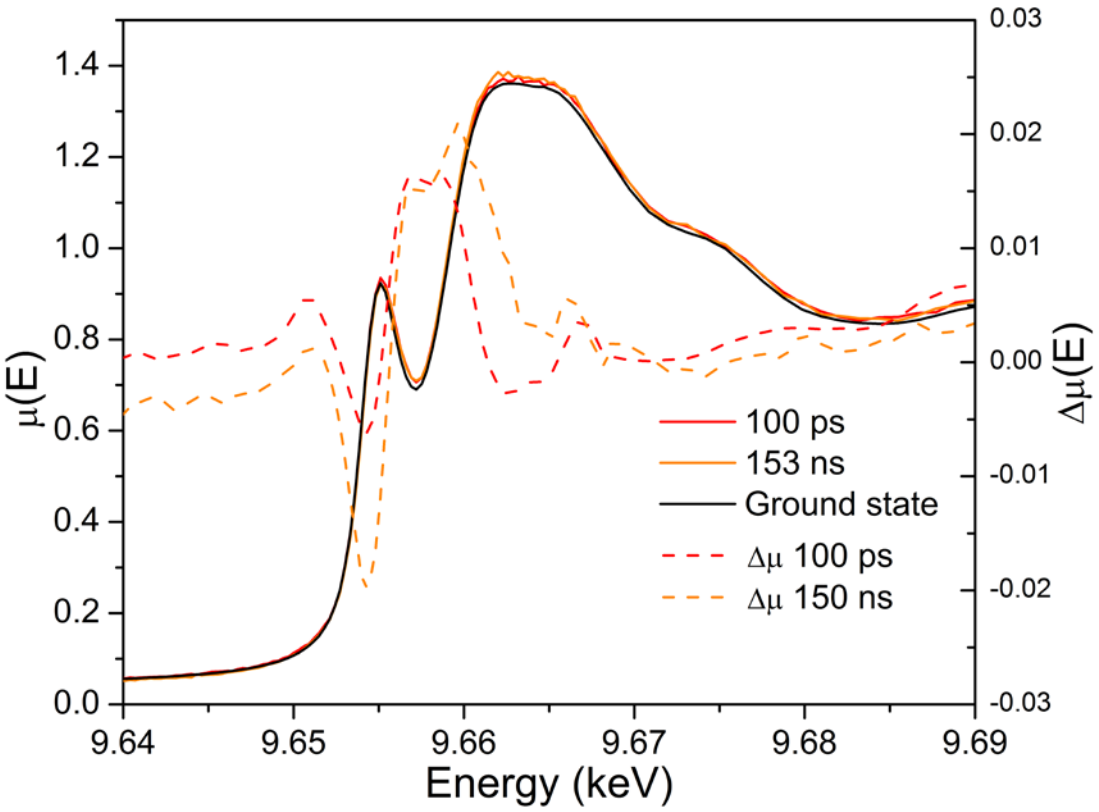

Figure 5.2: Zn K-edge XANES of ground state ZnTPP and at 100 ps and 153 ns after excitation. Difference spectra for both time delays are pictured (right axis).

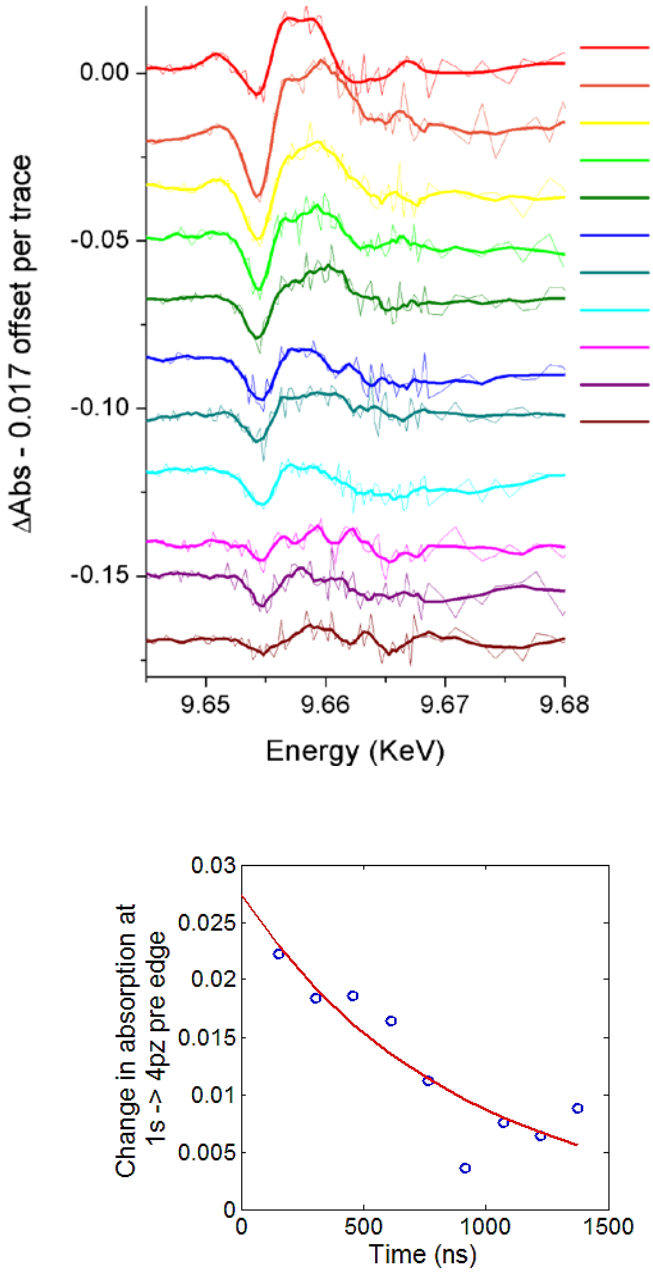

Figure 5.3: (Upper) Zn K-edge difference spectra for ZnTPP 100 ps after excitation and at subsequent 150 ns intervals, shown raw and 10 point smoothed, offset for clarity. (Lower) The change in the magnitude of the difference at its positive peak, 9.659 keV.

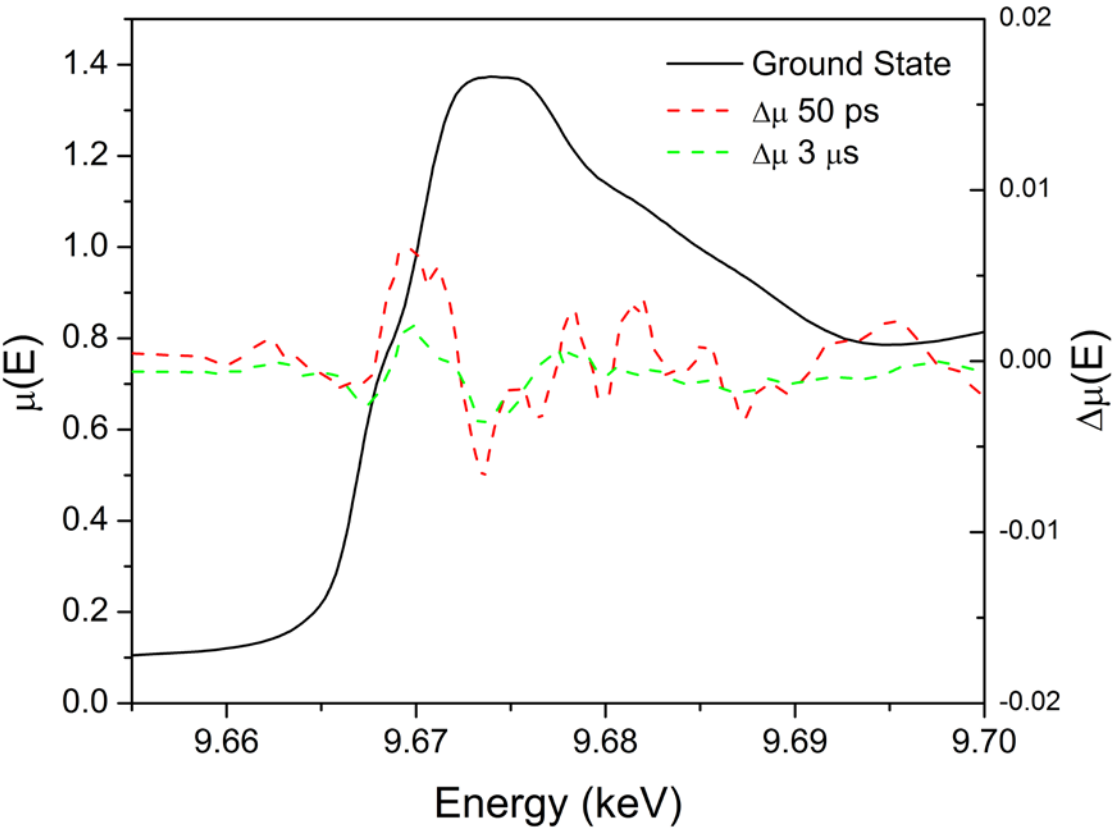

Figure 5.4: Zn K-edge XANES of ground state ZnPPIX + 10% 1-MeIm and at 50 ps and 500 ps after excitation. Difference spectra for both time delays are pictured (right axis)

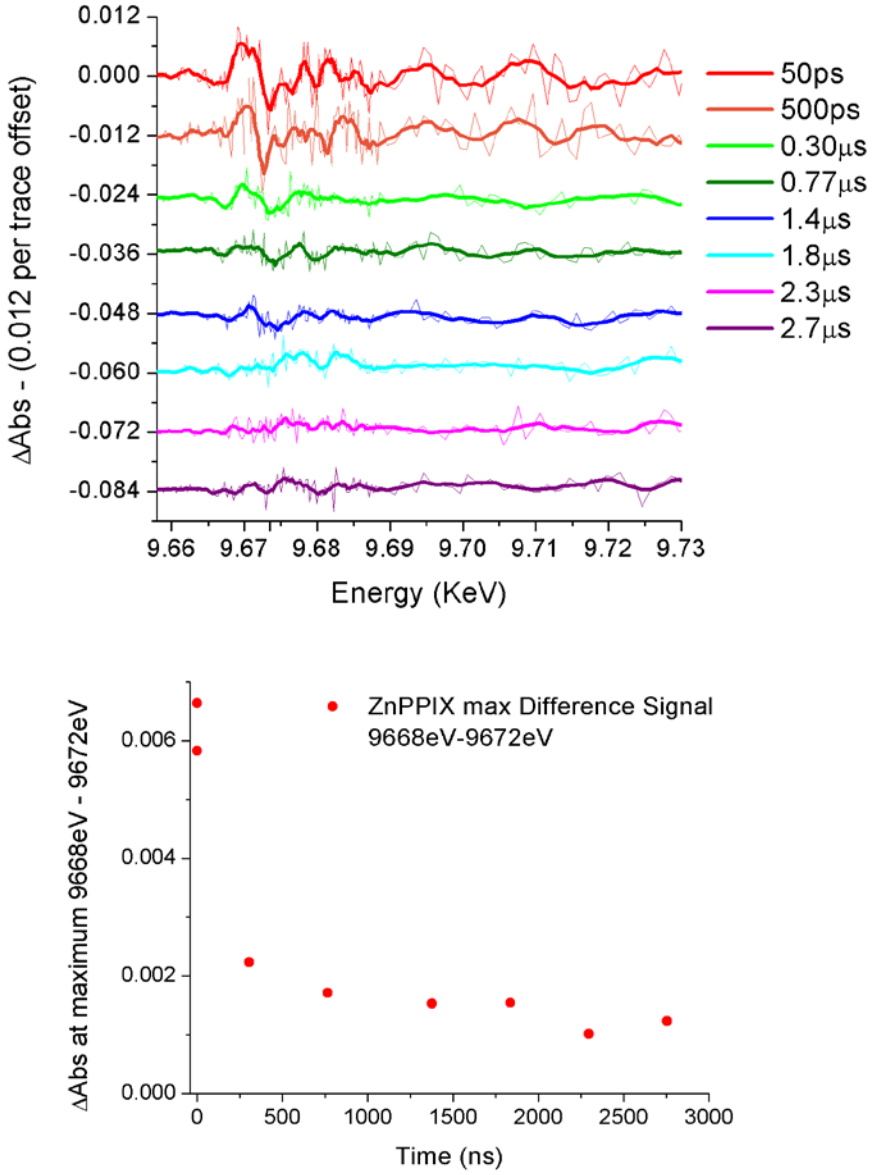

Figure 5.5: (Upper) Zn K-edge difference spectra for ZnPPIX in 10% 1-MeIm basic aqueous solution 50 ps, 500 ps and at subsequent 150 ns intervals after excitation, shown raw and 10 point smoothed, offset for clarity. (Lower) The decay of the magnitude of the integrated difference between 9668 eV and 9672 eV with time.

porphyrin or imidazole atoms were consistently below the precision of the method to determine meaningfully given the quality of the time resolved data (~0.02 – 0.03Å).

Therefore, the R-space plots (Figure 5.6) are discussed qualitatively. For ^{1}ZnTPP and ^{3}ZnTPP, small shifts in amplitude and position in the second and third shells, which correspond mostly to C_{α} and C_{meso}/C_{β} backscattering to the Zn respectively, are apparent relative to the ground state. A shift in the first shell peak, which is attributable to the Zn-N_p backscattering, is not apparent. There is a shift to shorter Zn-N bond length in the ^{1}ZnPPIX and ^{2}ZnPPIX R-space plot while the second shell and third shells exhibit small shifts to longer Zn-C_{α} and C_{meso}/C_{β} distances relative to the ground state, especially the third shell in triplet state. This suggests that some Zn-N bonds are shrinking while others are expanding, most likely either through an in-plane b_{1g} distortion or due to Fe-N_p and Fe-N_{His} bond length changes of opposite sign.

If we interpret the ZnPPIX XANES difference as a shift of the 4pz character shoulder to higher energy, Fe-N_{His} shrinkage and Fe-Np expansion is a good candidate in the latter case. That minimal changes observed in ZnTPP is in line with its relatively meager values of E and δ_{JT}. Any distortion present at room temperature may be broadened to the point of being undetectable by interconversion between Jahn Teller states. However, while a reduction in amplitude for some of the R-space peaks at 100 ps suggests broadening of the EXAFS, this is not the case for the triplet at 153 ns. It's also unclear how the shape of the ZnTPP XANES difference should be interpreted. While a shift of the edge to higher energy may indicate Zn-N_p bond contraction, that is not supported by the EXAFS and contradicts excited state geometries calculated by DFT, which invariably show expansion of the average Fe-Np bond lengths.[151 152]. ZnPPIX's more significant excited state changes in the EXAFS may reflect its higher value of E.

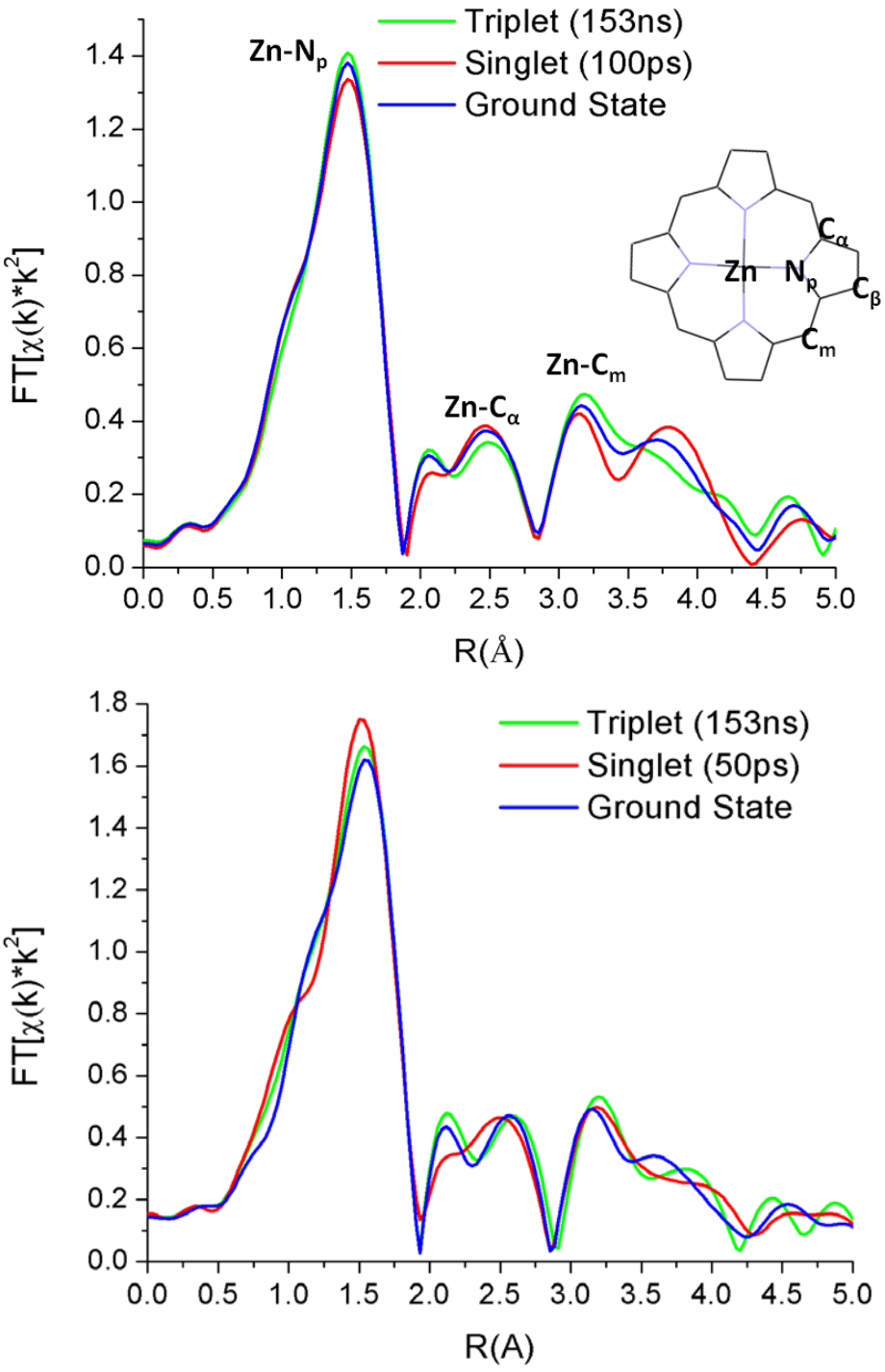

Figure 5.6: Fourier transforms (R plots) of the k^2 weighted EXAFS signal for ZnTPP and ZnPPIX.

5.3.2. Steady state XAS experiments at cryogenic temperature

Steady state Zn K-edges, where the X-ray fluorescence signal is temporally integrated, collected for continuously illuminated ZnPPIX, ZnMb and ZnCc at cryogenic temperature are expected to reflect a metastable population of excited triplet state with a single static JT distorted conformer. As seen in previous EPR studies,[144] porphyrin substitution by the vinyl groups of protoporphyrin and an axial and π-bonding ligands stabilizes one JT state with respect to the other for ZnPPIX + 1-MeIm and low ambient temperature (16K) ensures that only one JT state is populated as the JT splitting for this system is 50cm^{-1} and kT at 16K is 11cm^{-1}.[12] ZnMb (δ_{JT} = 150 cm^{-1}) and ZnCc (δ_{JT} = 180 cm^{-1}) are additionally split by the protein environment and should also have a single populated state. Implementing these low temperature sample conditions has the additional effect of greatly reducing radiation damage to the sample, yielding clearer, higher quality oscillatory features in the data at high k, and allowing the use of a much smaller sample volume compared to a liquid jet method of sample delivery, which would be impossible for preparations of ZnMb and ZnCc of this scale.

In this case excitation is accomplished with a broadband continuous light source with significant output in the Soret region ($S_0 \rightarrow S_2$) in addition to the Q-band, as opposed to a laser pulse. The decay from $S_2 \rightarrow S_1$ is very rapid and intersystem crossing to the triplet is many orders of magnitude faster than the triplet decay in all samples, leading to negligible contribution from either singlet state to the XAS. The illumination conditions are very similar to those used by the EPR studies that characterized the relative magnitudes of tetragonal distortion in this series of samples, and they are expected to produce high yields of the metastable triplet population for each. The Zn proteins have similar triplet lifetimes at room temperature and cryogenic temperature (13

ms for ZnMb[150] and 11 ms for ZnCc[153] at 77 K), but the lifetime of ^{3}ZnPPIX increases to 18 ms.[145]

While the magnitude of the steady state XANES difference in ZnPPIX is significantly larger than in the time resolved experiment, features of the difference are quite different. The steady state difference is dominated by a broad negative feature that indicates the depression or broadening of the entire peak of the Zn K-edge from 9662 eV to 9675 eV (Figure 5.7). A small negative feature appears at the shoulder of the edge at 9660 eV.

The XTA data for ZnPPIX show small negative features both at this shoulder and at the edge peak at 50 ps and 500ps, but the positive feature just below the peak of the edge is absent, possibly because it is overwhelmed by this broad depression of the edge peak. The XANES difference is similar for ZnCc, thought the negative feature is less intense and is shifted to slightly higher energy, while the ZnMb XANES difference appears to consist only of the broad reduction of the edge peak.

The broad depression of the edge peak is difficult to rationalize in terms static structural changes to the porphyrin. Many factors influence the peak height, and the possible justification of a decrease in coordination number can be ruled out based on the lack of positive features at the 9660 eV edge shoulder, which would be enhanced by any dissociation of axial ligands. Shifts in scattering resonances or electronic transitions due to bond length changes are unlikely to manifest as such a broad feature. The simplest explanation may be that heat deposited by the Xe lamp induces thermal broadening in the edge peak, which can be assessed by looking at the disorder of the scattering paths in the EXAFS regions.

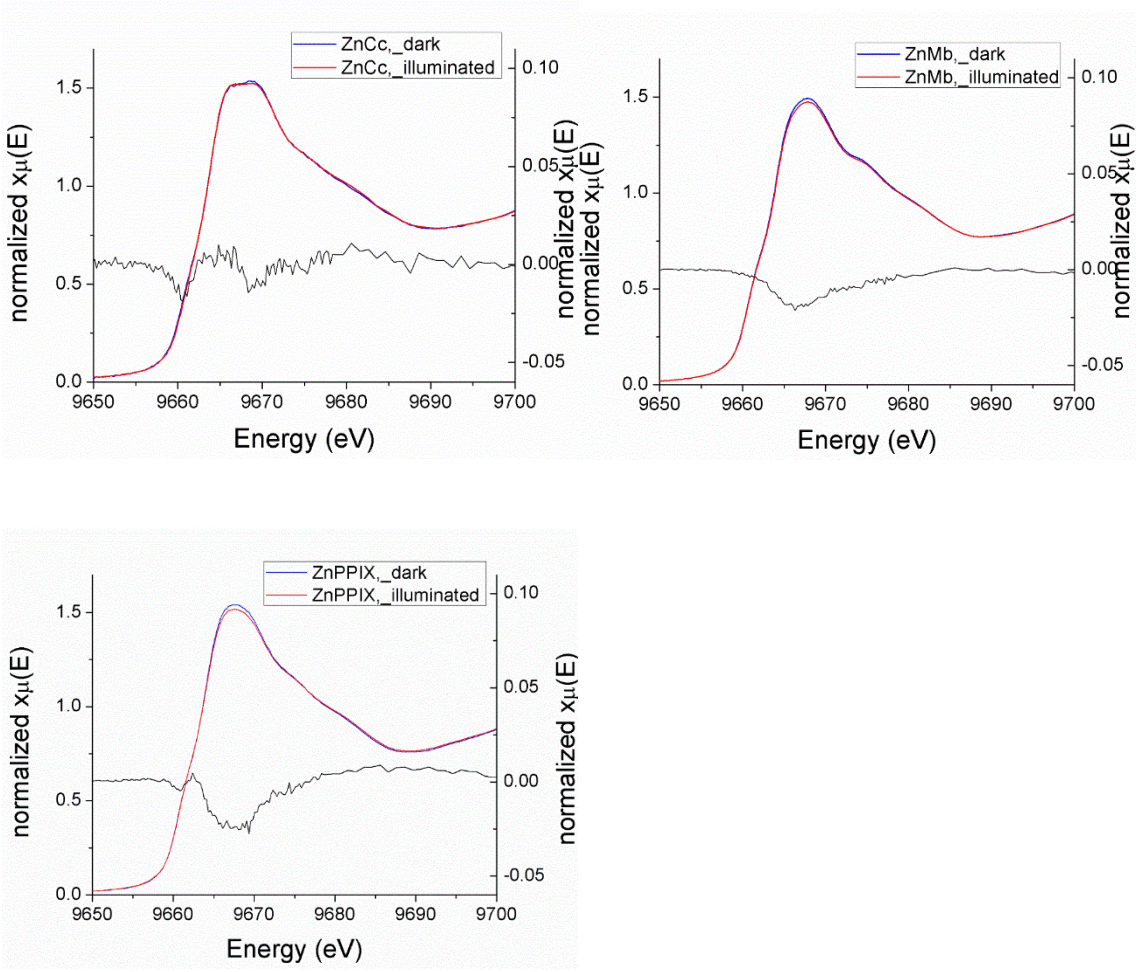

Figure 5.7: Zn K-edge XANES for ZnPPIX in 10% 1-MeIm, ZnMb, and ZnCc at cryogenic temperature (16 K), both dark and continuously illuminated with the focused output of a 50 W Xe lamp. Lamp on – Lamp off difference spectra are shown for each sample (right axis).

The Fourier Transform (FT) of EXAFS oscillations for dark and illuminated ZnPPIX (Figure 5.8) show very little difference on excitation, although a slight damping of the EXAFS signal may indicate a small contribution from broadening. ZnMb (Figure 5.10) and ZnCc (Figure 5.9) EXAFS show small shifts in several FT peaks on illumination and were fit to determine the general nature of the structural change. A small window in k was used to perform the Fourier transform (k = 1.5 – 10) for both samples due to some apparent oscillatory artifacts at higher k in the ZnMb EXAFS.

Both fits used available structural data to calculate EXAFS scattering paths[154 155]according to the EXAFS equation and results are shown in Tables 5.1- 5.4. The bond lengths obtained by the fits to dark ZnMb and ZnCc are in good agreement with the crystallographic data with the exception of Zn-N_h distance for ZnMb and the Zn-S distance for ZnCc, which fit to bond lengths 0.1 Å and 0.15 Å longer than the model respectively.

Fits for both illuminated samples describe a similar structural change; a slight expansion of the Zn-N_p distances accompanied by a reduction in the axial bond lengths. Attempts to fit the Zn-N_p and Zn-$C_{\alpha p}$ distances with two separate bond lengths to reflect bond alternation expected for a b_{1g} (rectangular) in-plane distortion did not significantly improve the fits. The rectangular distortion is typically the lowest energy distorted state observed in geometry optimizations of symmetrical four coordinate ZnPs. [152,156] Debye-waller factors, which indicate the level of disorder in the absorber/scatterer distance, are similar or larger for all scattering paths in the fits to illuminated spectra compared to dark spectra, indicating a higher degree of structural disorder on illumination. This is especially true of ZnMb and may explain the changes in the edge peak as the result of .this broadening of the conformational distribution.

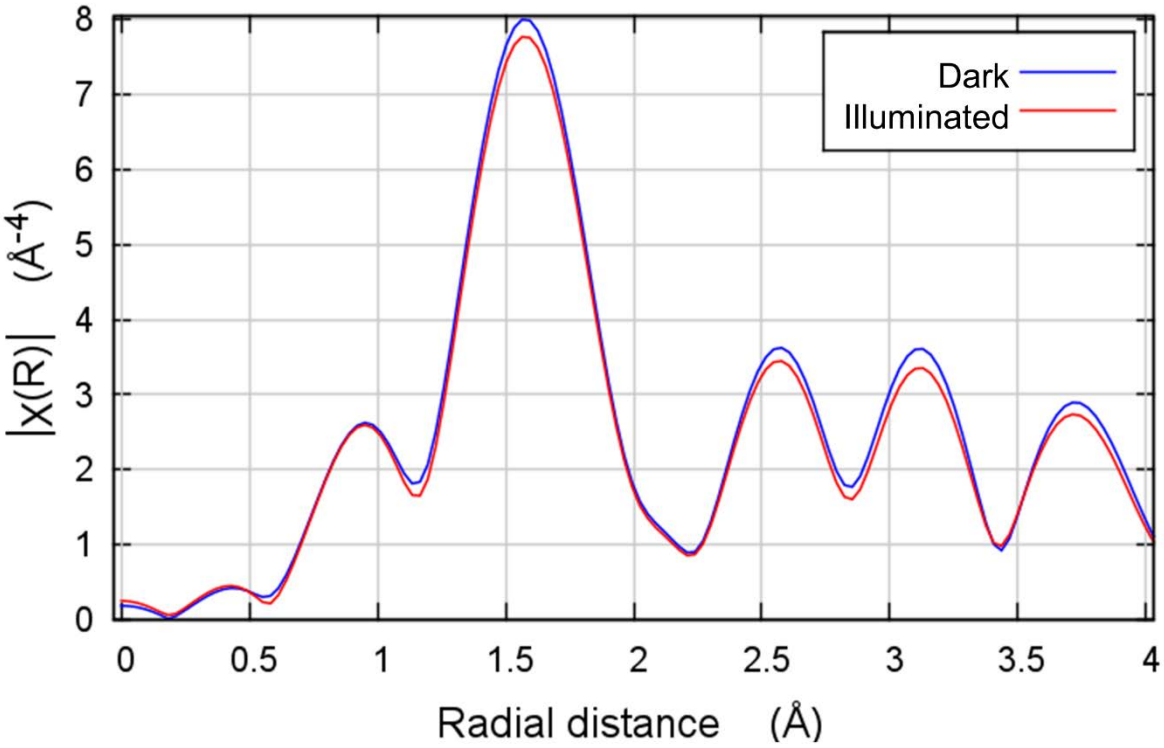

Figure 5.8: R-space plots of ZnPPIX in 10% 1-MeIm, with and without Xe lamp illumination.

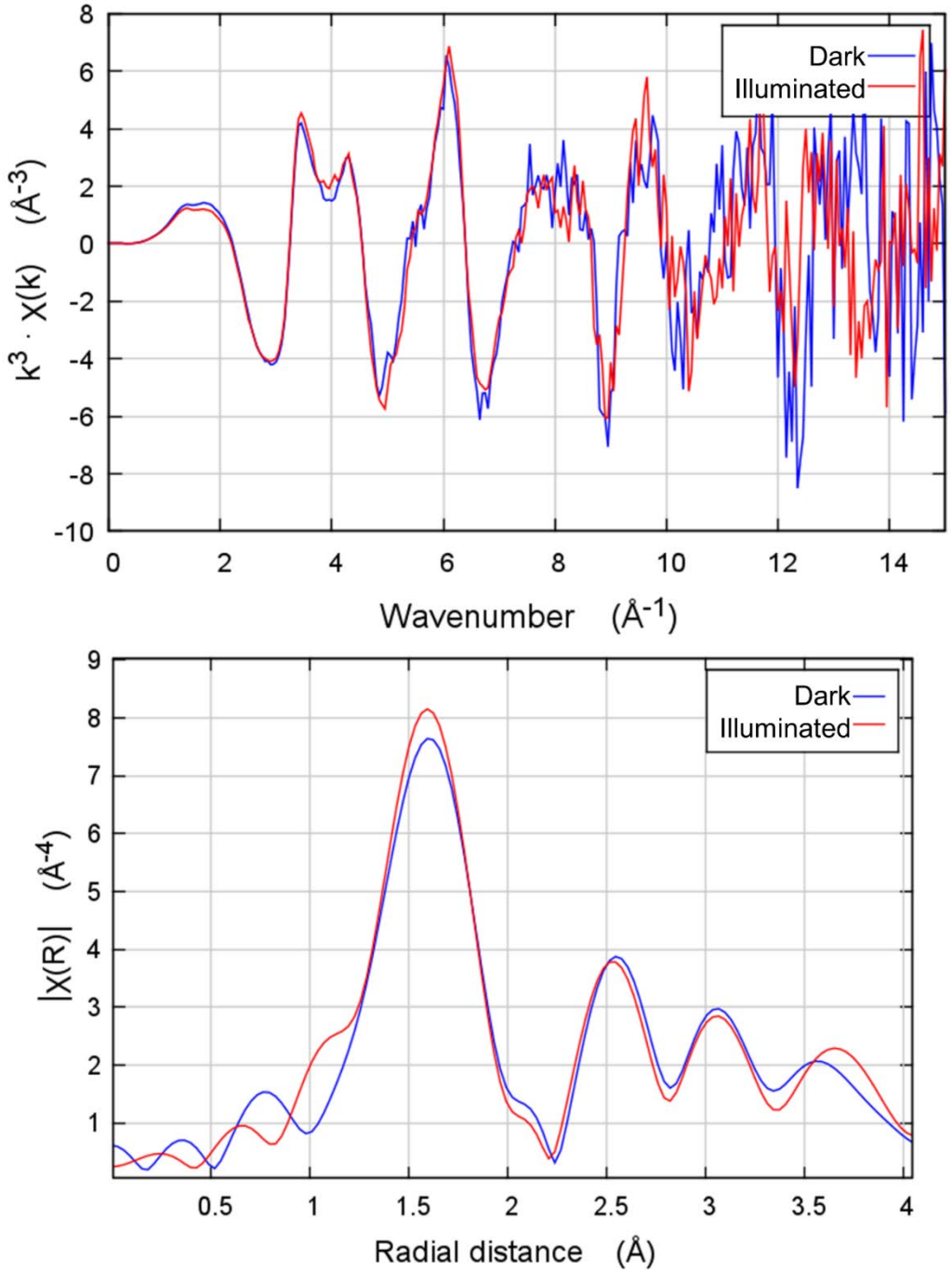

Figure 5.9: k-space spectra (above) and R-space plots of ZnCc, with and without Xe lamp illumination.

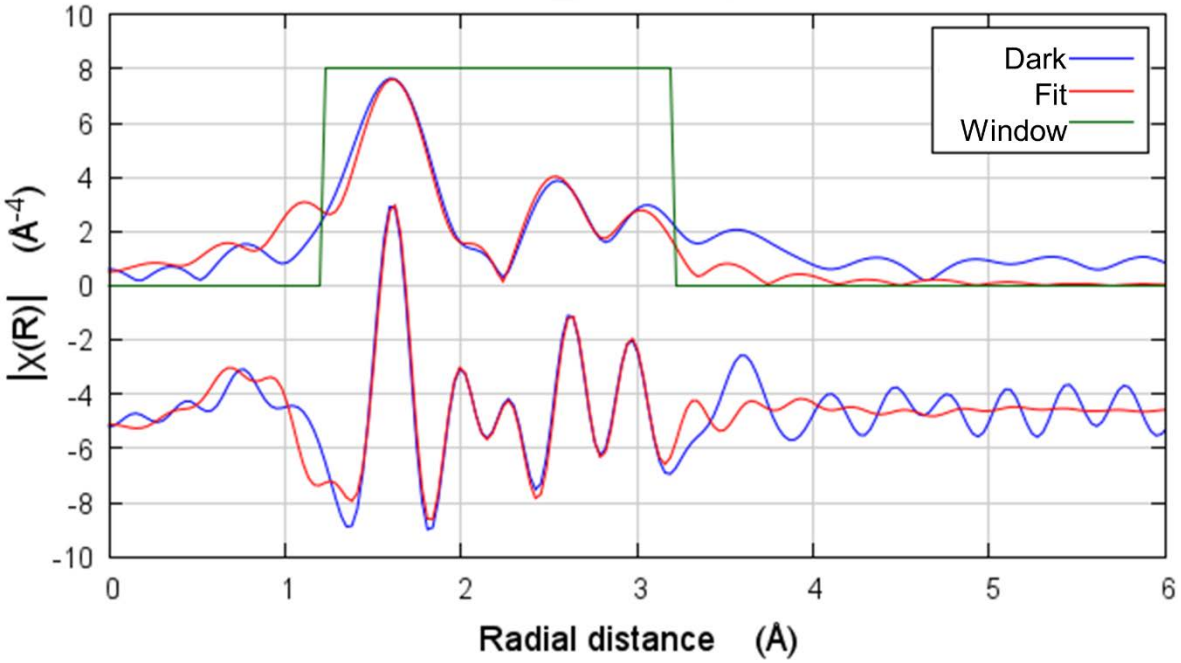

Figure 5.10: R-space (above) and imaginary R-space (below) plots of dark ZnCc with fits within the specified window in R.

Table 5.1: Fitted parameters for dark ZnCc.

Path	**S_0^2**	**E^0**	**R_{eff}**	**σ^2**
N_p	0.8	2.10	2.07	0.0010
N_h			2.303	0.0005
S			2.4	0.0010
$C_{\alpha p}$			3.1	0.0014
$C_{\alpha h}$			3.298	0.0005
C_m			3.456	0.0013

Slightly larger Debye Waller factors for the Zn-N_p scattering paths in both illuminated samples may suggest several similar distances are contained in the envelope of this scattering path, although the effect is too small to account for the degree of bond alternation reported by theoretical modeling of Zn porphyrin triplet states, which usually cite the bond length alternating by about 0.03 Å.[152]

While alternation is not observed, the expansion of the average Zn-N_p distance is consistent with theoretical studies. Because histidine is a π-bonding ligand, the reduction of the Zn-N_h bond may also serve to partly lift the in-plane degeneracy through mixing with one of the d_π orbitals of Zn. A similar role may be served by methionine, as the Zn-S bond has also been suggested to possess π-bonding character.[157]

Another interpretation of the lack of apparent bond alternation implicates interaction between the porphyrin and protein pocket to affect out-of-plane distortion. Protein matrices have a profound influence on heme conformation, in particular to induce out-of-plane distortions that are conserved across proteins with similar physiological function.[18,131,158,159] While coupling to a single out-of-plane mode alone will not break the in-plane symmetry, these distortions in proteins are often the sum of distortions in several modes and can contain lower symmetry components that do. Furthermore, the Jahn Teller instability of the excited state may make it more susceptible to nonplanar distortion, triggering nonplanar distortion when an in-plane distortion brings the porphyrin into closer contact with the surrounding protein. Hemoproteins such as cytochrome c that stabilize nonplanar conformational state would naturally stabilize a distortion triggered in this way.

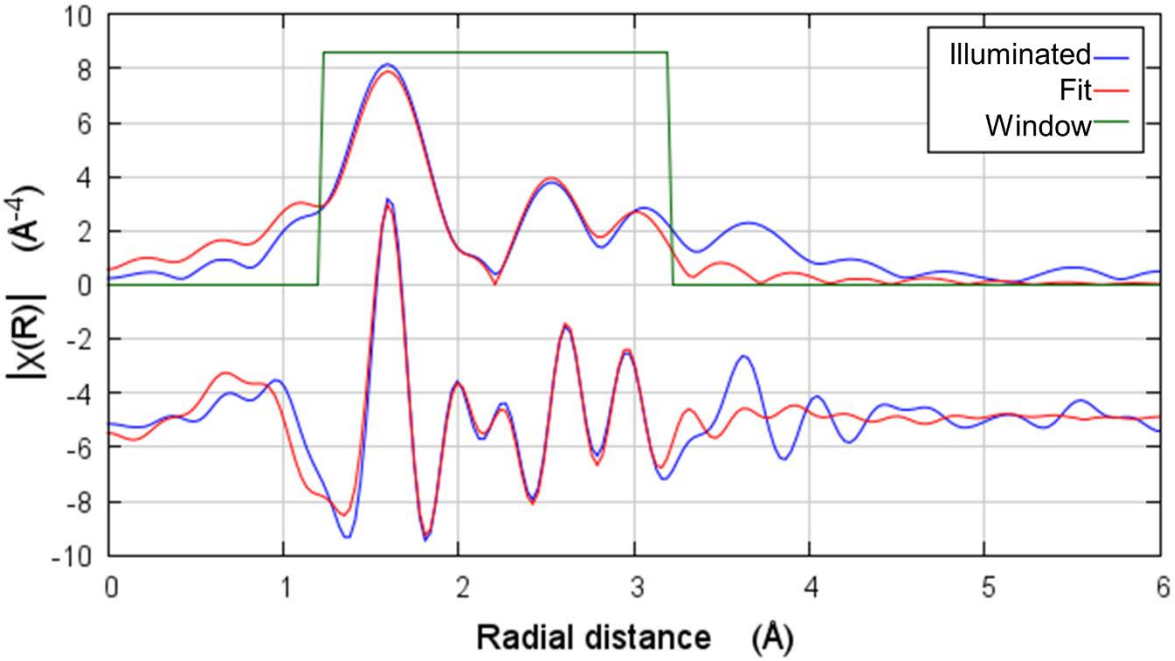

Figure 5.11: R-space (above) and imaginary R-space (below) plots of illuminated ZnCc with fits within the specified window in R.

Table 5.2: Fitted parameters for illuminated ZnCc.

Path	**S_0^2**	**E^0**	**R_{eff}**	**ΔGS**	**σ^2**
N_p	0.83	2.10	2.093	0.023	0.0027
N_h			2.183	-0.12	0.0002
S			2.32	-0.08	0.0003
$C_{\alpha p}$			3.123	0.023	0.0027
$C_{\alpha h}$			3.178	-0.12	0.0002
C_m			3.453	-0.003	0.0020

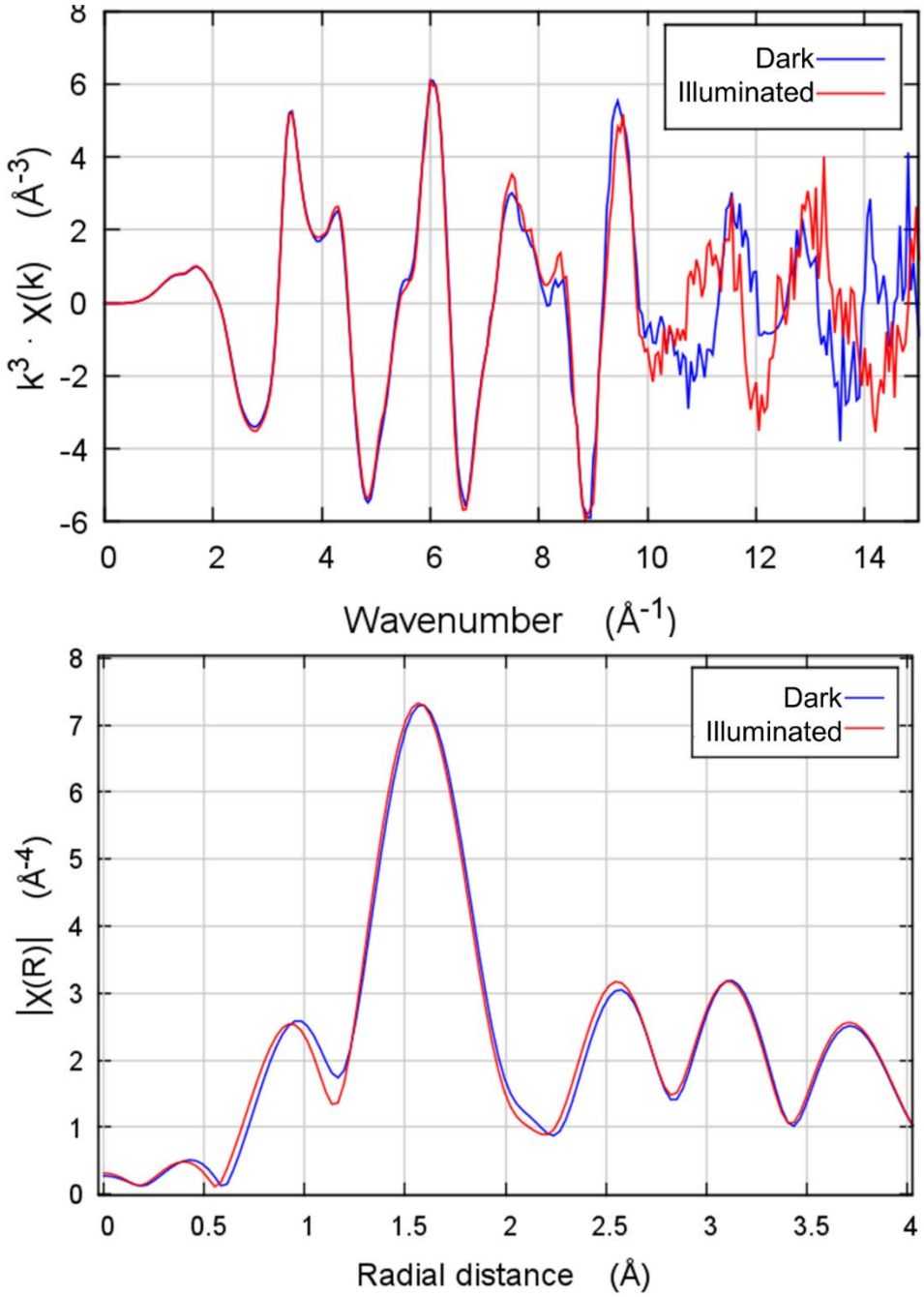

Figure 5.12: k-space spectra (above) and R-space plots of ZnMb, with and without Xe lamp illumination.

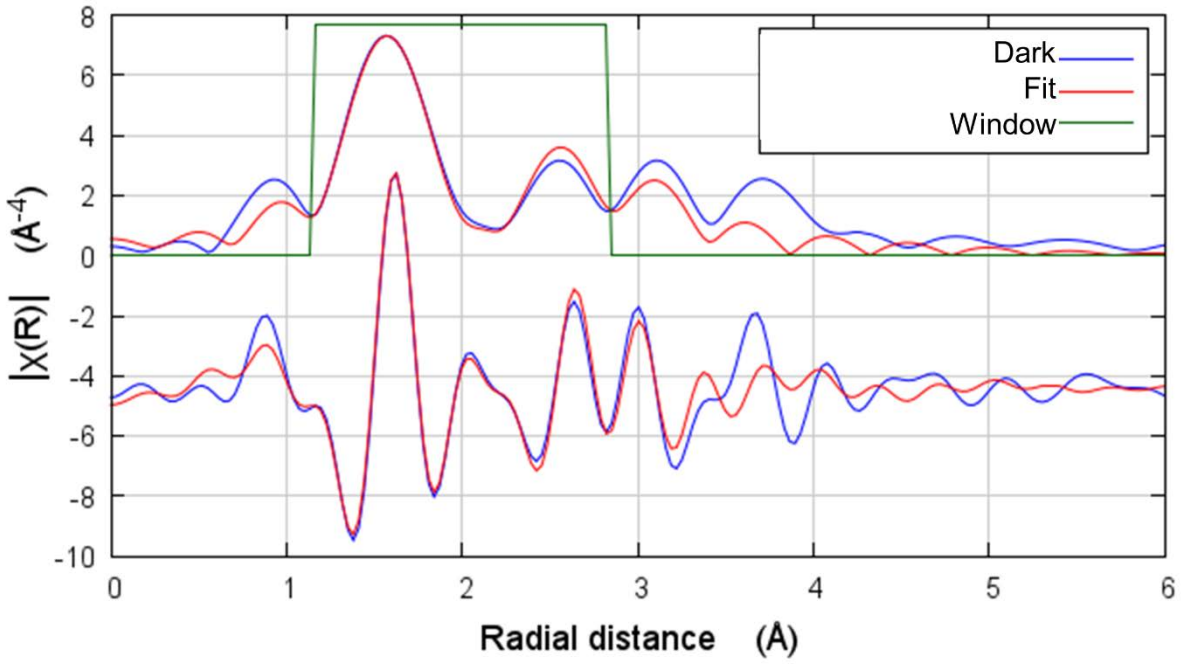

Figure 5.13: R-space (above) and imaginary R-space (below) plots of dark ZnMb with fits within the specified window in R.

Table 5.3: Fitted parameters for dark ZnMb.

Path	**S_0^2**	**E^0**	**R_{eff}**	**σ^2**
N_p	0.97	5.78	2.116	0.0025
N_h			2.038	0.0001
$C_{\alpha p}$			3.062	0.0025
$C_{\alpha h}$			3.108	0.0001
C_m			3.401	0.0001

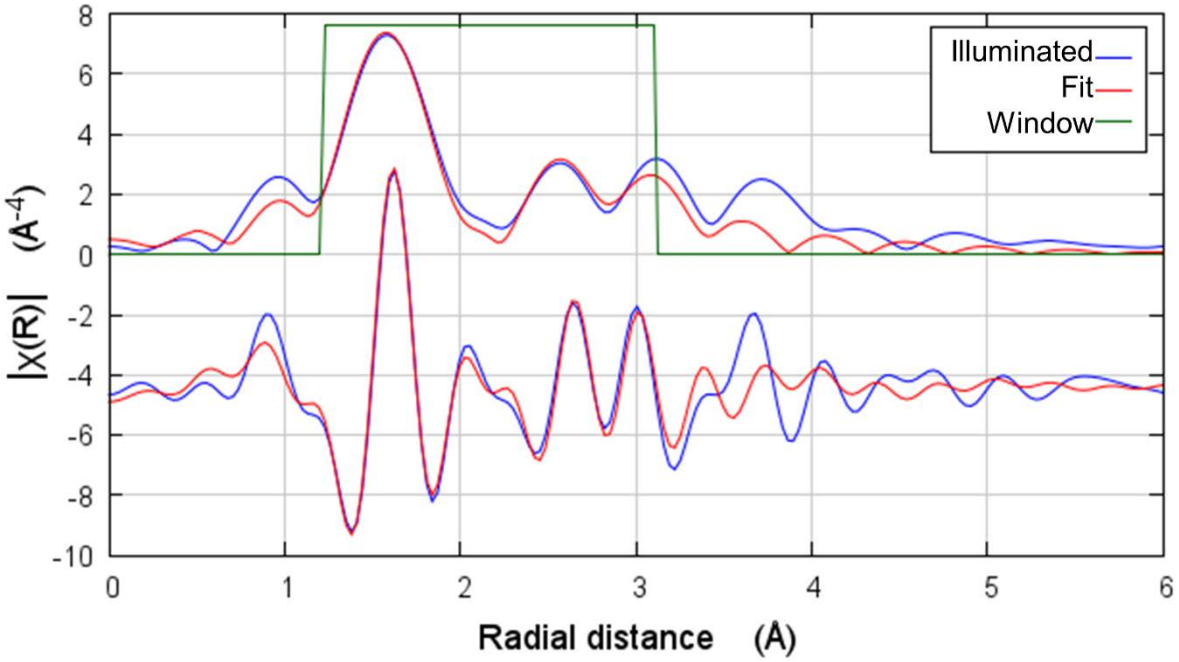

Figure 5.14: R-space (above) and imaginary R-space (below) plots of illuminated ZnMb with fits within the specified window in R.

Table 5.4: Fitted parameters for dark ZnMb.

Path	S_0^2	E^0	$\mathbf{R_{eff}}$	ΔGS	σ^2
N_p	1.05	5.78	2.136	0.02	0.0031
N_h			1.938	-0.1	0.0088
$C_{\alpha p}$			3.082	0.02	0.0031
$C_{\alpha h}$			3.008	-0.1	0.0088
C_m			3.427	0.026	0.0001

5.3.3. XTA studies of stationary Zn hemoproteins at cryogenic temperature

Time resolved measurements on stationary samples at low temperature were also attempted for Zn myoglobin. Because the sample does not circulate and the triplet lifetime of ZnMb is quite long (13 ms at 77 K) the repetition rate was reduced from 1.2 kHz to 20 Hz, which not only impacted the data quality compared to a standard XTA experiment due to reduced statistics, but led to poorer quality pulse-by-pulse fitting. The reduced rep rate increases the time required to acquire dark and reference fits (normally about four minutes at 1.2 kHz) and the number of orbits used in this process must necessarily be reduced. While our strategy to integrate a large number of scans allowed us to acquire acceptable XANES at 1 ns, the high level of noise makes EXAFS analysis of a single bunch impossible.

The XANES difference signal at 1 ns (Figure 5.15) is quite different than the singlet timescale XANES differences for ZnPPIX, and consists of the reduction of absorption between the shoulder and the edge peak as the higher energy part of the edge peak becomes more intense. Integrating all bunches to 50 μs provides greater statistics to our measurement of the ^{3}ZnMb difference and is acceptable based on the long lifetime of ^{3}ZnMb. In spite of this, the difference spectrum for ^{3}ZnMb (Figure 5.15) has quite low S/N due to the small magnitude of the difference (~0.3 % of the total signal). This difference bears some resemblance to the weak, broad, positive features that appear by 1.8 μs in the ZnPPIX difference signals. In the absence of EXAFS, a clear comparison with the other systems studied, or additional theory to model the XANES, these XANES features are very difficult to interpret and strategies to improve our approach are discussed below.

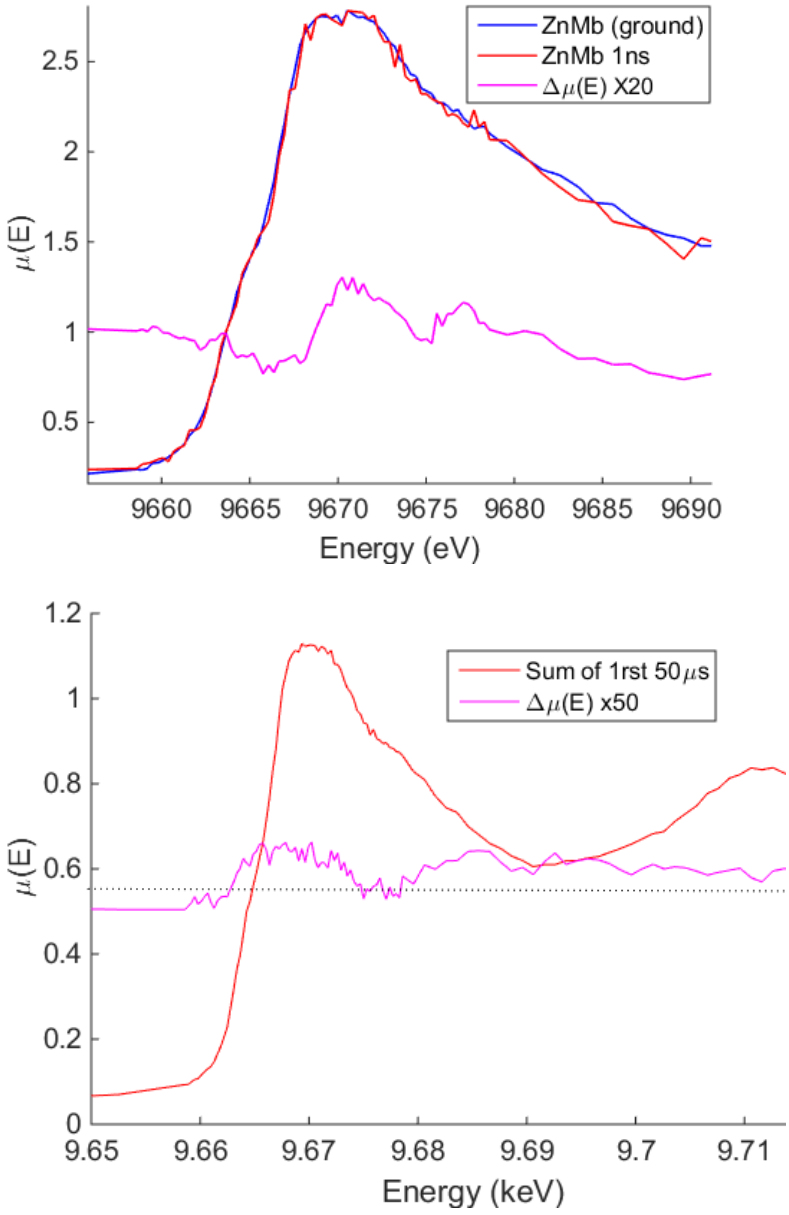

Figure 5.15: (Above) Zn-Kedge XANES for ZnMb in the ground state and at 1 ns following excitation with the difference signal (x20 and offset for clarity). (Below) The sum of all bunches within 50 μs of excitation and the difference signal with respect to the ground state (x50, offset for clarity).

5.4. Summary

Time resolved and steady state XAFS has been measured to characterize the structural dynamics and static distortions in ZnPs and Zn hemoproteins. But many aspects of the XTA and steady state data are currently unexplained. In general, structural changes in each ZnP system are very small in magnitude as measured by EXAFS and do not reflect expected in-plane symmetry breaking distortions. This may be reflective of the genuinely small effect of the Jahn Teller distortion on excited state geometry, or of less than optimal experimental sensitivity. Nevertheless, small structural changes involving the expansion of the porphyrin and the shrinkage of the Fe-Histidine (or 1-MeIm) bond in the steady state data at cryogenic temperature are consistent for the triplet populations of ZnMb and ZnCc, and may be reflected in the ZnPPIX XTA EXAFS. Excitation appears to have a much more profound effect on the ZnP excited state XANES. If the structural changes in the excited states mostly manifest as out-of-plane distortions, it's possible XANES could be much more sensitive to those changes since the scattering component of XANES mostly consists of multiple scattering, which is sensitive to the angle between the absorber and its neighboring atoms in addition to the distance. EXAFS is dominated by single scattering events and lacks that sensitivity. However, XANES differences are challenging to interpret in the absence of 1) a more detailed picture of the ZnP electronic structure on excitation 2) a structural model for the excited state, and 3) a method to quantitatively relate changes XANES features to specific structural distortions. We are currently in the process of completing electronic structure calculations and geometry optimizations for the ground, singlet, and triplet states of each system described by this work. Zn hemoproteins are being modeled within a rigid cage of all amino acids within 8 Å of the porphyrin according to available structure data. This will allow us to model both

electronic and geometric contributions to the excited state XANES. XAS transitions to bound states for the excited states will be calculated using a linear-response TDDFT method recently developed by Mosquera and Schatz[160] to calculate sequential double excitations. Given a geometry for the singlet and triplet excited states, the scattering component of the XANES can be modeled with any of the available tools that implement full multiple scattering theory, such as the FEFF or μXAN packages.

References

(1) Blankenship, R. E. *Molecular Mechanisms of Photosynthesis*; Balckwell Science: Oxford, 2002.

(2) Gust, D.; Moore, T. A.; Moore, A. L. *Acc. Chem. Res.* **2001**, *34*, 40.

(3) Frauenfelder, H.; McMahon, B. H.; Fenimore, P. W. *Proc. Nat. Acad. Sci.* **2003**, *100*, 8615.

(4) Rosenthal, J.; Bachman J; Dempsey J. L.; Esswein A. J.; Gray T. G.; Hodgkiss J. M.; Manke D. R.; Luckett T. D.; Pistorio B. J.; Veige A. S.; G., N. D. *Coord. Chem. Rev.* **2005**, *249*, 1316.

(5) Graham, D. J.; Nocera, D. G. *Organometallics.* **2014**, *33*, 4994.

(6) Yang, J. Y.; Nocera, D. G. *J. Am. Chem. Soc.* **2007**, *129*, 8192.

(7) Holten, D.; Bocian, D. F.; Lindsey, J. S. *Acc. Chem. Res.* **2002**, *35*, 57.

(8) Andersson, J.; Puntoriero, F.; Serroni, S.; Yartsev, A.; Pascher, T.; Polivka, T.; Campagna, S.; Sundstrom, V. *Chem. Phys. Lett.* **2004**, *386*, 336.

(9) Benko, G.; Kallioinen, J.; Korppi-Tommola, J. E. I.; Yartsev, A. P.; Sundstrom, V. *J. Am. Chem. Soc.* **2002**, *124*, 489.

(10) Diamantis, P.; Gonthier, J. F.; Tavernelli, I.; Rothlisberger, U. *J. Phys. Chem. B.* **2014**, *118*, 3950.

(11) Henry, W.; Coates, C. G.; Brady, C.; Ronayne, K. L.; Matousek, P.; Towrie, M.; Botchway, S. W.; Parker, A. W.; Vos, J. G.; Browne, W. R.; McGarvey, J. J. *J. Phys. Chem. A.* **2008**, *112*, 4537.

(12) Shaw, G. B.; Styers-Barnett, D. J.; Gannon, E. Z.; Granger, J. C.; Papanikolas, J. M. *J. Phys. Chem. A.* **2004**, *108*, 4998.

(13) Yoon, S.; Kukura, P.; Stuart, C. M.; Mathies, R. A. *Mol. Phys.* **2006**, *104*, 1275.

(14) Chen, L. X.; Zhang, X.; Wasinger, E. C.; Attenkofer, K.; Jennings, G.; Muresan, A.; Lindsey Jonathan, S. *J. Am. Chem. Soc.* **2007**, *129*, 9616.

(15) *The Porphyrin Handbook*; Academic Press: New York, 1999.

(16) Huang, Y.; Marden, M. C.; Lambry, J. C.; Fontaine-Aupart, M. P.; Pansu, R.; Martin, J. L.; Poyart, C. *J. Am. Chem. Soc.* **1991**, *113*, 9141.

(17) Patra, R.; Chaudhary, A.; Ghosh, S. K.; Rath, S. P. *Inorg. Chem.* **2010**, *49*, 2057.

(18) Jentzen, W.; Ma, J.-G.; Shelnutt, J. A. *Biophys. J.* **1998**, *74*, 753.

(19) Ye, X.; Yu, A.; Georgiev, G. Y.; Gruia, F.; Ionascu, D.; Cao, W.; Sage, J. T.; Champion, P. M. *J. Am. Chem. Soc.* **2005**, *127*, 5854.

(20) Chen, L. X.; Zhang, X.; Shelby, M. L. *Chem. Sci.* **2014**, *5*, 4136.

(21) Chen, L. X.; Zhang, X. Y. *J. Phys. Chem. Lett.* **2013**, *4*, 4000.

(22) Dell'Angela, M.; Anniyev, T.; Beye, M.; Coffee, R.; Fohlisch, A.; Gladh, J.; Katayama, T.; Kaya, S.; Krupin, O.; LaRue, J.; Mogelhoj, A.; Nordlund, D.; Norskov, J. K.; Oberg, H.; Ogasawara, H.; Ostrom, H.; Pettersson, L. G. M.; Schlotter, W. F.; Sellberg, J. A.; Sorgenfrei, F.; Turner, J. J.; Wolf, M.; Wurth, W.; Nilsson, A. *Science.* **2013**, *339*, 1302.

(23) Ferrer, A.; Johnson, J. A.; Huber, T.; Mariager, S. O.; Trant, M.; Grubel, S.; Zhu, D.; Chollet, M.; Robinson, J.; Lemke, H. T.; Ingold, G.; Milne, C.; Staub, U.; Beaud, P.; Johnson, S. L. *Appl. Phys. Lett.* **2015**, *106*.

(24) Kern, J.; Tran, R.; Alonso-Mori, R.; Koroidov, S.; Echols, N.; Hattne, J.; Ibrahim, M.; Gul, S.; Laksmono, H.; Sierra, R. G.; Gildea, R. J.; Han, G.; Hellmich, J.; Lassalle-Kaiser, B.; Chatterjee, R.; Brewster, A. S.; Stan, C. A.; Glockner, C.; Lampe, A.; DiFiore, D.; Milathianaki, D.; Fry, A. R.; Seibert, M. M.; Koglin, J. E.; Gallo, E.; Uhlig, J.; Sokaras, D.; Weng, T. C.; Zwart, P. H.; Skinner, D. E.; Bogan, M. J.; Messerschmidt, M.; Glatzel, P.; Williams, G. J.; Boutet, S.; Adams, P. D.; Zouni, A.; Messinger, J.; Sauter, N. K.; Bergmann, U.; Yano, J.; Yachandra, V. K. *Nat. Commun.* **2014**, *5*.

(25) Kim, K. H.; Kim, J. G.; Nozawa, S.; Sato, T.; Oang, K. Y.; Kim, T.; Ki, H.; Jo, J.; Park, S.; Song, C.; Sato, T.; Ogawa, K.; Togashi, T.; Tono, K.; Yabashi, M.; Ishikawa, T.; Kim, J.; Ryoo, R.; Kim, J.; Ihee, H.; Adachi, S. *Nature.* **2015**, *518*.

(26) Lemke, H. T.; Bressler, C.; Chen, L. X.; Fritz, D. M.; Gaffney, K. J.; Galler, A.; Gawelda, W.; Haldrup, K.; Hartsock, R. W.; Ihee, H.; Kim, J.; Kim, K. H.; Lee, J. H.; Nielsen, M. M.; Stickrath, A. B.; Zhang, W. K.; Zhu, D. L.; Cammarata, M. *J. Phys. Chem. A.* **2013**, *117*, 735.

(27) Mitzner, R.; Rehanek, J.; Kern, J.; Gul, S.; Hattne, J.; Taguchi, T.; Alonso-Mori, R.; Tran, R.; Weniger, C.; Schroder, H.; Quevedo, W.; Laksmono, H.; Sierra, R. G.; Han, G. Y.; Lassalle-Kaiser, B.; Koroidov, S.; Kubicek, K.; Schreck, S.; Kunnus, K.; Brzhezinskaya, M.; Firsov, A.; Minitti, M. P.; Turner, J. J.; Moeller, S.; Sauter, N. K.; Bogan, M. J.; Nordlund, D.; Schlotter, W. F.; Messinger, J.; Borovik, A.; Techert, S.; de Groot, F. M. F.; Fohlisch, A.; Erko, A.; Bergmann, U.; Yachandra, V. K.; Wernet, P.; Yano, J. *J. Phys. Chem. Lett.* **2013**, *4*, 3641.

(28) Zhang, W. K.; Alonso-Mori, R.; Bergmann, U.; Bressler, C.; Chollet, M.; Galler, A.; Gawelda, W.; Hadt, R. G.; Hartsock, R. W.; Kroll, T.; Kjaer, K. S.; Kubicek, K.; Lemke, H. T.; Liang, H. Y. W.; Meyer, D. A.; Nielsen, M. M.; Purser, C.; Robinson, J. S.; Solomon, E. I.; Sun, Z.; Sokaras, D.; van Driel, T. B.; Vanko, G.; Weng, T. C.; Zhu, D. L.; Gaffney, K. J. *Nature.* **2014**, *509*, 345.

(29) Berrah, N.; Bozek, J.; Costello, J. T.; Duesterer, S.; Fang, L.; Feldhaus, J.; Fukuzawa, H.; Hoener, M.; Jiang, Y. H.; Johnsson, P.; Kennedy, E. T.; Meyer, M.; Moshammer, R.; Radcliffe, P.; Richter, M.; Rouzee, A.; Rudenko, A.; Sorokin, A. A.; Tiedtke, K.; Ueda, K.; Ullrich, J.; Vrakking, M. J. J. *J. Mod. Opt.* **2010**, *57*, 1015.

(30) Emma, P.; Akre, R.; Arthur, J.; Bionta, R.; Bostedt, C.; Bozek, J.; Brachmann, A.; Bucksbaum, P.; Coffee, R.; Decker, F. J.; Ding, Y.; Dowell, D.; Edstrom, S.; Fisher, A.; Frisch, J.; Gilevich, S.; Hastings, J.; Hays, G.; Hering, P.; Huang, Z.; Iverson, R.; Loos, H.; Messerschmidt, M.; Miahnahri, A.; Moeller, S.; Nuhn, H. D.; Pile, G.; Ratner, D.; Rzepiela, J.; Schultz, D.; Smith, T.; Stefan, P.; Tompkins, H.; Turner, J.; Welch, J.; White, W.; Wu, J.; Yocky, G.; Galayda, J. *Nat. Photon.* **2010**, *4*, 641.

(31) Patterson, B. D.; Abela, R. *Phys. Chem. Chem. Phys.* **2010**, *12*, 5647.

(32) Zhang, X. Y.; Wasinger, E. C.; Muresan, A. Z.; Attenkofer, K.; Jennings, G.; Lindsey, J. S.; Chen, L. X. *J. Phys. Chem. A.* **2007**, *111*, 11736.

(33) Zamyatin, A. V.; Gusev, A. V.; Rodgers, M. A. J. *J. Am. Chem. Soc.* **2004**, *126*, 15934.

(34) Kim, D.; Kirmaier, C.; Holten, D. *Chem. Phys.* **1983**, *75*, 305.

(35) Retsek, J. L.; Drain, C. M.; Kirmaier, C.; Nurco, D. J.; Medforth, C. J.; Smith, K. M.; Sazanovich, I. V.; Chirvony, V. S.; Fajer, J.; Holten, D. *J. Am. Chem. Soc.* **2003**, *125*, 9787.

(36) Gentemann, S.; Nelson, N. Y.; Jaquinod, L.; Nurco, D. J.; Leung, S. H.; Medforth, C. J.; Smith, K. M.; Fajer, J.; Holten, D. *J. Phys. Chem. B.* **1997**, *101*, 1247.

(37) Jia, S.-L.; Jentzen, W.; Shang, M.; Song, X.-Z.; Ma, J.-G.; Scheidt, W. R.; Shelnutt, J. A. *Inorg. Chem.* **1998**, *37*, 4402.

(38) Song, Y.; Haddad, R. E.; Jia, S.-L.; Hok, S.; Olmstead, M. M.; Nurco, D. J.; Schore, N. E.; Zhang, J.; Ma, J. G.; Smith, K. M.; Gazeau, S.; Pe´ caut, J.; Marchon, J.-C.; Medforth, C. J.; Shelnutt, J. A. *J. Am. Chem. Soc.* **2005**, *127*, 1179.

(39) Shelnutt, J. A.; Majumder, S. A.; Sparks, L. D.; Hobbs, J. D.; Medforth, C. J.; Senge, M. O.; Smith, K. M.; Miura, M.; Luo, L.; Quirke, J. M. E. *J. Raman Spectrosc.* **1992**, *23*, 523.

(40) Jeong, D. H.; Kim, D.; Cho, D. W.; Jeoung, S. C. *J. Raman Spectrosc.* **2001**, *32*, 487.

(41) Chen, L. X.; Zhang, X.; Wasinger, E. C.; Lockard, J. V.; Stickrath, A. B.; Mara, M. W.; Attenkofer, K.; Jennings, G.; Smolentsev, G.; Soldatov, A. *Chem. Sci.* **2010**, *1*.

(42) *X-ray Absorption and X-ray Emission Spectroscopy: Theory and Applications*; van Bokhoven, J.; Lamberti, C., Eds.; Wiley & Sons: New York, 2015.

(43) Chen, L. X. *J. Electron Spectrosc. Relat. Phenom.* **2001**, *119*, 161.

(44) Katayama, T.; Inubushi, Y.; Obara, Y.; Sato, T.; Togashi, T.; Tono, K.; Hatsui, T.; Kameshima, T.; Bhattacharya, A.; Ogi, Y.; Kurahashi, N.; Misawa, K.; Suzuki, T.; Yabashi, M. *Appl. Phys. Lett.* **2013**, *103*.

(45) T' and T(d,d) are so named for historical reasons and for consistency with previous studies by both our group and others. Becuase T(d,d) is the lowest energy triplet state, it is assumed that this relatively long lived state is a triplet. T' is assigned by some studies to a hot triplet (d,d) state generated by energy transfer and intersystem crossing within instrument response. However, due to the inability of XANES to distinguish between spin states in this case, this study can not definitively assign T' or T(d,d) to a triplet state nor does it provide direct evidence of intersystem crossing.

(46) Chollet, M.; Alonso-Mori, R.; Cammarata, M.; Damiani, D.; Defever, J.; Delor, J. T.; Feng, Y.; Glownia, J. M.; Langton, J. B.; Nelson, S.; Ramsey, K.; Robert, A.; Sikorski, M.; Song, S.; Stefanescu, D.; Srinivasan, V.; Zhu, D.; Lemke, H. T.; Fritz, D. M. *J. Synch. Rad.* **2015**, *22*, 503.

(47) Glownia, J. M.; Cryan, J.; Andreasson, J.; Belkacem, A.; Berrah, N.; Blaga, C. I.; Bostedt, C.; Bozek, J.; DiMauro, L. F.; Fang, L.; Frisch, J.; Gessner, O.; Gühr, M.; Hajdu, J.; Hertlein, M. P.; Hoener, M.; Huang, G.; Kornilov, O.; Marangos, J. P.; March, A. M.; McFarland, B. K.; Merdji, H.; Petrovic, V. S.; Raman, C.; Ray, D.; Reis, D. A.; Trigo, M.; White, J. L.; White, W.; Wilcox, R.; Young, L.; Coffee, R. N.; Bucksbaum, P. H. *Optics Express.* **2010**, *18*, 17620.

(48) Chen, L. X.; Zhang, X.; Wasinger, E. C.; Attenkofer, K.; Jennings, G.; Muresan, A. Z.; Lindsey, J. S. *J. Am. Chem. Soc.* **2007**, *129*, 9616.

(49) Fonseca Guerra, C.; Snijders, J. G.; te Velde, G.; Baerends, E. J. *Theor. Chem. Acc.* **1998**, *99*, 391.

(50) te Velde, G.; Bickelhaupt, F. M.; Baerends, E. J.; Fonseca Guerra, C.; van Gisbergen, S. J. A.; Snijders, J. G.; Ziegler, T. *J. Comput. Chem.* **2001**, *22*, 931.

(51) Patchkovskii, S.; Kozlowski, P. M.; Zgierski, M. Z. *J. Chem. Phys.* **2004**, *121*, 1317.

(52) Becke, A. D. *J. Chem. Phys.* **1986**, *84*, 4524.

(53) Perdew, J. *Phys. Rev. B.* **1986**, *33*, 8822.

(54) Frisch, M. J.; Trucks, G. W.; Schlegel, H. B.; Scuseria, G. E.; Robb, M. A.; Cheeseman, J. R.; Scalmani, G.; Barone, V.; Mennucci, B.; Petersson, G. A.; Nakatsuji, H.; Caricato, M.; Li, X.; Hratchian, H. P.; Izmaylov, A. F.; Bloino, J.; Zheng, G.; Sonnenberg, J. L.; Hada, M.; Ehara, M.; Toyota, K.; Fukuda, R.; Hasegawa, J.; Ishida, M.; T. Nakajima; Honda, Y.; Kitao, O.; Nakai, H.; Vreven, T.; Jr., J. A. M.; Peralta, J. E.; Ogliaro, F.; Bearpark, M.; Heyd, J. J.; Brothers, E.; Kudin, K. N.; Staroverov, V. N.; Keith, T.; Kobayashi, R.; Normand, J.; Raghavachari, K.; Rendell, A.; Burant, J. C.; Iyengar, S. S.; Tomasi, J.; Cossi, M.; Rega, N.; Millam, J. M.; Klene, M.; Knox, J. E.; Cross, J. B.; Bakken, V.; Adamo, C.; Jaramillo, J.;

Gomperts, R.; Stratmann, R. E.; Yazyev, O.; Austin, A. J.; Cammi, R.; Pomelli, C.; Ochterski, J. W.; Martin, R. L.; Morokuma, K.; Zakrzewski, V. G.; Voth, G. A.; Salvador, P.; Dannenberg, J. J.; Dapprich, S.; Daniels, A. D.; Farkas, O.; Foresman, J. B.; Ortiz, J. V.; Cioslowski, J.; Fox, D. J.; Gaussian Development Version, Revision H.12+ ed.; Gaussian Inc.: Wallingford, CT, 2010.

(55) Rassolov, V. A.; Pople, J. A.; Ratner, M. A.; Windus, T. L. *J. Chem. Phys.* **1998**, *109*, 1223.

(56) Hariharan, P. C.; Pople, J. A. *Theor. Chem. Acc.* **1973**, *28*, 213.

(57) Liang, W.; Fischer, S. A.; Frisch, M. J.; Li, X. *J. Chem. Theor. Comput.* **2011**, *7*, 3540.

(58) Lestrange, P. J.; Nguyen, P. D.; Li, X. *J. Chem. Theor. Comput.* **2015**, Submitted.

(59) Weigend, F.; Ahlrichs, R. *Phys. Chem. Chem. Phys.* **2005**, *7*, 3297.

(60) Rappoport, D.; Furche, F. *J. Chem. Phys.* **2010**, *133*, 134105.

(61) Schuchardt, K. L.; Didier, B. T.; Elsethagen, T.; Sun, L.; Gurumoorthi, V.; Chase, J.; Li, J.; Windus, T. L. *J. Chem. Inf. Model.* **2007**, *47*, 1045.

(62) Feller, D. *J. Comp. Chem.* **1996**, *17*, 1571.

(63) Chen, L. X.; Jäger, W. J. H.; Jennings, G.; Gosztola, D. J.; Munkholm, A.; Hessler, J. P. *Science.* **2001**, *292*, 262.

(64) Kau, L.-S.; Spira-Solomon, D. J.; Penner-Hahn, J. E.; Hodgson, K. O.; Solomon, E. I. *J. Am. Chem. Soc.* **1987**, *109*, 6433.

(65) Westre, T. E.; Kennepohl, P.; DeWitt, J. G.; Hedman, B.; Hodgson, K. O.; Solomon, E. I. *J. Am. Chem. Soc.* **1997**, *119*, 6297.

(66) Campbell, L.; Tanaka, S.; Mukamel, S. *Chem. Phys.* **2004**, *299*, 225.

(67) Rodriguez, J.; Holten, D. *J. Chem. Phys.* **1989**, *91*, 3525.

(68) Gilbert, A. T. B.; Besley, N. A.; Gill, P. M. W. *J. Phys. Chem. A.* **2008**, *112*, 13164.

(69) Davidson, E. R. *J. Chem. Phys.* **1964**, *41*, 656.

(70) Peng, B.; Van Kuiken, B. E.; Ding, F.; Li, X. *J. Chem. Theor. Comput.* **2013**, *9*, 3933.

(71) Martin, R. L. *J. Chem. Phys.* **2003**, *118*, 4775.

(72) Bacskay, G. B. *Chem. Phys.* **1981**, *61*, 385.

(73) DeBeer George, S.; Petrenko, T.; Neese, F. *Inorg. Chem. Acta.* **2008**, *361*, 965.

(74) Besley, N. A.; Asmuruf, F. A. *Phys. Chem. Chem. Phys.* **2010**, *12*, 12024.

(75) Fronzoni, G.; De Francesco, R.; Stener, M. *J. Phys. Chem. B.* **2005**, *109*, 10332.

(76) Ha-Thi, M.-H.; Shafizadeh, N.; Poisson, L.; Soep, B. *Phys. Chem. Chem. Phys.* **2010**, *12*, 14985.

(77) Sorgues, S.; Poisson, L.; Raffael, K.; Krim, L.; Soep, B.; Shafizadeh, N. *J. Chem. Phys.* **2006**, *124*, 114302.

(78) Mizutani, Y.; Uesugi, Y.; Kitagawa, T. *J. Chem. Phys.* **1999**, *111*, 8950.

(79) Fadley, C. S.; Hagstrom, S. B. M.; Klein, M. P.; Shirley, D. A. *J. Chem. Phys.* **1968**, *48*, 3779.

(80) Sarangi, R.; DeBeer George, S.; Rudd, D. J.; Szilagyi, R. K.; Ribas, X.; Rovira, C.; Almeida, M.; Hodgson, K. O.; Hedman, B.; Solomon, E. I. *J. Am. Chem. Soc.* **2007**, *129*, 2316.

(81) Gu, W.; Wang, H.; Wang, K. *Dalton Trans.* **2014**, *43*, 6406.

(82) Drain, C. M.; Gentemann, S.; Roberts, J. A.; Nelson, N. Y.; Medforth, C. J.; Jia, S.; Simpson, M. C.; Smith, K. M.; Fajer, J.; Shelnutt, J. A.; Holten, D. *J. Am. Chem. Soc.* **1998**, *120*, 3781.

(83) Alden, R. G.; Crawford, B. A.; Doolen, R.; Ondrias, M. R.; Shelnutt, J. A. *J. Am. Chem. Soc.* **1989**, *111*, 2070.

(84) Alden, R. G.; Ondrias, M. R.; Shelnutt, J. A. *J. Am. Chem. Soc.* **1990**, *112*, 691.

(85) Balakrishnan, G.; Soldatova, A. V.; Reid, P. J.; Spiro, T. G. *J. Am. Chem. Soc.* **2014**, *136*, 8746.

(86) Wittenberg, B. A.; Wittenberg, J. B. *Annu. Rev. Physiol.* **1989**, *51*, 857.

(87) Parkhurst, L. J. *Annu. Rev. Phys. Chem.* **1979**, *30*, 503.

(88) Olson, J. S.; Soman, J.; Phillips, G. N., Jr. *IUBMB life.* **2007**, *59*, 552.

(89) Teeter, M. M. *Prot. Sci.* **2004**, *13*, 313.

(90) Antonyuk, S. V.; Rustage, N.; Petersen, C. A.; Arnst, J. L.; Heyes, D. J.; Sharma, R.; Berry, N. G.; Scrutton, N. S.; Eady, R. R.; Andrew, C. R.; Hasnain, S. S. *Proc. Nat. Acad. Sci.* **2011**, *108*, 15780.

(91) Kruglik, S. G.; Yoo, B.-K.; Franzen, S.; Vos, M. H.; Martin, J.-L.; Negrerie, M. *Proc. Nat. Acad. Sci.* **2010**, *107*, 13678.

(92) In *The Smallest Biomolecules: Diatomics and their Interactions with Heme Proteins*; Ghosh, A., Ed.; Elsevier: Amsterdam, 2008.

(93) Perutz, M. F. *Nature.* **1970**, *228*, 726.

(94) Kitagawa, T.; Mizutani, Y. *Coord. Chem. Rev.* **1994**, *135–136*, 685.

(95) Kitagawa, T.; Haruta, N.; Mizutani, Y. *Biopolymers.* **2002**, *67*, 207.

(96) Rovira, C.; Parrinello, M. *Int. J. Quant. Chem.* **2000**, *80*, 1172.

(97) Arcovito, A.; Lamb, D. C.; Nienhaus, G. U.; Hazemann, J. L.; Benfatto, M.; Della Longa, S. *Biophys J.* **2005**, *88*, 2954.

(98) Schmidt, M.; Nienhaus, K.; Pahl, R.; Krasselt, A.; Anderson, S.; Parak, F.; Nienhaus, G. U.; Šrajer, V. *Proc. Nat. Acad. Sci.* **2005**, *102*, 11704.

(99) Esquerra, R. M.; Goldbeck, R. A.; Kim-Shapiro, D. B.; Kliger, D. S. *Biochemistry.* **1998**, *37*, 17527.

(100) Plunkett, S. E. C., James L.; Tague, Thomas J.; Palmer, Richard A. *Appl. Spectrosc.* **1995**, *49*, 702.

(101) Franzen, S.; Kiger, L.; Poyart, C.; Martin, J.-L. *Biophys. J.* **2001**, *80*, 2372.

(102) Huang, J.; Buyukcakir, O.; Mara, M. W.; Coskun, A.; Dimitrijevic, N. M.; Barin, G.; Kokhan, O.; Stickrath, A. B.; Ruppert, R.; Tiede, D. M.; Stoddart, J. F.; Sauvage, J.-P.; Chen, L. X. *Ange. Chem.* **2012**, *124*, 12883.

(103) Rosca, F.; Kumar, A. T. N.; Ionascu, D.; Ye, X.; Demidov, A. A.; Sjodin, T.; Wharton, D.; Barrick, D.; Sligar, S. G.; Yonetani, T.; Champion, P. M. *J. Phys. Chem. A.* **2001**, *106*, 3540.

(104) Dao, L. V.; Lowe, R. M.; Rowlands, W. J.; Lincoln, C. N.; Hannaford, P. In *Femtochemistry And Femtobiology*; Douhal, A. a. S., Jesus, Ed.; World Scientific Publishing Co., Pte. Ltd.: River Edge, NJ: 2002, p 815.

(105) Cho, H. S.; Dashdorj, N.; Schotte, F.; Graber, T.; Henning, R.; Anfinrud, P. *Proc. Nat. Acad. Sci.* **2010**, *107*, 7281.

(106) Mills, D. M.; Lewis, A.; Harootunian, A.; Huang, J.; Smith, B. *Science.* **1984**, *223*, 811.

(107) Wang, H.; Peng, G.; Cramer, S. P. *J. of Electron Spectrosc. Rel. Phen.* **2005**, *143*, 1.

(108) Mizutani, Y.; Kitagawa, T. *Science.* **1997**, *278*, 443.

(109) Ye, X.; Demidov, A.; Rosca, F.; Wang, W.; Kumar, A.; Ionascu, D.; Zhu, L.; Barrick, D.; Wharton, D.; Champion, P. M. *J. Phys. Chem. A.* **2003**, *107*, 8156.

(110) Kruglik, S. G.; Lambry, J.-C.; Martin, J.-L.; Vos, M. H.; Negrerie, M. *J. Raman Spectrosc.* **2011**, *42*, 265.

(111) Lim, M.; Jackson, T. A.; Anfinrud, P. A. *J. Phys. Chem.* **1996**, *100*, 12043.

(112) Petrich, J. W.; Martin, J. L.; Houde, D.; Poyart, C.; Orszag, A. *Biochemistry.* **1987**, *26*, 7914.

(113) Petrich, J. W.; Poyart, C.; Martin, J. L. *Biochemistry.* **1988**, *27*, 4049.

(114) Kholodenko, Y.; Volk, M.; Gooding, E.; Hochstrasser, R. M. *Chem. Phys.* **2000**, *259*, 71.

(115) Lemke, H. T.; Weaver, M.; Chollet, M.; Robinson, J.; Glownia, J. M.; Zhu, D.; Bionta, M. R.; Cammarata, M.; Harmand, M.; Coffee, R. N.; Fritz, D. M. 2013; Vol. 8778, p 87780S.

(116) Stickrath, A. B.; Mara, M. W.; Lockard, J. V.; Harpham, M. R.; Huang, J.; Zhang, X.; Attenkofer, K.; Chen, L. X. *J. Phys. Chem. B.* **2012**.

(117) Lima, F. A.; Penfold, T. J.; van der Veen, R. M.; Reinhard, M.; Abela, R.; Tavernelli, I.; Rothlisberger, U.; Benfatto, M.; Milne, C. J.; Chergui, M. *Phys. Chem. Chem. Phys.* **2014**, *16*, 1617.

(118) Della Longa, S.; Arcovito, A.; Vallone, B.; Congiu Castellano, A.; Kahn, R.; Vicat, J.; Soldo, Y.; Hazemann, J. L. *J. Synch. Rad.* **1999**, *6*, 1138.

(119) Cabaret, D.; Bordage, A.; Juhin, A.; Arfaoui, M.; Gaudry, E. *Phys. Chem. Chem. Phys.* **2010**, *12*, 5619.

(120) Arcovito, A.; Lamb, D. C.; Nienhaus, G. U.; Hazemann, J. L.; Benfatto, M.; Longa, S. D. *Biophys. J.* **2005**, *88*, 2954.

(121) Wilson, S. A.; Green, E.; Mathews, I. I.; Benfatto, M.; Hodgson, K. O.; Hedman, B.; Sarangi, R. *Proc. Nat. Acad. Sci.* **2013**, *110*, 16333.

(122) Silatani, M.; Lima, F. A.; Penfold, T. J.; Rittmann, J.; Reinhard, M. E.; Rittmann-Frank, H. M.; Borca, C.; Grolimund, D.; Milne, C. J.; Chergui, M. *Proc. Natl. Acad. Sci.* **2015**, *112*, 12922.

(123) Liebisch, P.; Dau, H. *ChemPhysChem.* **2010**, *11*, 1236.

(124) Levantino, M.; Schirò, G.; Lemke, H. T.; Cottone, G.; Glownia, J. M.; Zhu, D.; Chollet, M.; Ihee, H.; Cupane, A.; Cammarata, M. *Nat. Comm.* **2015**, *6*.

(125) Can, M.; Zoppellaro, G.; Andersson, K. K.; Bren, K. L. *Inorg. Chem.* **2011**, *50*, 12018.

(126) Zoppellaro, G.; Harbitz, E.; Kaur, R.; Ensign, A. A.; Bren, K. L.; Andersson, K. K. *J. Am. Chem. Soc.* **2008**, *130*, 15348.

(127) Barkigia, K. M.; Chantranupong, L.; Smith, K. M.; Fajer, J. *J. Am. Chem. Soc.* **1988**, *110*, 7566.

(128) Olea, C.; Kuriyan, J.; Marletta, M. A. *J. Am. Chem. Soc.* **2010**, *132*, 12794.

(129) Geissinger, P.; Kohler, B. E.; Woehl, J. C. *J. Phys. Chem.* **1995**, *99*, 16527.

(130) Hobbs, J. D.; Shelnutt, J. A. *J. Protein Chem.* **1995**, *14*, 19.

(131) Ma, J. G.; Laberge, M.; Song, X. Z.; Jentzen, W.; Jia, S. L.; Zhang, J.; Vanderkooi, J. M.; Shelnutt, J. A. *Biochemistry.* **1998**, *37*, 5118.

(132) Hagihara, B.; OSHINO, R.; IIZUKA, T. *J. Biochem. (Tokyo, Jpn.).* **1974**, *75*, 45.

(133) Wagner, G. C.; Kassner, R. J. *Biochem. Biophys. Res. Commun.* **1975**, *63*, 385.

(134) Champion, P.; Collins, D.; Fitchen, D. *J. Am. Chem. Soc.* **1976**, *98*, 7114.

(135) Friedman, J. M.; Rousseau, D. L.; Adar, F. *Proc. Natl. Acad. Sci.* **1977**, *74*, 2607.

(136) Cowan, J. A.; Gray, H. B. *Inorg. Chem.* **1989**, *28*, 2074.

(137) Shelnutt, J. A.; Cheung, L. D.; Chang, R. C. C.; Yu, N. T.; Felton, R. H. *J. Chem. Phys.* **1977**, *66*, 3387.

(138) Canters, G. W. *J. Chem. Phys.* **1981**, *74*, 157.

(139) Canters, G. W.; Jansen, G.; Noort, M.; Van der Waals, J. H. *J. Phys. Chem.* **1976**, *80*, 2253.

(140) Van der Waals, J. H.; Van Dorp, W. G.; Schaafsma, T. J. *Electron spin resonance of porphyrin excited states*; Academic Press: New York, 1979; Vol. 4.

(141) Hoffman, B. M.; Ratner, M. A. *Mol. Phys.* **1978**, *35*, 901.

(142) Hougen, J. T. *J. Mol. Spectrosc.* **1964**, *13*, 149.

(143) Hoffman, B. M. *J. Am. Chem. Soc.* **1975**, *97*, 1688.

(144) Angiolillo, P. J.; Vanderkooi, J. M. *Biophys. J.* **1995**, *68*, 2505.

(145) Angiolillo, P. J.; Vanderkooi, J. M. *Biophys. J.* **1998**, *75*, 1491.

(146) Nagatani, H.; Tanida, H.; Ozeki, T.; Watanabe, I. *Langmuir.* **2006**, *22*, 209.

(147) Tanida, H.; Nagatani, H.; Watanabe, I. *J. Chem. Phys.* **2003**, *118*, 10369.

(148) Pekkarinen, L.; Linschitz, H. *J. Am. Chem. Soc.* **1960**, *82*, 2407.

(149) Feitelson, J.; Barboy, N. *J. Phys. Chem.* **1986**, *90*, 271.

(150) Nguyen, K. A.; Day, P. N.; Pachter, R. *J. Phys. Chem. A.* **1999**, *103*, 9378.

(151) Nguyen, K. A.; Pachter, R. *J. Chem. Phys.* **2003**, *118*, 5802.

(152) Vanderkooi, J. M.; Adar, F.; Erecińska, M. *Eur. J. Biochem.* **1976**, *64*, 381.

(153) Anni, H.; Vanderkooi, J. M.; Mayne, L. *Biochemistry.* **1995**, *34*, 5744.

(154) Koshiyama, T.; Shirai, M.; Hikage, T.; Tabe, H.; Tanaka, K.; Kitagawa, S.; Ueno, T. *Ange. Chem.* **2011**, *50*, 4849.

(155) Prendergast, K.; Spiro, T. G. *J. Phys. Chem.* **1991**, *95*, 9728.

(156) Tokita, Y.; Shimura, J.; Nakajima, H.; Goto, Y.; Watanabe, Y. *J. Am. Chem. Soc.* **2008**, *130*, 5302.

(157) A. Shelnutt, J.; Song, X.-Z.; Ma, J.-G.; Jia, S.-L.; Jentzen, W.; J. Medforth, C.; J. Medforth, C. *Chem. Soc. Rev.* **1998**, *27*, 31.

(158) Jentzen, W.; Song, X.-Z.; Shelnutt, J. A. *J. Phys. Chem. B.* **1997**, *101*, 1684.

(159) Mosquera, M. A.; Chen, L. X.; Ratner, M. A.; Schatz, G. C. *J. Chem. Phys.* **2016**, *144*, 204105.

Vita

Megan Lynn Shelby

Born 7/16/1986 in San Jose, CA

Education:

Northwestern University, Department of Chemistry, Evanston, IL & Argonne National Lab, Chemical Sciences and Engineering Division, Lemont, IL (Sept. 2010 – Dec. 2016)

PhD, Physical Chemistry, coursework in Physical Chemistry and Biophysics

Advisors: Lin X. Chen (ANL CSE and NU Chemistry) and Brian M. Hoffman (NU Chemistry)

Thesis: "Probing Excited State Dynamics in Metalloporphyrins and Hemoproteins with X-Ray Transient Absorption Spectroscopy"

University of California at Berkeley, College of Chemistry, Berkeley, CA (Aug. 2004 – May 2008)

Bachelor of Science, Chemical Biology, advanced coursework in Physical Chemistry, Biological Chemistry, and Molecular Biology

Research Experience:

Graduate Researcher, Chemistry Dept., Northwestern University & Chemical Sciences and Engineering Division, Argonne National Lab (Dec. 2010 - Dec. 2016)

Advisors: Lin X. Chen (ANL CSE and NU Chemistry) and Brian M. Hoffman (NU Chemistry)

Dynamics of electronic structure and nuclear geometry in excited metalloporphyrins and hemoproteins investigated by time-resolved X-ray absorption spectroscopy (XAS)

- Implementing a new technique – XAS on the femtosecond timescale at the Linear Coherent Light Source (LCLS), SLAC National Accelerator Laboratory – to study ultrafast structural and electronic relaxation in a Nickel porphyrin following optical excitation.
- Using femtosecond LCLS pulses to track how photo-initiated ligand dissociation and active site heme distortion in myoglobin is translated through global protein conformational change in collaboration with Cammarata Group.
- Conducting picosecond-resolved structural analysis of the electron transfer active excited states of Zn porphyrins and heme proteins using transient XAS at the Advanced Photon Source (APS).
- Development of time-resolved XAS instrumentation at Sector 11, APS (Basic Energy Sciences Structural Research Center) to accommodate metalloprotein samples.
- Bacterial expression, chemical modification and cofactor exchange, and solid phase purification of hemoprotein samples for XAS analysis.

- Participate in many collaborative X-ray spectroscopy experiments, involving for example in-situ electrochemistry, functionalized nanoparticles, various small molecule photo-catalysts, and solid-state photo-catalysts on films.

Research Assistant, Physical Biosciences Division, Lawrence Berkeley National Lab (Sept. 2008 - Aug. 2010)

Advisors**:** Vittal K. Yachandra and Junko Yano

Physical studies of Photosystem II (PSII) structure and catalytic cycle by X-ray absorption spectroscopy and X-ray emission spectroscopy (XES)

- XES capabilities at beamline 6-2, Stanford Synchrotoron Radiation Lab (SSRL) used to investigate oxidation state and oxygen ligation changes in the PSII catalytic site, which are implicated in mechanistically important H_2O binding, oxygen radical formation, or O-O bond formation.
- Depleted PSII protein samples of active site calcium and analyzed different steps in the catalytic cycle with XAS at beamline 7-3, SSRL to assess structural and electronic role of Ca ion.

Student Research Assistant, Earth Sciences Division, Lawrence Berkeley National Lab (July 2007 - Aug. 2008)

Advisor: Dr. Terry C. Hazen

Growth and characterization of wild type and mutant strains of the extremophile Sulfolobus sulfotaricus as a candidate for biofuel production

- Bacterial cultures grown under various conditions to assess feedstock metabolism.
- Cultures characterized using ion chromatography, protein quantification, and RNA extraction.

Student Research Assistant, College of Chemistry, University of California at Berkeley (Sept. 2006 - May 2007)

Advisor: Professor Matt Francis

Preparation of functionalized fluorescent EOSIN dyes for targeted labeling

Fellowships, Awards, and Grants:

Co-authored funded National Institutes of Health, National Institute of General Medical Sciences R01 grant: GM115761-01 (PI: Lin X. Chen), "Capturing transient protein structures on multiple spatial and temporal scales". (2015)

Robert L. Burwell Scholar, departmental award for excellence in Physical Chemistry (2014)

Phi Lambda Upsilon Chemistry Honors Society inductee, Northwestern chapter (2012)

Molecular Biophysics Training Program Appointee (Sept. 2011 – Sept. 2013)

Northwestern University Molecular Biophysics Training Program with full stipend funding by the National Institute of General Medical Sciences (NIGMS) of the National Institutes of Health

- Co-chair of the organizing committee for the 3rd annual Northwestern Biophysics Symposium, a day-long event with several off-campus invited speakers.
- Fulfilled additional curricular requirements in Biophysics in addition to Chemistry Dept. requirements.
- Presented research to fellow training program appointees and to Biophysics faculty.
- Participation in other Biophysics events such as seminars, symposia and journal clubs.

Publications and Presentations:

Publications:

Shelby ML, Lestrange PJ, Jackson NE, Haldrup K, Mara MW, Stickrath AB, Zhu D, Lemke HT, Chollet M, Hoffman BM, Li X, Chen LX. Ultrafast Excited State Relaxation of a Metalloporphyrin Revealed by Femtosecond X-ray Absorption Spectroscopy. *Journal of the American Chemical Society* 2016, **138**(28)**:** 8752-8764.

Shelby ML, Balducci L, Van Driel T, Hayes D, Fransted K, Kjaer KS, Chollet M, Lemke HT, Hoffman BM, Cammarata M, Chen LX. Local and Global Dynamics of CO Photolysis from the Myoglobin Active Site on the Femtosecond Timescale. In preparation

Lohmiller T, **Shelby ML**, Long X, Yachandra VK, Yano J. Removal of Ca2+ from the Oxygen-Evolving Complex in Photosystem II Has Minimal Effect on the Mn4O5 Core Structure: A Polarized Mn X-ray Absorption Spectroscopy Study. *The Journal of Physical Chemistry B* 2015, **119**(43)**:** 13742-13754.

Shelby ML, Mara MW, Chen LX. New insight into metalloporphyrin excited state structures and axial ligand binding from X-ray transient absorption spectroscopic studies. *Coordination Chemistry Reviews* 2014, **277–278:** 291-299.

Lin Z, **Shelby ML**, Hayes D, Fransted KA, Chen LX, Allen MJ. Water-exchange rates of lanthanide ions in an ionic liquid. *Dalton Transactions* 2014, **43**(43)**:** 16156-16159.

Mara MW, **Shelby ML**, Stickrath A, Harpham M, Huang J, Zhang X, Hoffman BM, Chen LX. Electronic and Nuclear Structural Snapshots in Ligand Dissociation and Recombination Processes of Iron Porphyrin in Solution: A Combined Optical/X-ray Approach. *The Journal of Physical Chemistry B* 2013, **117**(45)**:** 14089-14098.

Chen LX, **Shelby ML**, Lestrange PJ, Jackson NE, Haldrup K, Mara MW, Stickrath AB, Zhu D, Lemke H, Chollet M. Imaging ultrafast excited state pathways in transition metal complexes by X-ray transient absorption and scattering using X-ray free electron laser source. *Faraday Discussions* 2016.

Haldrup K, Dohn AO, **Shelby ML**, Mara MW, Stickrath AB, Harpham MR, Huang J, Zhang

X, Møller KB, Chakraborty A. Butterfly Deformation Modes in a Photoexcited Pyrazolate-Bridged Pt Complex Measured by Time-Resolved X-Ray Scattering in Solution. *The Journal of Physical Chemistry A* 2016, **120**(38)**:** 7475-7483.

Chen LX, Zhang X, **Shelby ML**. Recent advances on ultrafast X-ray spectroscopy in the chemical sciences. *Chem. Sci.* 2014, **5**(11)**:** 4136-4152.

Kohler L, Hayes D, Hong J, Carter TJ, **Shelby ML**, Fransted KA, Chen LX, Mulfort KL. Synthesis, structure, ultrafast kinetics, and light-induced dynamics of CuHETPHEN chromophores. *Dalton Transactions* 2016.

Kern J, Schroeder H, **Shelby ML**, Pushkar Y, Lasalle B, Glatzel P, Yachandra VK, Bergmann U, Yano J. Direct Detection of Oxygen Ligands to the Mn4Ca Complex in Photosystem II by X-ray Emission Spectroscopy. *Photosynthesis Research for Food, Fuel and the Future*. Springer, 2013, pp 231-233.

Hayes D, Hadt RG, Emery JD, Cordones AA, Martinson AB, **Shelby ML**, Fransted KA, Dahlberg PD, Hong J, Zhang X. Electronic and nuclear contributions to time-resolved optical and X-ray absorption spectra of hematite and insights into photoelectrochemical performance. *Energy & Environmental Science* 2016.

Mara MW, Bowman DN, Buyukcakir O, **Shelby ML**, Haldrup K, Huang J, Harpham MR, Stickrath AB, Zhang X, Stoddart JF, Coskun A, Jakubikova E, Chen LX. Electron Injection from Copper Diimine Sensitizers into TiO2: Structural Effects and Their Implications for Solar Energy Conversion Devices. *Journal of the American Chemical Society* 2015, **137**(30)**:** 9670 9684.

Huang J, Mara MW, Stickrath AB, Kokhan O, Harpham MR, Haldrup K, **Shelby ML**, Zhang X, Ruppert R, Sauvage JP, Chen LX. A strong steric hindrance effect on ground state, excited state, and charge separated state properties of a Cu-diimine complex captured by X-ray transient absorption spectroscopy. *Dalton Trans.* 2014, **43**(47)**:** 17615-17623.

Bacchi M, Berggren G, Niklas J, Veinberg E, Mara MW, **Shelby ML**, Poluektov OG, Chen LX, Tiede DM, Cavazza C, Field MJ, Fontecave M, Artero V. Cobaloxime-Based Artificial Hydrogenases. *Inorganic Chemistry* 2014, **53**(15)**:** 8071-8082.

Fransted KA, Jackson NE, Zong R, Mara MW, Huang J, Harpham MR, **Shelby ML**, Thummel RP, Chen LX. Ultrafast Structural Dynamics of Cu(I)-Bicinchoninic Acid and Their Implications for Solar Energy Applications. *The Journal of Physical Chemistry A* 2014, **118**(45)**:** 10497-10506.

Vagnini MT, Mara MW, Harpham MR, Huang J, **Shelby ML**, Chen LX, Wasielewski MR. Interrogating the photogenerated Ir(iv) state of a water oxidation catalyst using ultrafast optical and X-ray absorption spectroscopy. *Chemical Science* 2013, **4**(10)**:** 3863.

Khnayzer RS, Mara MW, Huang J, **Shelby ML**, Chen LX, Castellano FN. Structure and Activity of Photochemically Deposited "CoPi" Oxygen Evolving Catalyst on Titania. *ACS Catalysis* 2012, **2**(10)**:** 2150-2160.

Selected Conference Presentations:

Shelby ML, Lestrage P, Jackson N, Haldrup K, Mara M, Li X, Hoffman BM, Chen LX. Ultrafast XANES characterization of relaxation dynamics in a nickel porphyrin. *Ultrafast experiments at XFEL sources, the first 5 years and beyond, Electronic Structure and Structural Dynamics Session*, Ringsted, Denmark, Aug. 27, 2014. **Invited oral presentation**.

Shelby ML, Mara MW, Hoffman BM, Chen LX. Excited-state structural dynamics of Zn-substituted hemoproteins and model compounds detected by transient and steady state XAS. *X-ray Science Gordon Research Conference,* Easton, MA, Aug. 4, 2013 – Aug. 5, 2013. **Poster presentation.**

Shelby ML, Kern J, Schroeder H, Yachandra VK, Bergmann U, Yano J. X-ray Emission Spectroscopy of the Catalytic Cycle of Water Oxidation by Photosystem II. *Western Photosynthesis Conference, Antennae and Reaction Centers session,* Pacific Grove, CA. Jan 9, 2010. S**elected for oral presentation.**

Teaching Experience:

Advanced Physical Chemistry Lab Teaching Assistant

Fred Northrup, Dir. of Undergraduate Studies, Chemistry Dept., Northwestern University *(March 2012 - June 2012)*

CASPIE Lab Teaching Assistant, Chemistry Dept., Northwestern University *(March 2011 - June 2011)*

Shelby Hatch, General Chemistry Lab director

General Chemistry Lab Teaching Assistant, Chemistry Dept., Northwestern University *(Sept. 2010 - March 2011)*

Shelby Hatch, General Chemistry Lab director,

References:

Lin Chen, Principal Investigator, Argonne National Lab and Northwestern University, Chemical Sciences and Engineering Division and Chemistry Dept. resp. lchen@anl.gov

Brian Hoffman, Principal Investigator, Northwestern University, Chemistry Dept. bmh@northwestern.edu

Kristoffer Haldrup, Senior Researcher, Technical University of Denmark, Physics Dept. hald@fysik.dtu.dk